

学位論文

Complex Langevin simulation of Bose-Einstein condensate under
extreme conditions

(極限状態に置かれたボースアインシュタイン凝縮の
複素ランジュバン法を用いた数値解析)

平成26年12月博士(理学)申請

東京大学大学院理学系研究科

物理学専攻

早田 智也

Abstract

In this thesis, we perform ab-initio lattice simulations of the nonrelativistic and relativistic Bose-Einstein condensates under strong external fields such as the electric field, the magnetic field, and the rotation. All the lattice actions discussed in this thesis are complex, so that the conventional Monte Carlo method suffers from the notorious sign problem. The path integral measure is complex due to the complex action, so that the important sampling algorithm cannot be applied. To overcome this difficulty, we adopt the complex Langevin method, which has been developed in the context of finite density quantum chromodynamics to attack the fermion sign problem.

In particular, we perform ab-initio simulation of the quantum vortex nucleation by the magnetic field or the rotation. In dilute and low temperature system, quantum and thermal fluctuations are negligible. The system can be remarkably well described by the mean field approximation. However, when quantum or thermal fluctuation becomes large, it is highly nontrivial how the quantized vortices behave. Around the critical values of temperature, chemical potential, magnetic field, or angular velocity, the fluctuation grows and the mean-field description inevitably breaks down. To understand the quantum vortex nucleation in such situations, the ab-initio simulation is necessary as discussed in this thesis.

The direct evidence of the quantum vortex nucleation is the quantization of circulation. We show that the circulation is quantized in the superconducting (superfluid) phase far from the critical chemical potential, but it is not just above the critical chemical potential. We observe that the quantized circulation is blurred by the quantum fluctuation as the chemical potential is getting close to its critical value. In our simulation, the quantum fluctuation of vortex number is observed, while the averaged circulation is clearly quantized. At first glance, these two facts seem to be incompatible. However, we show that the fluctuation of vortex number behaves as Gaussian and, as a result of cancellation, the average circulation becomes exact integer.

Table of Contents

1	Introduction	1
2	Lattice field theory	7
2.1	Path integral formalism	7
2.2	Spontaneous symmetry breaking	11
3	Complex Langevin method	15
3.1	Stochastic quantization	15
3.2	Fokker-Planck equation	17
3.3	Complex Langevin equation	19
3.4	Numerical simulation	21
4	Nonrelativistic Bose-Einstein condensate	27
4.1	Electromagnetic fields on the lattice	28
4.2	Electric field	30
4.2.1	Minkowski and Euclid electric fields	30
4.2.2	Numerical simulation	31
4.3	Magnetic field	35
4.3.1	Landau level	35
4.3.2	Magnetic flux quantization	39
4.3.3	Numerical simulation	40
4.4	Rotation	47
4.4.1	Bose gas under rotation	47
4.4.2	Numerical simulation	48
5	Relativistic Bose-Einstein condensate	57
5.1	Chemical potential	58
5.2	Electric field	62
5.3	Magnetic field	67
6	Summary and Concluding Remarks	75
	Acknowledgments	79

A Higher order algorithm **81**

B Jackknife method **85**

 B.1 Standard deviation 85

 B.2 Jackknife estimation 85

Chapter 1

Introduction

The Bose-Einstein condensation attracts lots of attention in various areas of physics. It is a novel state of bose gases, in which the macroscopic number of bosons occupies the same quantum state, and thus the quanta scaled by the Planck constant become apparent even in the macroscopic scale. The first direct observation of Bose-Einstein condensation has been achieved in the experiments of liquid helium [1, 2, 3] (reviewed in Ref. [4]). Later, it has also been realized in weakly interacting atomic gases [5, 6, 7] (for a review, see Ref. [8]). The Bose-Einstein condensate created in the cold atom experiments is very close to the original notion of one proposed by Einstein. We show schematic phase diagrams of systems exhibiting the Bose-Einstein condensation in Fig. 1.1(*a, b, and c*), where the superfluid or superconducting phase appears at very low temperatures.

In solid state physics, the superconductivity of metals results from the condensation of Cooper pair, which is a bound state of electrons in momentum space [11]. There are various types of pair condensation in the context of high temperature superconductors [12, 13, 14]. Similarly, the condensation of quasi bosonic-particles such as the exciton, which is a bound state of electron and hole pairs [15, 16, 17], or the magnon [18, 19], which is a collective excitation in spin system, has been actively analyzed both from theories and experiments.

The Bose-Einstein condensation occurs also in nuclear and elementary particle physics (Fig. 1.1(*d*)). In the core of neutron stars, it is considered that the condensate of the Cooper pairs of nucleons or quarks exists [20, 21] (see also Ref. [22]). The nucleons may exhibit anisotropic superfluidity such as the triplet superfluidity because of the spin-orbit coupling [23, 24, 25]. The quarks exhibit the superconductivity in terms of color degrees of freedom [26, 27, 28, 29, 30, 31]. Because of the complexity of the nonabelian gauge interaction and the internal degrees of freedom, the color superconductivity enriches the phase structure of quantum chromodynamics [21]. Also, the condensation of Higgs boson results in the dynamical mass generation of gauge bosons in the Standard Model of particle physics [32, 33, 34]. The Higgs boson has been recently observed at the Large Hadron Collider in CERN 48 years after from its theoretical prediction in 1964 [35, 36]. Now it has been started to analyze the detailed properties of Higgs boson.

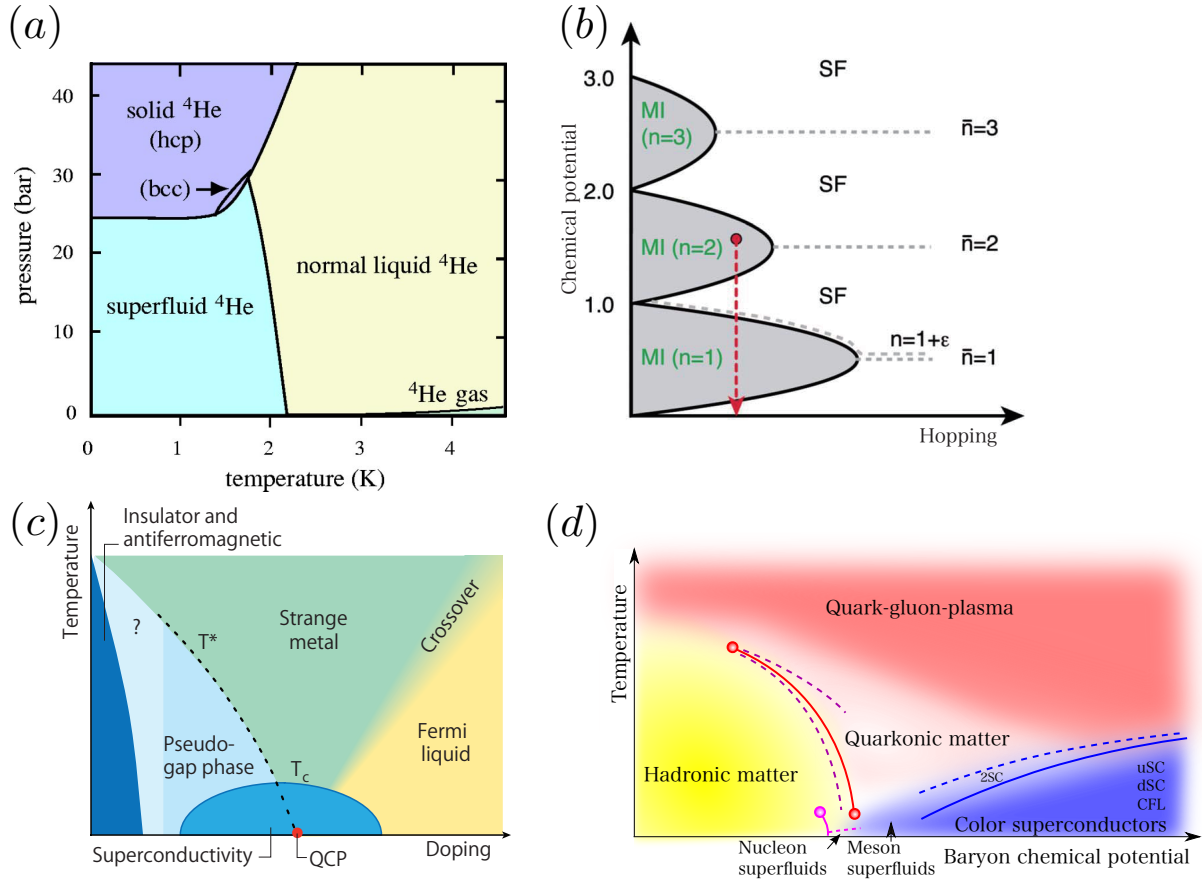


Figure 1.1: Bose-Einstein condensate in branches of physics. (a) Phase diagram of ^4He [4]. (b) Phase diagram of Bose-Hubbard model [8]. (c) Phase diagram of high temperature superconductors [9]. (d) Phase diagram of quantum chromodynamics at finite densities [10]

In the presence of external gauge fields, the Bose-Einstein condensate exhibits topological solitons or topological defects. The topological solitons are solutions of nonlinear field equations homotopically distinct from the trivial vacuum. They are classified by boundary conditions and carry the topological charge. In this sense, the topological solitons are countable like ordinary particles. For example, in type-II superconductors under magnetic field, the penetrating magnetic flux is quantized due to the macroscopic coherence of Bose-Einstein condensate and the quanta form the lattice structure [37, 38, 39, 40], which is referred to as the Abrikosov lattice. As understood from the analogy between magnetism and rotation, the same quantization of vortices and the Abrikosov lattice have been observed in the rotating Bose-Einstein condensate [41, 42, 43, 44, 45]. It has been investigated in detail both from theories and experiments (for a review, see Ref. [46]).

The topological solitons have been analyzed in detail also in the relativistic Bose-Einstein condensate. Our universe has started from extremely hot and dense state, and has been cooled

by its expansion [47, 48, 49]. It has experienced a series of phase transition in the early stage of the expansion [50, 51, 52, 53, 54, 55]. Various topological solitons are considered to be formed when the phase transitions have occurred. Due to their topological nature, these solitons are stable, and thus can be utilized as probes of the phase transitions. Some examples include domain walls [56], magnetic monopoles [57], cosmic strings [58, 59] and so on. Any such topological solitons have not been discovered yet in astronomical observations [60, 61, 62, 63, 64, 65]: Nevertheless, these experiments have been provided strong constraints to the condition of the early universe.

In dilute and low temperature systems, quantum and thermal fluctuations can be negligible, and thus the mean-field approximation works well. Quantum vortex nucleation in such systems can be described by using the Gross-Pitaevskii equation [66, 67]. By numerically solving the real-time evolution of the Gross-Pitaevskii equation, as shown in Fig. 1.2 [68], the authors have analyzed the dynamical mechanism of formation of the Abrikosov lattice in the rotating Bose-Einstein condensate, and they have compared the result with cold atom experiments. However,

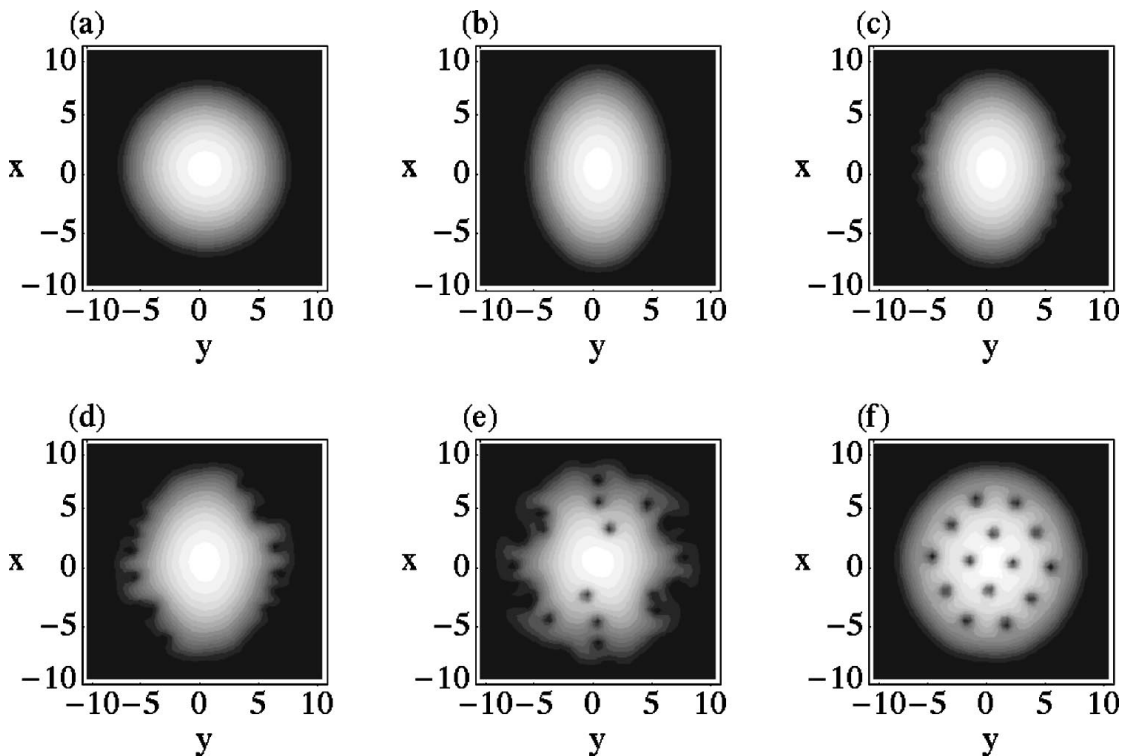


Figure 1.2: Time evolution of condensate density in the rotating trapping potential at $t = 0$ [(a)], 21 [(b)], 107 [(c)], 114 [(d)], 123 [(e)], and 262 ms [(f)]. The figure is taken from Ref. [68].

when quantum or thermal fluctuation cannot be negligible, it is highly nontrivial how such topological solitons behave. Around the critical values of temperature, chemical potential, magnetic field, or angular velocity, the fluctuation grows and the mean-field description inevitably breaks

down [69, 70]. Since high precision measurements are possible in cold atomic experiments, the deviation from the mean-field approximation can be detectable in experiments. Therefore, the ab-initio simulation of quantum vortex nucleation is necessary for definite theoretical prediction without uncertainty.

In this thesis, we present the first ab-initio simulations of such quantum vortex nucleation in the Bose-Einstein condensate under strong external fields [71]. For this purpose, we adopt the complex Langevin method to both nonrelativistic and relativistic boson field theories. This is because, as explicitly shown in the following chapters, the conventional Monte Carlo simulations on the lattice [72, 73, 74, 75, 76, 77] suffer from the notorious sign problem. The Monte Carlo simulation is based on the importance sampling algorithm [78, 79, 80]: We evaluate the path integral in equilibrium states

$$\langle O \rangle = \frac{1}{Z} \int d\varphi^* d\varphi e^{-S_{\text{lat}}} O(\varphi, \varphi^*), \quad (1.1)$$

by means of the ensemble average, which is randomly generated by the probability density $e^{-S_{\text{lat}}}/Z$ with Z being the normalization factor. Its applicability is in some cases very limited, which is referred to as the sign problem. For example, when the lattice action becomes complex, the probability interpretation of the weight $e^{-S_{\text{lat}}}/Z$ breaks down and thus the importance sampling cannot be applied. The complex Langevin method has been developed in relativistic field theories to attack such complex action problem e.g., nonequilibrium system [81, 82, 83], and the phase diagram at finite quark number density [84, 85, 86, 87, 88] (for a review, see Ref. [89]). It is based on the stochastic quantization formalism, instead of the path integral one, and does not necessarily require the action to be real.

We analyze nonrelativistic and relativistic bosons interacting by a repulsive contact interaction under strong external fields such as the electric field, the magnetic field, and the rotation by adopting the complex Langevin method, in which all quantum fluctuations can be properly taken into account. We formulate the nonrelativistic lattice action under rotation in which the chemical potential is introduced on the basis of standard lattice techniques [90, 91], and the angular velocity is introduced by the same manner as magnetic fields [92] with the local centrifugal potential. We numerically show that the superfluid transition occurs as the chemical potential increases. The condensation is calculated from the off-diagonal long-range order of two-point correlation function. The quantization of circulation is clearly seen, which indicates that the vortices are successfully generated in our simulation. To get more information for vortex structure, the size dependence of circulation is calculated, from which we can estimate the typical size of vortex lattice.

This thesis is organized as follows. In Chap. 2, we review the lattice field theory, and how to study the spontaneous symmetry breaking in lattice simulations. In Chap. 3, we review the stochastic quantization using the example of free theory. We summarize the basics to perform the complex Langevin simulation. Application to the nonrelativistic $\lambda\varphi^4$ is also discussed, where we demonstrate the long-range order analysis discussed in Chap. 2. In Chap. 4, we study the

nonrelativistic Bose-Einstein condensate under strong external fields. First, we discuss how to apply external electromagnetic fields on the lattice. Then, the spontaneous $U(1)$ symmetry breaking by the electric field is analyzed. Next, we analyze the quantum vortex nucleation by the magnetic field and by the rotation. We study the effect of quantum fluctuation to the vortex nucleation. In Chap. 5, we study the relativistic Bose-Einstein condensate under strong electromagnetic fields. We show that the particle production by the electric field occurs via the Schwinger mechanism. We also analyze the associated $U(1)$ symmetry breaking. Then, we show the quantum vortex nucleation by the magnetic field in the relativistic system. Chapter 6 is devoted to summary and concluding remarks. In Appendices, we summarize the higher order algorithm to numerically solve the Langevin equation, and the jackknife method to estimate the statistical errors.

Numerical simulations presented in sections 3.4, 4.2.2, 4.3.3, 4.4.2, 5.2, and 5.3 are based on our original work [71] in collaboration with Arata Yamamoto.

Chapter 2

Lattice field theory

In this chapter, we review the formulation of quantum field theories on the lattice. The partition function in the grand canonical ensemble is represented by the path integral over field variables on the lattice. We also review how to discuss the spontaneous symmetry breaking in practical simulations. The spontaneous symmetry breaking occurs only in the thermodynamic limit and thus the order parameter always vanishes unless the symmetry is explicitly broken [93]. Since it is not easy to manage the noncommutative thermodynamic and zero external field limits in practical simulations, we introduce an alternative way to study the spontaneous symmetry breaking, that is, observing the nonvanishing long-range order [94]. We also show that the Bose-Einstein condensate implies the spontaneous U(1) symmetry breaking.

2.1 Path integral formalism

We start with the partition function in the grand canonical ensemble,

$$Z = \text{tr} e^{-\beta(\hat{H} - \mu\hat{Q})}, \quad (2.1)$$

where $\beta = 1/T$ and μ are inverse temperature and chemical potential, respectively. H is the Hamiltonian of the system and Q is a charge. We use the hat symbol to indicate quantum operators. As an example, let us consider bosons interacting by a repulsive contact interaction. The Hamiltonian and charge (particle number) operators are, respectively, given as

$$\hat{H} = \int d^3x \hat{\varphi}_x^\dagger \left(-\frac{\nabla^2}{2m} \right) \hat{\varphi}_x + \frac{\lambda}{4} \hat{\varphi}_x^\dagger \hat{\varphi}_x^\dagger \hat{\varphi}_x \hat{\varphi}_x, \quad (2.2)$$

$$\hat{Q} = \int d^3x \hat{\varphi}_x^\dagger \hat{\varphi}_x, \quad (2.3)$$

where $\hat{\varphi}_x$ and $\hat{\varphi}_x^\dagger$ are annihilation and creation operators of bosons and satisfy

$$[\hat{\varphi}_x, \hat{\varphi}_{x'}^\dagger] = \delta(\mathbf{x} - \mathbf{x}'). \quad (2.4)$$

We rewrite the partition function (2.1) by using the coherent states $|\varphi\rangle$, which are eigenstates of annihilation operators:

$$\hat{\varphi}_{\mathbf{x}}|\varphi\rangle = \varphi_{\mathbf{x}}|\varphi\rangle, \quad (2.5)$$

$$\langle\varphi|\hat{\varphi}_{\mathbf{x}}^\dagger = \langle\varphi|\varphi_{\mathbf{x}}^*, \quad (2.6)$$

and are given explicitly as

$$|\varphi\rangle = e^{\int d^3x \varphi_{\mathbf{x}} \hat{\varphi}_{\mathbf{x}}^\dagger} |0\rangle, \quad (2.7)$$

where $|0\rangle$ is the Fock vacuum. The coherent states are over completed, so that the closure relation is different from that of the standard complete set and reads

$$\int \prod_{\mathbf{x}} \frac{d\varphi_{\mathbf{x}}^* d\varphi_{\mathbf{x}}}{2\pi i} e^{-\int d^3x \varphi_{\mathbf{x}}^* \varphi_{\mathbf{x}}} |\varphi\rangle \langle\varphi| = 1. \quad (2.8)$$

Eq. (2.8) can be easily checked by applying it to a coherent state $|\varphi'\rangle$:

$$\left(\int \prod_{\mathbf{x}} \frac{d\varphi_{\mathbf{x}}^* d\varphi_{\mathbf{x}}}{2\pi i} e^{-\int d^3x \varphi_{\mathbf{x}}^* \varphi_{\mathbf{x}}} |\varphi\rangle \langle\varphi| \right) |\varphi'\rangle = |\varphi'\rangle. \quad (2.9)$$

By using the coherent states, we have

$$\begin{aligned} \text{tr } \hat{O} &= \sum_n \langle n | \hat{O} | n \rangle \\ &= \int \prod_{\mathbf{x}} \frac{d\varphi_{\mathbf{x}}^* d\varphi_{\mathbf{x}}}{2\pi i} e^{-\int d^3x \varphi_{\mathbf{x}}^* \varphi_{\mathbf{x}}} \langle\varphi | \hat{O} | \varphi\rangle, \end{aligned} \quad (2.10)$$

where $|n\rangle$ is a complete set and we used the closure relation $\sum_n |n\rangle \langle n| = 1$ to obtain the last line. Then, the partition function (2.1) reads

$$\begin{aligned} Z &= \text{tr} \prod_{j=1}^N e^{-\Delta\tau_j (\hat{H} - \mu \hat{Q})} \\ &= \prod_{j=1}^N \int \prod_{\mathbf{x}} \frac{d\varphi_{j\mathbf{x}}^* d\varphi_{j\mathbf{x}}}{2\pi i} e^{-\int d^3x \varphi_{j\mathbf{x}}^* \varphi_{j\mathbf{x}}} \\ &\quad \times \langle\varphi_N | e^{-\Delta\tau_N (\hat{H} - \mu \hat{Q})} | \varphi_{N-1} \rangle \cdots \langle\varphi_1 | e^{-\Delta\tau_1 (\hat{H} - \mu \hat{Q})} | \varphi_N \rangle \end{aligned} \quad (2.11)$$

where $\Delta\tau_j (= \Delta\tau) = \beta/N$. We consider the $N \rightarrow \infty$ ($\Delta\tau \rightarrow 0$) limit and then the matrix elements are evaluated as

$$\begin{aligned} \langle\varphi_j | e^{-\Delta\tau (\hat{H} - \mu \hat{Q})} | \varphi_{j-1} \rangle &= \langle\varphi_j | \left(1 - \Delta\tau (\hat{H} - \mu \hat{Q}) \right) | \varphi_{j-1} \rangle + \mathcal{O}(\Delta\tau^2) \\ &= \langle\varphi_j | \varphi_{j-1} \rangle (1 - \Delta\tau (H_{j,j-1} - \mu Q_{j,j-1})) + \mathcal{O}(\Delta\tau^2) \\ &= e^{\int d^3x \varphi_{j\mathbf{x}}^* \varphi_{j-1\mathbf{x}}} e^{-\Delta\tau (H_{j,j} - \mu Q_{j,j})} + \mathcal{O}(\Delta\tau^2), \end{aligned} \quad (2.12)$$

where $\varphi_{0\mathbf{x}} = \varphi_{N\mathbf{x}}$ and

$$\begin{aligned} H_{j,j-1} - \mu Q_{j,j-1} &= \int d^3x \varphi_{j\mathbf{x}}^* \left(-\frac{\nabla^2}{2m} - \mu \right) \varphi_{j-1\mathbf{x}} + \frac{\lambda}{4} \varphi_{j\mathbf{x}}^* \varphi_{j\mathbf{x}}^* \varphi_{j-1\mathbf{x}} \varphi_{j-1\mathbf{x}} \\ &= H_{j,j} - \mu Q_{j,j} + \mathcal{O}(\Delta\tau). \end{aligned} \quad (2.13)$$

We used the inner product between coherent states

$$\langle \varphi | \varphi' \rangle = e^{\int d^3x \varphi_{\mathbf{x}}^* \varphi'_{\mathbf{x}}}, \quad (2.14)$$

which is obtained from Eqs. (2.4) and (2.7). Finally, we have

$$Z = \int \prod_{j,\mathbf{x}} \frac{d\varphi_{j\mathbf{x}}^* d\varphi_{j\mathbf{x}}}{2\pi i} e^{-\Delta\tau \sum_j \int d^3x \varphi_{j\mathbf{x}}^* (\varphi_{j\mathbf{x}} - \varphi_{j-1\mathbf{x}}) / \Delta\tau + H_{j,j} - \mu Q_{j,j}} + \mathcal{O}(\Delta\tau^2). \quad (2.15)$$

Therefore, the partition function (2.1) reads

$$Z = \mathcal{N} \int \mathcal{D}\varphi e^{-S}, \quad (2.16)$$

$$S = \int_0^\beta d\tau d^3x \varphi_{\tau,\mathbf{x}}^* \left(\partial_\tau - \frac{\nabla^2}{2m} - \mu \right) \varphi_{\tau,\mathbf{x}} + \frac{\lambda}{4} \varphi_{\tau,\mathbf{x}}^* \varphi_{\tau,\mathbf{x}}^* \varphi_{\tau,\mathbf{x}} \varphi_{\tau,\mathbf{x}}, \quad (2.17)$$

in the limit of $N \rightarrow \infty$ with $\mathcal{D}\varphi = \prod_{\tau,\mathbf{x}} d\varphi_{\tau,\mathbf{x}}^* d\varphi_{\tau,\mathbf{x}}$, and \mathcal{N} being the normalization factor. The condition $\varphi_{0\mathbf{x}} = \varphi_{N\mathbf{x}}$ imposes the periodic boundary condition, $\varphi_{0\mathbf{x}} = \varphi_{\beta\mathbf{x}}$, to Eq. (2.16).

Expectation values can also be written in the path integral form. For example, charge density, which is defined as

$$\begin{aligned} n &= \lim_{V \rightarrow \infty} \frac{\text{tr} e^{-\beta(\hat{H} - \mu\hat{Q})} \hat{Q} / V}{\text{tr} e^{-\beta(\hat{H} - \mu\hat{Q})}} \\ &= \lim_{V \rightarrow \infty} \frac{1}{\beta V} \frac{\partial}{\partial \mu} \log Z, \end{aligned} \quad (2.18)$$

reads

$$n = \lim_{V \rightarrow \infty} \frac{1}{Z} \int \mathcal{D}\varphi e^{-S} \frac{1}{\beta V} \int_0^\beta d\tau d^3x \varphi_{\tau,\mathbf{x}}^* \varphi_{\tau,\mathbf{x}}, \quad (2.19)$$

where V is the spatial volume. The expectation value in the ground state can be obtained by taking the $\beta \rightarrow \infty$ ($T \rightarrow 0$) limit in addition to the thermodynamic limit, $V \rightarrow \infty$. In the following discussions, we calculate various type of propagators, which are defined as

$$\begin{aligned} G(\tau, \mathbf{x}; \tau' \mathbf{y}) &= \langle \text{T}[\hat{O}(\tau, \mathbf{x}), \hat{O}^\dagger(\tau', \mathbf{y})] \rangle \\ &= \frac{1}{Z} \int \mathcal{D}\varphi e^{-S} O_{\tau,\mathbf{x}} O_{\tau',\mathbf{y}}^\dagger, \end{aligned} \quad (2.20)$$

where T denotes a time ordered product and O is some local operator. The most simple propagator is obtained by $O = \varphi$. In the free theory, it is given explicitly as

$$\langle \text{T}[\varphi(\tau, \mathbf{x}), \varphi^*(\tau', \mathbf{x}')] \rangle = \frac{1}{\partial_\tau - \mu - \nabla^2/2m} \delta(\tau - \tau') \delta^{(3)}(\mathbf{x} - \mathbf{x}'). \quad (2.21)$$

We can calculate the free boson propagator as follows. First, we define the generating functional $Z(j^*, j)$ as

$$Z(j^*, j) = \mathcal{N} \int \mathcal{D}\varphi e^{-S + \int d\tau d^3x (j_{\tau, \mathbf{x}}^* \varphi_{\tau, \mathbf{x}} + \varphi_{\tau, \mathbf{x}}^* j_{\tau, \mathbf{x}})}. \quad (2.22)$$

In the free theory, we have

$$\begin{aligned} S - \int d\tau d^3x (j_{\tau, \mathbf{x}}^* \varphi_{\tau, \mathbf{x}} + \varphi_{\tau, \mathbf{x}}^* j_{\tau, \mathbf{x}}) \\ = \int d\tau d^3x d\tau' d^3y \left(\varphi_{\tau, \mathbf{x}}^* - (j^* \Delta_F)_{\tau, \mathbf{x}} \right) \mathcal{D}_{\tau, \mathbf{x}; \tau', \mathbf{y}} \left(\varphi_{\tau', \mathbf{y}} - (\Delta_F j)_{\tau', \mathbf{y}} \right) \\ - j_{\tau, \mathbf{x}}^* \Delta_F(\tau, \mathbf{x}; \tau', \mathbf{y}) j_{\tau', \mathbf{y}}, \end{aligned} \quad (2.23)$$

where \mathcal{D} is a matrix operator:

$$\mathcal{D}_{\tau, \mathbf{x}; \tau', \mathbf{y}} = \left(\partial_\tau - \frac{\nabla^2}{2m} - \mu \right) \delta(\tau - \tau') \delta^{(3)}(\mathbf{x} - \mathbf{y}). \quad (2.24)$$

Δ_F is the inverse of \mathcal{D} and satisfies

$$\int d\tau'' d^3z \mathcal{D}_{\tau, \mathbf{x}; \tau'', \mathbf{z}} \Delta_F(\tau'', \mathbf{z}; \tau', \mathbf{y}) = \delta(\tau - \tau') \delta^{(3)}(\mathbf{x} - \mathbf{y}), \quad (2.25)$$

or equivalently,

$$\left(\partial_\tau - \frac{\nabla^2}{2m} - \mu \right) \Delta_F(\tau, \mathbf{x}; \tau', \mathbf{y}) = \delta(\tau - \tau') \delta^{(3)}(\mathbf{x} - \mathbf{y}). \quad (2.26)$$

$(j^* \Delta_F)$ and $(\Delta_F j)$ are

$$(j^* \Delta_F)_{\tau, \mathbf{x}} = \int d\tau' d^3z j_{\tau', \mathbf{z}}^* \Delta_F(\tau', \mathbf{z}; \tau, \mathbf{x}), \quad (2.27)$$

$$(\Delta_F j)_{\tau, \mathbf{x}} = \int d\tau' d^3z \Delta_F(\tau, \mathbf{x}; \tau', \mathbf{z}) j_{\tau', \mathbf{z}}. \quad (2.28)$$

Thus, the path integral in Eq. (2.22) is Gaussian integral and can be calculated exactly:

$$Z(j^*, j) = \mathcal{N}' e^{\int d\tau d^3x d\tau' d^3y j_{\tau, \mathbf{x}}^* \Delta_F j_{\tau', \mathbf{y}}}. \quad (2.29)$$

The boson propagator is obtained by taking the functional derivatives:

$$\begin{aligned} \langle T[\varphi(\tau, \mathbf{x}), \varphi^*(\tau', \mathbf{y})] \rangle &= \frac{1}{Z(j^*, j)} \frac{\delta^2}{\delta j_{\tau, \mathbf{x}}^* \delta j_{\tau', \mathbf{y}}} Z(j^*, j) \\ &= \Delta_F(\tau, \mathbf{x}; \tau', \mathbf{y}), \end{aligned} \quad (2.30)$$

and then we obtain Eq. (2.21).

Now, we formulate Eqs. (2.16) and (2.17) on the lattice. $\varphi_{\tau, \mathbf{x}}$ and $\varphi_{\tau, \mathbf{x}}^*$ are defined on the four-dimensional hypercubic lattice, where τ and \mathbf{x} are discretized as $(\mathbf{x}, \tau) = (i_x a, i_y a, i_z a, i_\tau a)$ with a being the lattice spacing. The total number of lattice sites is $N_x N_y N_z \times N_\tau$. We impose

the periodic boundary conditions to all four directions. The partition function is given by the integral over all field variables on the lattices:

$$Z = \mathcal{N} \int \prod_{\tau, \mathbf{x}} d\varphi_{\tau, \mathbf{x}}^* d\varphi_{\tau, \mathbf{x}} e^{-S_{\text{lat}}}. \quad (2.31)$$

The lattice-discretized action S_{lat} reads

$$S_{\text{lat}} = a^3 \sum_{\tau, \mathbf{x}} \left[\varphi_{\tau, \mathbf{x}}^* (\varphi_{\tau, \mathbf{x}} - e^{\mu a} \varphi_{\tau-a, \mathbf{x}}) - \frac{1}{2ma} \sum_i \left(\varphi_{\tau, \mathbf{x}+\hat{i}a}^* \varphi_{\tau, \mathbf{x}} + \varphi_{\tau, \mathbf{x}}^* \varphi_{\tau, \mathbf{x}+\hat{i}a} - 2|\varphi_{\tau, \mathbf{x}}|^2 \right) + \frac{1}{2} \frac{\lambda}{a^2} a^3 |\varphi_{\tau, \mathbf{x}}|^4 \right], \quad (2.32)$$

where \hat{i} denote unit vectors in the x_i direction. Then, the continuum theory is defined as the $a \rightarrow 0$ limit. The thermodynamic limit is obtained by $N_{i=x,y,z} \rightarrow \infty$ with fixed a . Also, the zero temperature theory is obtained by $N_\tau \rightarrow \infty$ with fixed a .

To discretize Eq. (2.17), there are several choices of lattice actions, which have the same continuum limit (2.17). This variety comes from the choice of forward, backward, and central differences, how to apply external fields on the lattice, and so on. We employ the backward difference. We apply external fields, so as for the lattice action to keep the symmetry of the continuum action. For example, we can introduce the chemical potential by adding $-\mu \varphi_{\tau, \mathbf{x}}^* \varphi_{\tau, \mathbf{x}}$ to the lattice action, instead of exponential term in Eq. (2.32). They correspond to each other in the limit of $a \rightarrow 0$. Since the chemical potential is an external field coupled to the U(1) symmetry (the particle number symmetry), we should introduce it as (a kind of) U(1) gauge field on the lattice, which is the exponential term in Eq. (2.32). The same problem appears in the case of other external fields such as electric or magnetic field, which will be discussed in detail in the following chapters. We remark here that these choices of external fields affects the renormalization of numerical results, not just a formal problem.

2.2 Spontaneous symmetry breaking

In finite dimensional systems, the spontaneous symmetry breaking does not occur and thus its order parameter vanishes [93]. To study the spontaneous symmetry breaking, we need to introduce an external field, which explicitly breaks the symmetry and consider the zero external field limit after taking the extrapolation to the thermodynamic limit. More specifically, the order parameter h is defined as

$$\lim_{J \rightarrow 0} \lim_{V \rightarrow \infty} \langle 0_J | [i\hat{Q}, \hat{\psi}] | 0_J \rangle = h \neq 0, \quad (2.33)$$

where Q is the broken charge and ψ is some local orator, which is referred to as symmetry breaking operator. $|0_J\rangle$ is the groundstate at finite external field J . If these limits are commutable, the order parameter vanishes because the ground state is singlet at zero external field, that is,

$Q|0\rangle = 0$. Therefore, non-analyticity with respect to J , which comes from the thermodynamic limit, characterizes the spontaneous symmetry breaking. The spontaneous symmetry breaking at finite temperature can also be discussed in the same way, where the vacuum expectation value is replaced by the ensemble average with the density matrix $\exp(-\beta\hat{H} - \beta J\hat{\psi})$. We note that the symmetry breaking operator ψ is not unique and thus h is also not.

We need to manage these two noncommutative limits carefully and thus it is not easy to calculate the order parameter in practical simulations. In the following numerical simulation, instead of directly calculating Eq. (2.33), we define the spontaneous symmetry breaking by the long range order [94]. In the Monte Carlo or complex Langevin simulation, all the infinitely degenerate vacua appear in the ensemble unless the symmetry is explicitly broken. Then, the order parameter is averaged over them:

$$\begin{aligned}\langle 0|\hat{h}|0\rangle &\sim \int d\theta P_\theta \langle 0_\theta|\hat{h}|0_\theta\rangle / \int d\theta P_\theta \\ &= \int d\theta P_\theta |h| e^{i\theta} / \int d\theta P_\theta,\end{aligned}\tag{2.34}$$

where θ is the phase of order parameter and $|0_\theta\rangle$ is one of the degenerate vacua in which the order parameter has the phase θ . The θ dependence is canceled over the ensemble average (the degenerate vacua) and Eq. (2.34) goes to zero since there is no preferred θ direction in the numerical simulations. To avoid this, we calculate the two point correlation function of order parameter field h . Because of the cluster decomposition principle [95, 96], the long-range behavior of correlation function reads

$$\langle 0|\hat{h}(\mathbf{x})\hat{h}^\dagger(\mathbf{y})|0\rangle \rightarrow |\langle 0|\hat{h}|0\rangle|^2\tag{2.35}$$

in the limit of $|\mathbf{x} - \mathbf{y}| \rightarrow \infty$, where we assume the translational symmetry of vacuum. Now, since the right hand side is independent of θ , it does not vanish by taking the average over the degenerate vacua:

$$\begin{aligned}|\langle 0|\hat{h}|0\rangle|^2 &\sim \int d\theta P_\theta |\langle 0_\theta|\hat{h}|0_\theta\rangle|^2 / \int d\theta P_\theta \\ &= |h|^2\end{aligned}\tag{2.36}$$

Thus, we can define the spontaneous symmetry breaking whether the two point correlation function of order parameter fields goes to zero or goes to finite constant value, which is directly checked on the lattice simulations.

In the case of the spontaneous U(1) symmetry breaking, the long range order also means the macroscopic occupation of ground state, that is, the Bose-Einstein condensation. This is

because the two point correlation function of the order parameter field φ is written as

$$\begin{aligned}
G(\mathbf{x}, \mathbf{y}) &= \langle 0 | \hat{\varphi}^\dagger(\mathbf{x}) \hat{\varphi}(\mathbf{y}) | 0 \rangle \\
&= \frac{1}{V} \sum_{\mathbf{k}, \mathbf{k}'} e^{-i\mathbf{k}\cdot\mathbf{x} + i\mathbf{k}'\cdot\mathbf{y}} \langle 0 | a_{\mathbf{k}}^\dagger a_{\mathbf{k}'} | 0 \rangle \\
&= \frac{1}{V} \langle 0 | a_{\mathbf{k}=0}^\dagger a_{\mathbf{k}=0} | 0 \rangle + \frac{1}{V} \sum_{\mathbf{k} \neq 0} e^{-i\mathbf{k}\cdot(\mathbf{x}-\mathbf{y})} \langle 0 | a_{\mathbf{k}}^\dagger a_{\mathbf{k}} | 0 \rangle,
\end{aligned} \tag{2.37}$$

where $a_{\mathbf{k}}$ and $a_{\mathbf{k}}^\dagger$ are, respectively, the annihilation and creation operator of particles with momentum \mathbf{k} . Here, we assume the translational invariance of the vacuum, so that

$$\langle 0 | a_{\mathbf{k}}^\dagger a_{\mathbf{k}'} | 0 \rangle = \delta_{\mathbf{k}\mathbf{k}'} \langle 0 | a_{\mathbf{k}}^\dagger a_{\mathbf{k}} | 0 \rangle. \tag{2.38}$$

The second term in Eq. (2.37) rapidly oscillates in the limit of $|\mathbf{x} - \mathbf{y}| \rightarrow \infty$ and goes to zero. Then, if the U(1) symmetry is spontaneously broken, we have

$$\frac{\langle \hat{N}_{\mathbf{k}=0} \rangle}{V} = |\varphi|^2 \neq 0, \tag{2.39}$$

where $\hat{N}_{\mathbf{k}=0}$ is number operator, which counts the number of particles with momentum $\mathbf{k} = 0$. This means that the zero momentum state is occupied by the number of particles comparable to the system size, that is, $\langle N_{\mathbf{k}=0} \rangle \sim V$. Therefore, the Bose-Einstein condensation occurs when the U(1) symmetry is spontaneously broken.

Chapter 3

Complex Langevin method

In this chapter, we first review the stochastic quantization formalism, namely, the formulation of quantum field theories on the basis of the classical Langevin equation along the fictitious time direction, which was proposed by Parisi and Wu in 1981 [97, 98, 99] (for a review, see Ref. [100]). Based on Ref. [99], we also review the general relation between the stochastic and path integral formalisms from which we can understand how the Langevin method reproduces the standard Monte Carlo simulation. Then, we summarize the basis to perform the complex Langevin simulation in which the quantization procedure in the stochastic quantization formalism is numerically performed on the lattice. As an example of numerical simulation, we present our original work [71] in which we have applied the complex Langevin method to the nonrelativistic bose system interacting by a repulsive contact interaction. This is the first application of the complex Langevin method to a condensed matter system, which suffers from the sign problem. We show that the Silver Blaze phenomena [101] is correctly managed in our simulation. Also, we analyze the spontaneous breaking of U(1) symmetry by performing the long-range order analysis discussed in Sec. 2.2.

3.1 Stochastic quantization

We start with the nonrelativistic free boson propagator in $(1 + 3)$ -dimensional Euclid space, which is given explicitly as

$$\langle T[\varphi(\tau, \mathbf{x}), \varphi^*(\tau', \mathbf{x}')] \rangle = \frac{1}{\partial_\tau - \nabla^2/2m} \delta(\tau - \tau') \delta^{(3)}(\mathbf{x} - \mathbf{x}'), \quad (3.1)$$

where T denotes a time ordered product. In the stochastic quantization formalism [97, 98, 99] (for a review, see Ref. [100]), the propagator (3.1) is retrieved by the noise average of the solution of the Langevin equation along the fictitious time direction. We solve the Langevin equation along the fifth direction θ :

$$\partial_\theta \varphi_{\tau, \mathbf{x}}(\theta) = -\frac{\partial S}{\partial \varphi_{\tau, \mathbf{x}}^*} + \eta_{\tau, \mathbf{x}}(\theta), \quad (3.2)$$

where S is the action in $(1 + 3)$ -dimensional Euclid space, which is given explicitly as

$$S = \int d\tau d^3x \varphi^* (\partial_\tau - \nabla^2/2m) \varphi, \quad (3.3)$$

in the case of free theory. $\eta_{\tau,\mathbf{x}}(\theta)$ are Gaussian noises and the average over $\eta_{\tau,\mathbf{x}}(\theta)$ satisfies

$$\begin{aligned} \langle \eta_{\tau,\mathbf{x}}(\theta) \rangle_\eta &= \langle \eta_{\tau,\mathbf{x}}^*(\theta) \rangle_\eta = 0, \\ \langle \eta_{\tau,\mathbf{x}}(\theta) \eta_{\tau',\mathbf{x}'}(\theta') \rangle_\eta &= \langle \eta_{\tau,\mathbf{x}}^*(\theta) \eta_{\tau',\mathbf{x}'}^*(\theta') \rangle_\eta = 0, \\ \langle \eta_{\tau,\mathbf{x}}(\theta) \eta_{\tau',\mathbf{x}'}^*(\theta') \rangle_\eta &= 2\delta(\theta - \theta') \delta(\tau - \tau') \delta^{(3)}(\mathbf{x} - \mathbf{x}'). \end{aligned} \quad (3.4)$$

In the free theory, we can formally solve Eq. (3.2) and obtain

$$\varphi_{\tau,\mathbf{x}}(\theta) = \int_0^\theta d\theta' e^{-[\partial_\tau - \nabla^2/2m](\theta - \theta')} \eta_{\tau,\mathbf{x}}(\theta'), \quad (3.5)$$

where we chose $\varphi_{\tau,\mathbf{x}}(0) = 0$ as an initial condition to solve Eq. (3.2). After taking the stochastic average, the two point correlation of $\varphi_{\tau,\mathbf{x}}(\theta)$ reads

$$\langle \varphi_{\tau,\mathbf{x}}(\theta) \varphi_{\tau',\mathbf{x}'}^*(\theta') \rangle_\eta = \frac{1}{\partial_\tau - \nabla^2/2m} \left[1 - e^{-2(\partial_\tau - \nabla^2/2m)\theta} \right] \delta(\tau - \tau') \delta^{(3)}(\mathbf{x} - \mathbf{x}'). \quad (3.6)$$

The exponential term monotonically drops off as θ increases, so that Eq. (3.6) recovers the free boson propagator (3.1) in the limit of $\theta \rightarrow \infty$. Since Eq. (3.2) is a diffusion equation along θ direction, this limit is nothing but the equilibrium solution of Eq. (3.2). Multiple-point correlation functions are also obtained from equal stochastic-time correlation functions as

$$\begin{aligned} &\langle \mathbb{T}[\varphi(\tau_1, \mathbf{x}_1), \dots, \varphi(\tau_n, \mathbf{x}_n), \varphi^*(\tau'_1, \mathbf{x}'_1), \dots, \varphi^*(\tau'_n, \mathbf{x}'_n)] \rangle \\ &= \lim_{\theta \rightarrow \infty} \langle \varphi_{\tau_1, \mathbf{x}_1}(\theta) \cdots \varphi_{\tau_n, \mathbf{x}_n}(\theta) \varphi_{\tau'_1, \mathbf{x}'_1}^*(\theta) \cdots \varphi_{\tau'_n, \mathbf{x}'_n}^*(\theta) \rangle_\eta. \end{aligned} \quad (3.7)$$

The generalization to interacting theories is straightforward. Now we solve the Langevin equation (3.2) with interaction terms. For example, in the nonrelativistic bose gas interacting by a repulsive contact interaction, the Langevin equation reads

$$\partial_\theta \varphi_{\tau,\mathbf{x}} = - (\partial_\tau - \nabla^2/2m) \varphi_{\tau,\mathbf{x}} - \lambda \varphi_{\tau,\mathbf{x}}^* \varphi_{\tau,\mathbf{x}}^2 + \eta_{\tau,\mathbf{x}}. \quad (3.8)$$

The noise terms are the same as those in the free theory and satisfy Eq. (3.4). The expectation value of observable is obtained by using the equilibrium solution of Eq. (3.2) or (3.8) as

$$\langle O \rangle = \lim_{\theta \rightarrow \infty} \langle O(\varphi^*, \varphi) \rangle_\eta, \quad (3.9)$$

where the operator is written in terms of φ with the fictitious time θ . Although the noise is trivial Gaussian, because of interactions, non-linear contractions between η are generated by solving the evolution along the θ direction, and thus we can completely recover correlation functions in interacting quantum field theories.

We remark here that as in the case of Monte Carlo simulation, some observables are not able to be directly calculated by using the complex Langevin method. As is clear from our introduction of the stochastic quantization, we can only calculate correlation functions by using the stochastic average of solutions of classical equation of motion. Therefore, the generating functional (the integral measure in terms of path integral formalism) and thus the thermodynamic quantities such as free energy, or pressure are not easy to calculate also in the complex Langevin simulation.

3.2 Fokker-Planck equation

Now that we have reached a stochastic description of the correlation functions, let us deepen our insight from the general relation between this formalism and the path integral formalism. We show that the path integral measure of Euclid field theory is retrieved by the stochastic formalism through the Fokker-Planck equation. From that, we can see that the (complex) Langevin method is an alternative way to generate the ensemble of equilibrium states.

Let us define a distribution $P(\theta, \varphi^*, \varphi)$, which reproduces the stochastic average of O at finite θ as

$$\langle O(\varphi^* = \varphi_\eta^*(\theta), \varphi = \varphi_\eta(\theta)) \rangle_\eta = \int d\varphi^* d\varphi P(\theta, \varphi^*, \varphi) O(\varphi^*, \varphi), \quad (3.10)$$

where φ_η denotes a solution of the Langevin equation (3.2). The θ dependence of $\langle O \rangle_\eta$ reads

$$\begin{aligned} \frac{\partial}{\partial \theta} \langle O \rangle_\eta &= \left\langle \left(\partial_\theta \varphi_\eta \frac{\partial}{\partial \varphi} + \partial_\theta \varphi_\eta^* \frac{\partial}{\partial \varphi^*} \right) O \right\rangle_\eta \\ &= \left\langle \left(\left(-\frac{\partial S}{\partial \varphi^*} + \eta \right) \frac{\partial}{\partial \varphi} + \left(-\frac{\partial S}{\partial \varphi} + \eta^* \right) \frac{\partial}{\partial \varphi^*} \right) O \right\rangle_\eta \\ &= \left\langle \left(\left(-\frac{\partial S}{\partial \varphi^*} + \frac{\partial}{\partial \varphi^*} \right) \frac{\partial}{\partial \varphi} + \left(-\frac{\partial S}{\partial \varphi} + \frac{\partial}{\partial \varphi} \right) \frac{\partial}{\partial \varphi^*} \right) O \right\rangle_\eta. \end{aligned} \quad (3.11)$$

To obtain the last line, we used the following equations:

$$\begin{aligned} \langle \eta \frac{\partial}{\partial \varphi_\eta} O \rangle_\eta &= \int d\eta^* d\eta e^{-\eta^* \eta} \frac{\partial}{\partial \varphi} O(\varphi^* = \varphi_\eta^*, \varphi = \varphi_\eta) \\ &= \int d\eta^* d\eta (-\partial_{\eta^*}) e^{-\eta^* \eta} \frac{\partial}{\partial \varphi} O \\ &= \int d\eta^* d\eta e^{-\eta^* \eta} \left(\frac{\partial \varphi_\eta^*}{\partial \eta^*} \frac{\partial}{\partial \varphi^*} \right) \frac{\partial}{\partial \varphi} O \\ &= \left\langle \frac{\partial}{\partial \varphi^*} \frac{\partial}{\partial \varphi} O \right\rangle_\eta, \end{aligned} \quad (3.12)$$

and

$$\frac{\partial \varphi_\eta}{\partial \eta} = \frac{\partial \varphi_\eta^*}{\partial \eta^*} = 1, \quad (3.13)$$

which is a prescription of stochastic derivatives and our convention is clear from Eq. (3.5). By using $P(\theta, \varphi)$, Eq. (3.12) is written as :

$$\begin{aligned} \frac{\partial}{\partial \theta} \langle O \rangle_\eta &= \int d\varphi^* d\varphi P \left(\left(-\frac{\partial S}{\partial \varphi^*} + \frac{\partial}{\partial \varphi^*} \right) \frac{\partial}{\partial \varphi} + \left(-\frac{\partial S}{\partial \varphi} + \frac{\partial}{\partial \varphi} \right) \frac{\partial}{\partial \varphi^*} \right) O \\ &= \int d\varphi^* d\varphi \left(2 \frac{\partial^2 S}{\partial \varphi^* \partial \varphi} + \frac{\partial S}{\partial \varphi^*} \frac{\partial}{\partial \varphi} + \frac{\partial S}{\partial \varphi} \frac{\partial}{\partial \varphi^*} + 2 \frac{\partial^2}{\partial \varphi^* \partial \varphi} \right) P O \\ &= \int d\varphi^* d\varphi \left(\frac{\partial}{\partial \varphi} \left(\frac{\partial S}{\partial \varphi^*} + \frac{\partial}{\partial \varphi^*} \right) + \frac{\partial}{\partial \varphi^*} \left(\frac{\partial S}{\partial \varphi} + \frac{\partial}{\partial \varphi} \right) \right) P O. \end{aligned} \quad (3.14)$$

Now, the θ dependence of $P(\theta, \varphi)$ reads

$$\partial_\theta P = \left(\frac{\partial}{\partial \varphi} \left(\frac{\partial}{\partial \varphi^*} + \frac{\partial S}{\partial \varphi^*} \right) + \frac{\partial}{\partial \varphi^*} \left(\frac{\partial}{\partial \varphi} + \frac{\partial S}{\partial \varphi} \right) \right) P. \quad (3.15)$$

This is the so called Focker-Planck equation. Eq.(3.15) is written as

$$\partial_\theta \tilde{P} = - \left[\left(-\frac{\partial}{\partial \varphi^*} + \frac{1}{2} \frac{\partial S}{\partial \varphi^*} \right) \left(\frac{\partial}{\partial \varphi} + \frac{1}{2} \frac{\partial S}{\partial \varphi} \right) + \left(-\frac{\partial}{\partial \varphi} + \frac{1}{2} \frac{\partial S}{\partial \varphi} \right) \left(\frac{\partial}{\partial \varphi^*} + \frac{1}{2} \frac{\partial S}{\partial \varphi^*} \right) \right] \tilde{P}, \quad (3.16)$$

where $P = \tilde{P} e^{-S/2}$. Let us assume the action is real, that is, $S = S^\dagger$ and then the stochastic time evolution operator of \tilde{P} ,

$$H = \left(-\frac{\partial}{\partial \varphi^*} + \frac{1}{2} \frac{\partial S}{\partial \varphi^*} \right) \left(\frac{\partial}{\partial \varphi} + \frac{1}{2} \frac{\partial S}{\partial \varphi} \right) + \left(-\frac{\partial}{\partial \varphi} + \frac{1}{2} \frac{\partial S}{\partial \varphi} \right) \left(\frac{\partial}{\partial \varphi^*} + \frac{1}{2} \frac{\partial S}{\partial \varphi^*} \right), \quad (3.17)$$

becomes semi-positive definite, since $H = H^\dagger$. Therefore, without depending on initial conditions, the asymptotic behavior of \tilde{P} in the limit of $\theta \rightarrow \infty$ is given by the eigenstate of H with zero eigenvalue, which is obtained from

$$\left(\frac{\partial}{\partial \varphi} + \frac{1}{2} \frac{\partial S}{\partial \varphi} \right) \Psi = 0, \quad (3.18)$$

$$\left(\frac{\partial}{\partial \varphi^*} + \frac{1}{2} \frac{\partial S}{\partial \varphi^*} \right) \Psi = 0, \quad (3.19)$$

and we have $\Psi = e^{-S/2}$. Now, we find that the distribution P behaves as

$$P = \tilde{P} e^{-S/2} \propto e^{-S}, \quad (3.20)$$

at $\theta \rightarrow \infty$. The ensemble of $\varphi(\theta \rightarrow \infty)$, which is obtained by repeatedly solving the Langevin equation reproduces the one randomly generated by the Path integral measure e^{-S} , and thus the ensemble average of O over them reproduces the expectation value (1.1). Now, we find that when the action is real, to generate the ensemble by solving the Langevin equation is completely equivalent to generate it by the importance sampling method.

This is no longer true in the situation where the action is not real, that is, $S \neq S^\dagger$, and the Monte Carlo simulation suffers from the sign problem. Even in such a case, we can still

solve the Langevin equation and obtain the ensemble of the equilibrium solutions $\varphi(\theta \rightarrow \infty)$. Since H is not positive semi-definite if $S \neq S^\dagger$, it is not obvious whether there exists a unique equilibrium distribution in Eq. (3.15) in any kind of field theories. Even though, at least, if the real part of all eigenvalues of H is semi-positive, the above argument still holds and thus the ensemble average over $\varphi(\theta \rightarrow \infty)$ gives the expectation value (1.1). Therefore, there is a possibility that by using the Langevin method, we can attack the problem which cannot be handled by the Monte Carlo method.

We remark here that it is not easy to show whether the real part of all eigenvalues are positive or not. Moreover, even if we assume it, there still exist difficulties of slow convergence towards equilibrium solutions and of instability caused by the discretization of fictitious time [102, 103, 104, 105]. These difficulties originate from the complexification of P and hinder numerical simulations in practice. The condition to avoid such practical problems is still unclear and we need to check whether the method works well or not by performing numerical simulations. The practical criterion to judge the applicability of complex Langevin method is an still important open question [104, 105].

3.3 Complex Langevin equation

In this section, we summarize the basics to perform the complex Langevin simulation. As an example, let us consider the nonrelativistic $\lambda\varphi^4$ theory at finite chemical potential. The lattice-discretized action S_{lat} is

$$\begin{aligned} S_{\text{lat}} = & a^3 \sum_{\tau, \mathbf{x}} \left[\varphi_{\tau, \mathbf{x}}^* (\varphi_{\tau, \mathbf{x}} - e^{\mu a} \varphi_{\tau-a, \mathbf{x}}) \right. \\ & \left. - \frac{1}{2ma} \sum_i \left(\varphi_{\tau, \mathbf{x}+\hat{i}a}^* \varphi_{\tau, \mathbf{x}} + \varphi_{\tau, \mathbf{x}}^* \varphi_{\tau, \mathbf{x}+\hat{i}a} - 2|\varphi_{\tau, \mathbf{x}}|^2 \right) + \frac{1}{4} \frac{\lambda}{a^2} a^3 |\varphi_{\tau, \mathbf{x}}|^4 \right], \end{aligned} \quad (3.21)$$

or equivalently,

$$\begin{aligned} S_{\text{lat}} = & a^3 \sum_{\tau, \mathbf{x}} \left[-e^{\mu a} (\varphi_{\tau, \mathbf{x}}^a \varphi_{\tau-a, \mathbf{x}}^a + i\epsilon_{ab} \varphi_{\tau, \mathbf{x}}^a \varphi_{\tau-a, \mathbf{x}}^b) \right. \\ & \left. - \frac{1}{ma} \sum_i \varphi_{\tau, \mathbf{x}+\hat{i}a}^a \varphi_{\tau, \mathbf{x}}^a + \left(1 + \frac{3}{ma} \right) \varphi_{\tau, \mathbf{x}}^a \varphi_{\tau, \mathbf{x}}^a + \frac{1}{4} \frac{\lambda}{a^2} a^3 (\varphi_{\tau, \mathbf{x}}^a \varphi_{\tau, \mathbf{x}}^a)^2 \right], \end{aligned} \quad (3.22)$$

where $\varphi = \varphi^1 + i\varphi^2$ with $\varphi^{a=1,2}$ being real scalar fields. The Einstein convention is understood for repeated indices. ϵ_{ab} are completely antisymmetric tensor with $\epsilon_{12} = 1$. We impose the periodic boundary conditions to all directions. The chemical potential is introduced on the basis of the standard lattice techniques [90, 91, 106]: On the lattice, the covariant derivatives are replaced with the link variables and thus the chemical potential is introduced by the same manner as the abelian link variables. This point will be discussed in detail in the next chapter. We absorb the lattice spacing into the definition of the field and parameters, $a^{3/2}\phi \rightarrow \phi$,

$ma \rightarrow m$, $\mu a \rightarrow \mu$, and $\lambda/a^2 \rightarrow \lambda$. Then, in the following discussion, all dimensional quantities are scaled by the lattice spacing a .

It is clear from Eq. (3.22) that the lattice action is in general complex in the nonrelativistic boson regardless of zero or finite chemical potential, which causes the sign problem in the standard lattice simulations. In the Langevin method, we need to solve

$$\partial_\theta \varphi_{\tau,\mathbf{x}}^a(\theta) = -\frac{\partial S_{\text{lat}}}{\partial \varphi_{\tau,\mathbf{x}}^a} + \eta_{\tau,\mathbf{x}}^a(\theta), \quad (3.23)$$

where η^a are real Gaussian noises and satisfy

$$\langle \eta_x^a(\theta) \rangle = 0, \quad (3.24)$$

$$\langle \eta_x^a(\theta) \eta_y^b(\theta') \rangle = 2\delta_{ab} \delta_{xy} \delta(\theta - \theta'). \quad (3.25)$$

The complex lattice action makes the right hand side of Eq. (3.23) complex. Thus, we need to complexify the left hand side, namely, the two real fields φ^a as well. They are complexified as $\varphi^{aC} = \varphi^{aR} + i\varphi^{aI}$ and this is the reason why this method is called complex Langevin method. Then, Eq. (3.2) becomes complex stochastic differential equation for the two complex fields φ^{aC} in which the Gaussian noises are applied only to the real parts [87, 97, 98]. By discretizing the fictitious time θ as $\theta = \varepsilon n$ with ε being the auxiliary time step, we numerically solve the following equations:

$$\varphi_{\tau,\mathbf{x}}^{aR}(n+1) = \varphi_{\tau,\mathbf{x}}^{aR}(n) - \varepsilon \text{Re} \left[\frac{\partial S_{\text{lat}}}{\partial \varphi_{\tau,\mathbf{x}}^a} \right] + \sqrt{\varepsilon} \eta_{\tau,\mathbf{x}}^a(n), \quad (3.26)$$

$$\varphi_{\tau,\mathbf{x}}^{aI}(n+1) = \varphi_{\tau,\mathbf{x}}^{aI}(n) - \varepsilon \text{Im} \left[\frac{\partial S_{\text{lat}}}{\partial \varphi_{\tau,\mathbf{x}}^a} \right]. \quad (3.27)$$

The drift terms are given explicitly as

$$\begin{aligned} \text{Re} \left[\frac{\partial S_{\text{lat}}}{\partial \varphi_{\tau,\mathbf{x}}^a} \right] &= -e^\mu (\varphi_{\tau+1,\mathbf{x}}^{aR} + \varphi_{\tau-1,\mathbf{x}}^{aR}) - e^\mu \epsilon_{ab} (\varphi_{\tau+1,\mathbf{x}}^{bI} - \varphi_{\tau-1,\mathbf{x}}^{bI}) \\ &\quad - \frac{1}{m} \sum_i (\varphi_{\tau,\mathbf{x}+i}^{aR} + \varphi_{\tau,\mathbf{x}-i}^{aR}) + 2 \left(1 + \frac{3}{m} \right) \varphi_{\tau,\mathbf{x}}^{aR} \\ &\quad + \lambda (\varphi_{\tau,\mathbf{x}}^{bR} \varphi_{\tau,\mathbf{x}}^{bR} - \varphi_{\tau,\mathbf{x}}^{bI} \varphi_{\tau,\mathbf{x}}^{bI}) \varphi_{\tau,\mathbf{x}}^{aR} - 2\lambda \varphi_{\tau,\mathbf{x}}^{bR} \varphi_{\tau,\mathbf{x}}^{bI} \varphi_{\tau,\mathbf{x}}^{aI}, \end{aligned} \quad (3.28)$$

$$\begin{aligned} \text{Im} \left[\frac{\partial S_{\text{lat}}}{\partial \varphi_{\tau,\mathbf{x}}^a} \right] &= -e^\mu (\varphi_{\tau+1,\mathbf{x}}^{aI} + \varphi_{\tau-1,\mathbf{x}}^{aI}) + e^\mu \epsilon_{ab} (\varphi_{\tau+1,\mathbf{x}}^{bR} + \varphi_{\tau-1,\mathbf{x}}^{bR}) \\ &\quad - \frac{1}{m} \sum_i (\varphi_{\tau,\mathbf{x}+i}^{aI} + \varphi_{\tau,\mathbf{x}-i}^{aI}) + 2 \left(1 + \frac{3}{m} \right) \varphi_{\tau,\mathbf{x}}^{aI} \\ &\quad + \lambda (\varphi_{\tau,\mathbf{x}}^{bR} \varphi_{\tau,\mathbf{x}}^{bR} - \varphi_{\tau,\mathbf{x}}^{bI} \varphi_{\tau,\mathbf{x}}^{bI}) \varphi_{\tau,\mathbf{x}}^{aI} + 2\lambda \varphi_{\tau,\mathbf{x}}^{bR} \varphi_{\tau,\mathbf{x}}^{bI} \varphi_{\tau,\mathbf{x}}^{aR}. \end{aligned} \quad (3.29)$$

The expectation value is obtained by using the solution of Eqs. (3.26) and (3.27) as

$$\langle O \rangle = \lim_{n \rightarrow \infty} \langle O(\varphi^a = \varphi^{aC}(n)) \rangle_\eta, \quad (3.30)$$

where the operator is written in terms of the complex fields φ^{aC} . For example, the number density operator, $n_{\tau,\mathbf{x}} = \partial\mathcal{L}/\partial\mu$ with \mathcal{L} being the lattice Lagrangian density, is given by

$$\begin{aligned} n_{\tau,\mathbf{x}} &= e^\mu (\delta_{ab} + i\epsilon_{ab}) \varphi_{\tau,\mathbf{x}}^{aC} \varphi_{\tau-1,\mathbf{x}}^{bC} \\ &= e^\mu (\delta_{ab} + i\epsilon_{ab}) \left(\varphi_{\tau,\mathbf{x}}^{aR} \varphi_{\tau-1,\mathbf{x}}^{bR} - \varphi_{\tau,\mathbf{x}}^{aI} \varphi_{\tau-1,\mathbf{x}}^{bI} + i (\varphi_{\tau,\mathbf{x}}^{aR} \varphi_{\tau-1,\mathbf{x}}^{bI} + \varphi_{\tau,\mathbf{x}}^{aI} \varphi_{\tau-1,\mathbf{x}}^{bR}) \right). \end{aligned} \quad (3.31)$$

We note that all observables are complexified in the same manner and have both real and imaginary parts. Of course, the imaginary parts should be zero after the ensemble average.

In the following numerical simulation, we adopt a higher order algorithm [107] to improve the step size dependence [108], which is summarized in Appendix A. Moreover, instead of repeatedly solving the Langevin equation, by assuming the ergodicity of stochastic evolution, we calculate observables as the long time average over the Langevin trajectories. More specifically, the ensemble φ^{aC} is taken from every step after updating the Langevin processes N_{step} times (the Langevin time interval $\Delta\theta = \varepsilon N_{\text{step}}$), where we discard the early-stage of Langevin evolution before reaching equilibrium solutions. Then, the expectation value is given as

$$\langle \hat{O} \rangle = \frac{1}{N_{\text{stat}}} \sum_{\varphi^{aC}} O(\varphi^{aC}), \quad (3.32)$$

with N_{stat} being the total number of field configurations taken from the Langevin trajectories. Statistical errors are estimated by using the standard jackknife method, which is summarized in Appendix B.

3.4 Numerical simulation

As an example, we perform the complex Langevin simulation of the lattice action (3.21). We have numerically solved Eqs. (3.26) and (3.27) by adopting the higher order algorithm [107, 108] with $\varepsilon = 5.0 \times 10^{-4} a$. The total number of lattice sites is $V = N_x N_y N_z N_\tau = 6^4, 8^4, \text{ and } 10^4$. The periodic boundary condition was imposed to all directions. We set $ma = 1.0$ and $\lambda/a^2 = 1.0$. We have updated the Langevin evolution 1.5×10^6 times after discarding the equilibration stage to obtain the data shown below. Errors were estimated by using the jackknife method. We show the early stage of the Langevin evolution towards the equilibration in Fig. 3.1, where we show the number density

$$n = \frac{1}{V} \sum_{\tau,\mathbf{x}} n_{\tau,\mathbf{x}}, \quad (3.33)$$

obtained from each Langevin step in the case of $N^4 = 10^4$ and $\mu a = 0.5$. We can clearly see that the number density reaches the equilibrium value after 2.5×10^4 times updated. The ensemble used below is taken from the Langevin steps after 5.0×10^4 times updated.

Now, we will show the numerical result. First, we show the number density (3.33) as a function of chemical potential for the lattice size $V = 6^4$ (circle), 8^4 (triangle), and 10^4

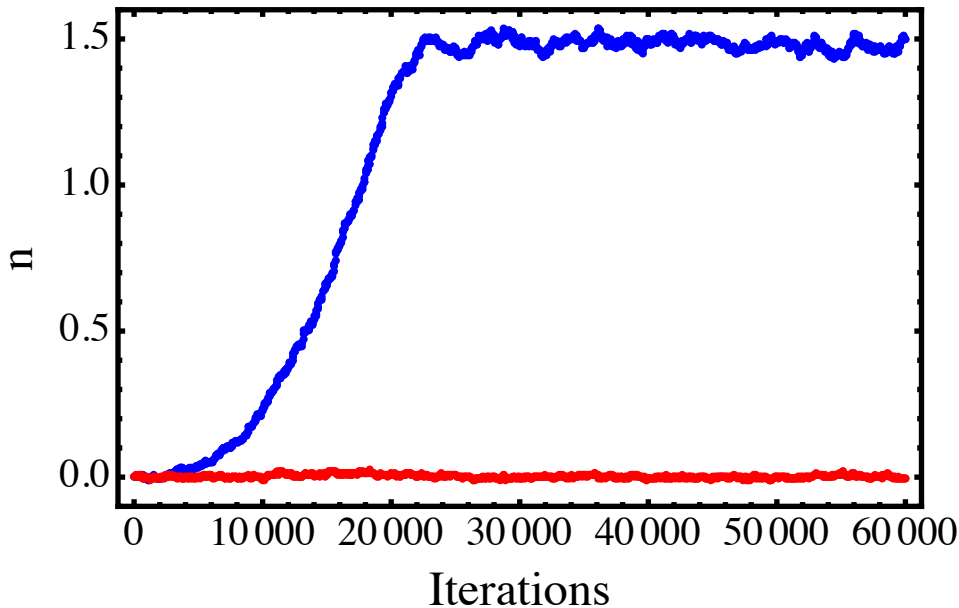


Figure 3.1: Number density n as a function of the Langevin time evolution in the case of $N^4 = 10^4$, and $\mu a = 0.5$. Blue and red open curves denote real and imaginary parts of number density, respectively.

(diamond) in Fig. 3.2. We can clearly see a transition from zero density phase to finite density phase. We note that non-linear behavior above $\mu a \sim 0.8$ would be a lattice artifact, which comes from exponentiating the chemical potential as in Eq. (3.21) or (3.31). The chemical potential should be small enough, so that the exponential term can be expanded, that is, $e^{\mu a} \sim 1 + \mu a$ is numerically satisfied. We show the number density near the transition region in Fig. 3.3. Imaginary part of the number density was consistent with zero within error bars in both figures.

At strictly zero temperature and in the thermodynamic limit, all physical observables are independent of chemical potential until the lowest lying mode is excited by the chemical potential. Therefore, even though it is manifestly introduced in the density matrix as $\exp(-\beta(H - \mu N))$, the μ -dependence should be exactly canceled over the ensemble average below the critical value of μ , and this exact cancelation is referred to as the Silver Blaze problem [101]. In Fig. 3.3, with increasing the lattice volume $V = N^4$, the transition becomes sharper and sharper and the density goes to zero below the critical value $\mu_c a \sim 0.20$, so that the Silver Blaze problem can be correctly handled in our simulation.

At zero temperature, as shown in Chap. 2, the nonvanishing number density means the macroscopic occupation of the lowest quantum state, which is comparable to the spatial volume of the system and thus the Bose-Einstein condensation may occur above the critical chemical potential. To show this, we have calculated the two-point correlation function $G(\mathbf{x} - \mathbf{y}) = \langle \phi^*(\tau, \mathbf{x}) \phi(\tau, \mathbf{y}) \rangle$ and checked the long range order. We show the two-point correlation function

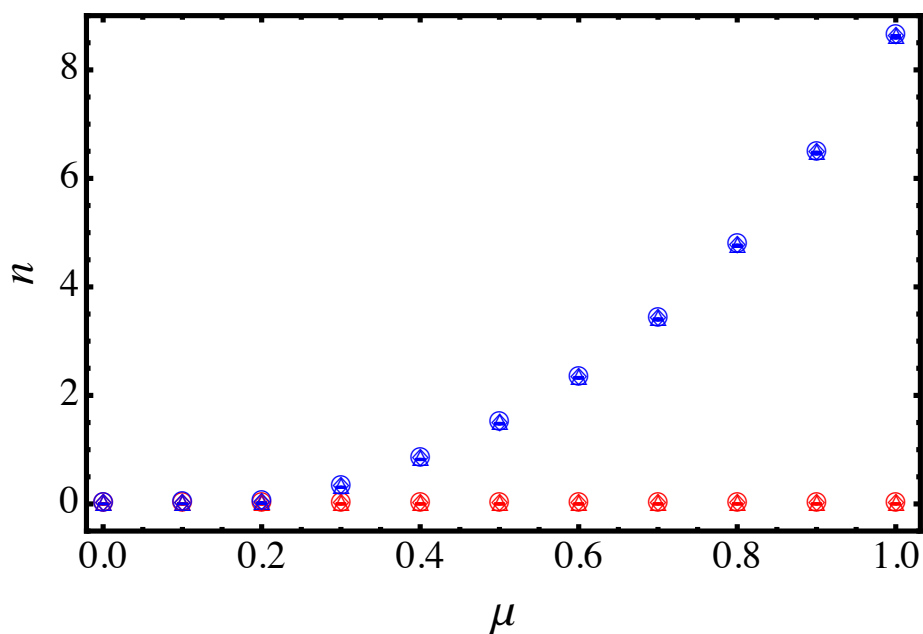


Figure 3.2: Number density n as a function of chemical potential μ at $N = 6$ (circle), 8 (triangle) and 10 (diamond). Blue and red symbols denote real and imaginary parts of number density. All the scales are measured in the unit of the lattice spacing a .

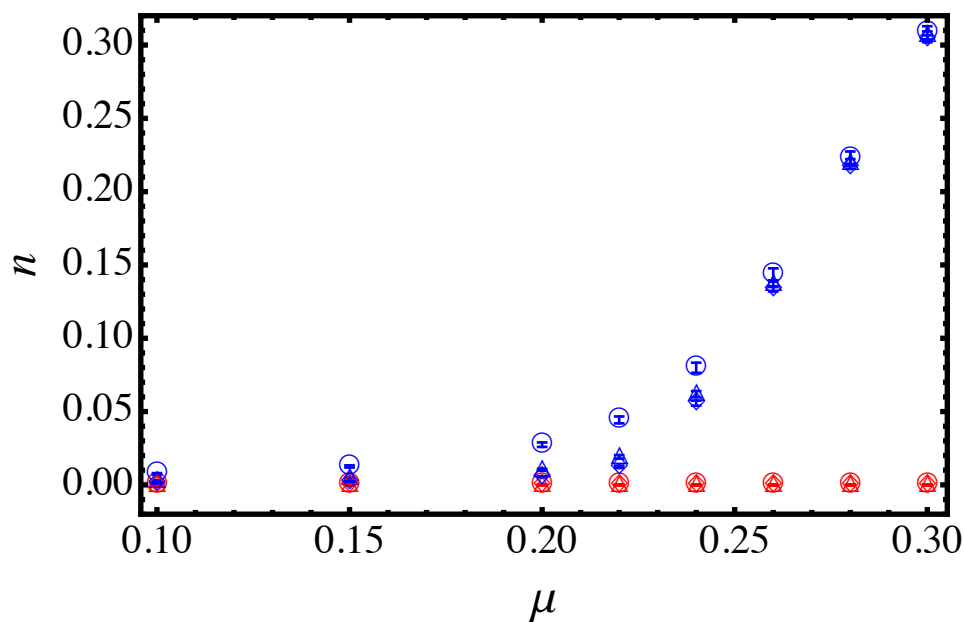


Figure 3.3: Number density n near the transition region at $N = 6$ (circle), 8 (triangle) and 10 (diamond). Blue and red symbols denote real and imaginary parts of number density. All the scales are measured in the unit of the lattice spacing a .

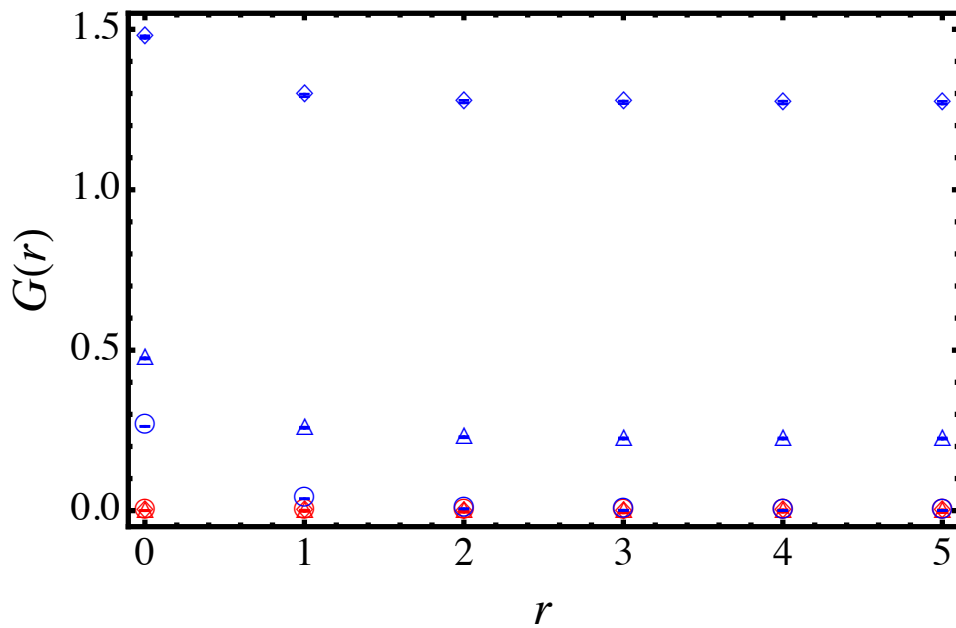


Figure 3.4: Boson propagator $G(r)$ as a function of r at $\mu a = 0.1$ (circle), 0.3 (triangle) and 0.6 (diamond). Blue and red symbols denote real and imaginary parts of propagator. All the scales are measured in the unit of the lattice spacing a .

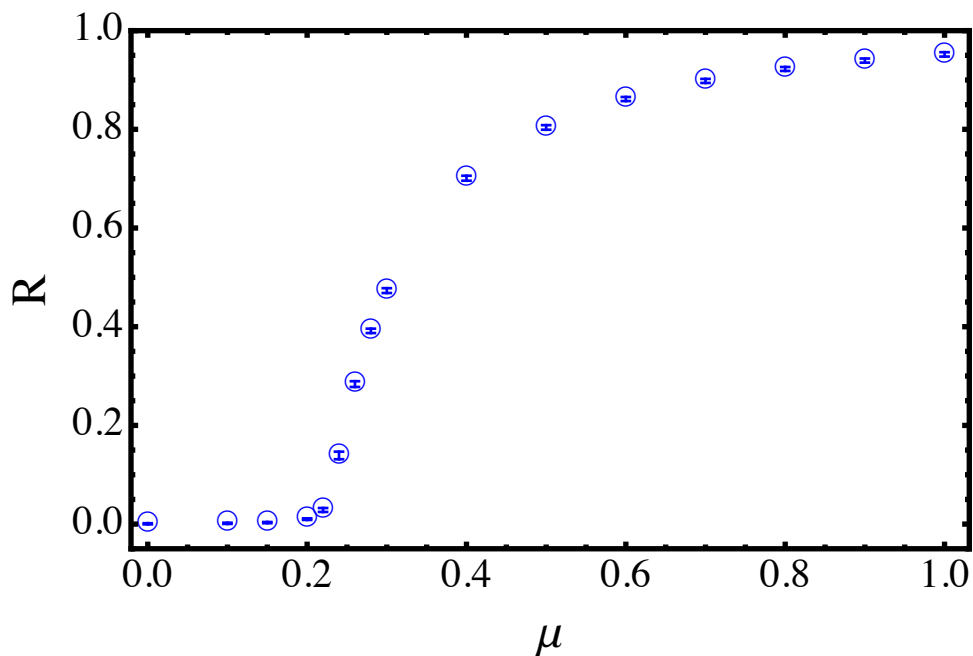


Figure 3.5: Condensate fraction R as a function of the chemical potential μ . The chemical potential μ is measured in the unit of the lattice spacing a .

as a function of r :

$$G(r) = \frac{1}{N_\tau N_x N_y} \sum_{\tau, x, y} \langle \phi^*(\tau, x, y, r) \phi(\tau, x, y, 0) \rangle, \quad (3.34)$$

at $\mu a = 0.1$ (circle), 0.3 (triangle) and 0.5 (diamond) in Fig. 3.4. The lattice size was fixed with $N^4 = 10^4$. Below the critical value of the chemical potential (circle), the boson propagator exponentially drops to zero. On the other hand, above the critical chemical potential (triangle and diamond), it goes to a constant value and thus the signature of long range order has been clearly observed. We show the condensate fraction R as a function of chemical potential in Fig. 3.5, which is defined as

$$R = \text{Re}[G(N_z a/2)] / \text{Re}[G(0)], \quad (3.35)$$

where N_z is an extent along the z direction ($N_z = 10$ in our simulation). From Fig. 3.5, we find that the superfluid transition occurs simultaneously at the critical value of the Silver Blaze problem μ_c , and thus μ_c can also be interpreted as the critical value of the spontaneous U(1) symmetry breaking.

Chapter 4

Nonrelativistic Bose-Einstein condensate

In this chapter, we present our original work [71]. We perform ab-initio simulations of the nonrelativistic Bose-Einstein condensate under strong external fields such as the electric field, the magnetic field, and the rotation. All the lattice actions discussed in this chapter are complex, so that the conventional Monte Carlo method suffers from the sign problem. To overcome this difficulty, we adopt the complex Langevin method, which can take into account quantum fluctuations exactly even for such complex actions.

First, in Sec. 4.1, we discuss how to apply such external fields on the lattice. This is the review part based on Refs. [90, 91, 92, 106]. On the lattice, the naive discretization does not maintain the local $U(1)$ symmetry. Thus, we improve the lattice action by adding higher order terms in terms of the lattice spacing, so as the lattice action to have the lattice version of the local $U(1)$ symmetry.

Then, in Sec. 4.2, we analyze the Bose-Einstein condensate in the presence of electric fields: In Euclid simulation, two types of electric fields are possible, that is, the Euclid and Minkowski electric fields (See e.g., Ref. [109]). In our work, we apply the Minkowski electric field, so that we can directly calculate observables without performing the analytic continuation. We show that the non-uniform charge distribution is generated according to the vector potential. We also analyze the associated $U(1)$ symmetry breaking by performing the long-range order analysis.

Next, in Sec. 4.3, we analyze the Bose-Einstein condensate in the presence of magnetic field. As explicitly shown in the free theory in Sec. 4.3.1, the Bose-Einstein condensate is destroyed by the magnetic field due to the formation of Landau levels. The derivation is based on Refs. [110, 111]. We numerically show that it occurs even in the interacting theory. The Bose-Einstein condensate becomes inhomogeneous, where the quantum vortex is generated. We show that the vortex is quantized far from the critical chemical potential, but it is blurred by quantum fluctuation as the chemical potential is getting close to its critical value.

Finally, in Sec. 4.4, we analyze the rotating Bose-Einstein condensate. We formulate the rotating lattice through the effective magnetic field induced in the rotating frame in Ref. [71].

The direct evidence of the quantum vortex nucleation is the quantized circulation. In our simulation, the quantization of the average circulation is clearly seen, and at the same time the quantum fluctuation of vortex number is also seen. At first glance, these two facts seem contradicting or counterintuitive. However, we show that the fluctuation behaves as Gaussian and, as a result of cancellation, the average circulation becomes integer.

4.1 Electromagnetic fields on the lattice

In this section, we discuss how to apply external electromagnetic fields on the lattice. Let us start with the local U(1) symmetry in the Minkowski space in continuum theories. The action of charged boson is

$$iS_{\text{con}} = i \int dt d^3x \left[\varphi^* i D_t \varphi - \frac{1}{2m} |D_i \varphi|^2 - \frac{1}{4} \lambda |\varphi|^4 \right], \quad (4.1)$$

where $D_{\mu=t,\mathbf{x}} = \partial_\mu - iqA_\mu^M$. This action is invariant under the local U(1) transformation:

$$\varphi \rightarrow e^{i\theta} \varphi, \quad (4.2)$$

$$qA_\mu^M \rightarrow qA_\mu^M - \partial_\mu \theta. \quad (4.3)$$

The analytic continuation of gauge fields is given as

$$A_t^M \rightarrow iA_\tau^E, \quad (4.4)$$

$$A_{i=x,y,z}^M \rightarrow A_i^E, \quad (4.5)$$

with $t \rightarrow -i\tau$, and then the Euclid action is

$$-S_{\text{con}} = - \int d\tau d^3x \left[\varphi^* D_\tau \varphi + \frac{1}{2m} |D_i \varphi|^2 + \frac{1}{4} \lambda |\varphi|^4 \right], \quad (4.6)$$

where $D_{\mu=\tau,\mathbf{x}} = \partial_\mu - iqA_\mu^E$. Here and below, the Minkowski and Euclid gauge field are, respectively, denoted as A_μ^M and A_μ^E . The Euclid action is invariant under Eqs. (4.2) and (4.3) with replacing A_μ^M by A_μ^E . We discretize the Euclid action (4.6) on the hypercubic lattice. In the discretized action, the derivatives are replaced by finite differences,

$$\partial_\tau \varphi_{\tau,\mathbf{x}} \rightarrow (\varphi_{\tau,\mathbf{x}} - \varphi_{\tau-a,\mathbf{x}}) / a, \quad (4.7)$$

$$\partial_i \varphi_{\tau,\mathbf{x}} \rightarrow (\varphi_{\tau,\mathbf{x}} - \varphi_{\tau,\mathbf{x}-\hat{i}a}) / a. \quad (4.8)$$

Then, the lattice action reads

$$S_{\text{lattice}} = a^4 \sum_{\tau,\mathbf{x}} \left[\frac{1}{a} \varphi_{\tau,\mathbf{x}}^* (\varphi_{\tau,\mathbf{x}} - \varphi_{\tau-a,\mathbf{x}} - iqaA_\tau^E \varphi_{\tau,\mathbf{x}}) \right. \\ \left. + \frac{1}{2ma^2} \sum_i \left(\varphi_{\tau,\mathbf{x}}^* - \varphi_{\tau,\mathbf{x}-\hat{i}a}^* + iqaA_i^E \varphi_{\tau,\mathbf{x}}^* \right) (\varphi_{\tau,\mathbf{x}} - \varphi_{\tau,\mathbf{x}-\hat{i}a} - iqaA_i^E \varphi_{\tau,\mathbf{x}}) + \frac{1}{4} \lambda |\varphi|^4 \right]. \quad (4.9)$$

The problem is that this lattice action is not invariant under the lattice version of U(1) gauge transformation,

$$\varphi \rightarrow e^{i\theta} \varphi, \quad (4.10)$$

$$qA_\tau^E \rightarrow eA_\tau^E - (\theta_{\tau,x} - \theta_{\tau-a,x})/a, \quad (4.11)$$

$$qA_i^E \rightarrow eA_i^E - (\theta_{\tau,x} - \theta_{\tau,x-\hat{i}a})/a. \quad (4.12)$$

Therefore, even if we replace A_μ^E by external fields, they cannot induce proper Noether currents on the lattice. To obtain the U(1) symmetric lattice action, we need to cancel the phase shift of φ by the local shift of A_μ^E . For this purpose, we improve the lattice action as

$$\begin{aligned} S_{\text{lattice}} = & a^4 \sum_{\tau,\mathbf{x}} \left[\frac{1}{a} \varphi_{\tau,\mathbf{x}}^* \left(\varphi_{\tau,\mathbf{x}} - e^{-ieaA_\tau^E} \varphi_{\tau-a,\mathbf{x}} \right) \right. \\ & \left. + \frac{1}{2ma^2} \sum_i \left(\varphi_{\tau,\mathbf{x}}^* - e^{-iqaA_i^E} \varphi_{\tau,\mathbf{x}-\hat{i}a}^* \right) \left(\varphi_{\tau,\mathbf{x}} - e^{iqaA_i^E} \varphi_{\tau,\mathbf{x}-\hat{i}a} \right) + \frac{1}{4} \lambda |\varphi|^4 \right]. \end{aligned} \quad (4.13)$$

By imposing the periodic boundary conditions, we have [92]

$$\begin{aligned} S_{\text{lattice}} = & a^4 \sum_{\tau,\mathbf{x}} \left[\frac{1}{a} \varphi_{\tau,\mathbf{x}}^* \left(\varphi_{\tau,\mathbf{x}} - e^{-iqaA_\tau^E} \varphi_{\tau-a,\mathbf{x}} \right) \right. \\ & \left. + \frac{1}{2ma^2} \sum_i \left(2\varphi_{\tau,\mathbf{x}}^* \varphi_{\tau,\mathbf{x}} - \varphi_{\tau,\mathbf{x}-\hat{i}a}^* e^{-iqaA_i^E} \varphi_{\tau,\mathbf{x}} - \varphi_{\tau,\mathbf{x}}^* e^{iqaA_i^E} \varphi_{\tau,\mathbf{x}-\hat{i}a} \right) + \frac{1}{4} \lambda |\varphi|^4 \right], \end{aligned} \quad (4.14)$$

or equivalently,

$$\begin{aligned} S_{\text{lattice}} = & a^4 \sum_{\tau,\mathbf{x}} \left[\frac{1}{a} \varphi_{\tau,\mathbf{x}}^* \left(\varphi_{\tau,\mathbf{x}} - u_\tau \varphi_{\tau-a,\mathbf{x}} \right) \right. \\ & \left. + \frac{1}{2ma^2} \sum_i \left(2\varphi_{\tau,\mathbf{x}}^* \varphi_{\tau,\mathbf{x}} - \varphi_{\tau,\mathbf{x}}^* u_i \varphi_{\tau,\mathbf{x}+\hat{i}a} - \varphi_{\tau,\mathbf{x}+\hat{i}a}^* u_i^\dagger \varphi_{\tau,\mathbf{x}} \right) + \frac{1}{4} \lambda |\varphi|^4 \right], \end{aligned} \quad (4.15)$$

where $u_{\mu=\tau,\mathbf{x}} = \exp(-iaqA_\mu^E(x))$. The improved lattice action (4.15) is apparently invariant under Eqs. (4.10), (4.11) and (4.12). In Eq. (4.13) and (4.14), the covariant derivatives are discretized as

$$\begin{aligned} (\partial_0 - iqA_\tau^E) \varphi_{\tau,\mathbf{x}} & \rightarrow (\varphi_{\tau,\mathbf{x}} - \varphi_{\tau-a,\mathbf{x}} - iqaA_\tau^E \varphi_{\tau,\mathbf{x}}) / a \\ & \rightarrow (\varphi_{\tau,\mathbf{x}} - \varphi_{\tau-a,\mathbf{x}} - iqaA_\tau^E \varphi_{\tau-a,\mathbf{x}} + \mathcal{O}(a^2)) / a \\ & \rightarrow (\varphi_{\tau,\mathbf{x}} - e^{iqaA_\tau^E} \varphi_{\tau-a,\mathbf{x}} + \mathcal{O}(a^2)) / a, \end{aligned} \quad (4.16)$$

$$\begin{aligned} (\partial_i - iqA_i^E) \varphi_{\tau,\mathbf{x}} & \rightarrow (\varphi_{\tau,\mathbf{x}} - \varphi_{\tau,\mathbf{x}-\hat{i}a} - iqaA_i^E \varphi_{\tau,\mathbf{x}}) / a \\ & \rightarrow (\varphi_{\tau,\mathbf{x}} - e^{iqaA_i^E} \varphi_{\tau,\mathbf{x}-\hat{i}a} + \mathcal{O}(a^2)) / a. \end{aligned} \quad (4.17)$$

In the action (4.15), we recover the U(1) symmetry by adding higher order terms with respect to the lattice spacing a , and thus the lattice actions (4.9) and (4.15) are equivalent to each other in the limit of $a \rightarrow 0$.

In summary, in lattice simulations, external U(1) fields can be introduced as abelian phase factors, which respect the local U(1) symmetry on the lattice. We remark here that the chemical potential can be applied as the constant A_τ^E . Also, the lattice simulation in co-moving frame can be performed by introducing a constant A_i^E .

4.2 Electric field

4.2.1 Minkowski and Euclid electric fields

In this section, we discuss external electric fields in Euclid simulations. The magnetic field does not change its sign in the analytic continuation between the Minkowski and Euclid theory, but the electric field does. Therefore, two types of external electric fields are possible in lattice simulations, that is, the Minkowski electric field E^M and the Euclid electric field E^E . These two are related to each other by the analytic continuation $E^M \rightarrow iE^E$. For Euclid electric field, it can be introduced as

$$S_{\text{con}} = \int d\tau d^3x \left[\varphi^* D_\tau \varphi + \frac{1}{2m} |\partial_i \varphi|^2 + \frac{1}{4} \lambda |\varphi|^4 \right], \quad (4.18)$$

by using the Euclid gauge field A_τ^E , where we take the spatial components of gauge fields zero, i.e., $A_i^E = 0$. The Euclid electric field is given as $E_i^E = -\partial_i A_\tau^E$. The Euclid gauge field can induce only the imaginary shift of particle energy ε as

$$\varepsilon \rightarrow \varepsilon - iqA_\tau^E, \quad (4.19)$$

not the real energy shift. Therefore, the Euclid electric field does not cause neither the instability of the vacuum nor particle creations. This is the same as the case of imaginary chemical potential. Also, since the real physics is given by the Minkowski electric field, the analytic continuation of electric field is needed to obtain the physical result, when we use the Euclid electric field.

On the other hand, the Minkowski electric field can be introduced by the replacement $A_\tau^E \rightarrow -iA_\tau^M$ in the same action (4.18). We take the spatial components of gauge fields zero again, so that the Minkowski electric field is given as $E_i^M = -\partial_i A_\tau^M$. Now, the Minkowski electric field induces the real energy shift as

$$\varepsilon \rightarrow \varepsilon - qA_\tau^M, \quad (4.20)$$

and causes the vacuum instability. In relativistic theories, particle creations can occur above the critical electric field via the so called Schwinger mechanism [112]. The external Minkowski electric field can be introduced in the Euclidian simulations, however, causes the sign problem. Thus, it is in general hard to apply the Minkowski electric field in lattice simulations. The situation is exactly the same as the case of real chemical potential.

4.2.2 Numerical simulation

In Euclid simulations, the real-time dynamics induced by the electric field cannot be followed. What we can calculate is the expectation value in equilibrium state, which minimizes the free energy in the presence of the electric field. The equilibrium state is realized when the charged particles distribute according to the electric potential. In other words, particles concentrate on the highest voltage region. Also, there is no finite (dissipative) current in the equilibrium state.

At zero electric field, the equilibrium state favours the uniform condensation due to the bose statics, namely, the macroscopic occupation of zero momentum state is realized. On the other hand, non-uniform charge distribution is favored at finite electric field, which makes the condensation non-uniform. There must be crossover between these uniform and non-uniform Bose-Einstein condensate.

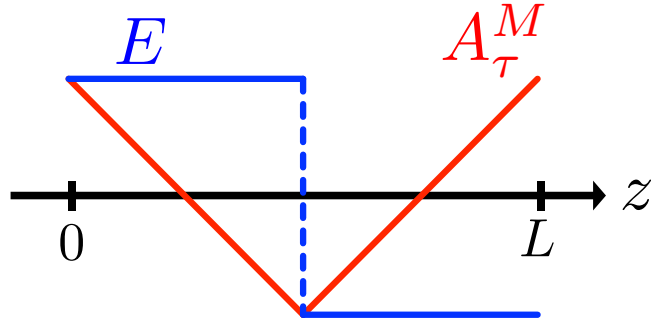


Figure 4.1: Schematic configuration of vector potential A_τ^M and associated electric field E^M . The periodic boundary condition is imposed along the z direction.

To show this crossover, we have applied the Minkowski electric field to the interacting charged bose gas. Below, we consider only the Minkowski electric field and omit the upper script M . The lattice action is

$$S_{\text{lat}} = a^3 \sum_x \left[\varphi_{\tau, \mathbf{x}}^* (\varphi_{\tau, \mathbf{x}} - u_\tau \varphi_{\tau - a, \mathbf{x}}) - \frac{1}{2ma} \sum_i \left(\varphi_{\tau, \mathbf{x} + \hat{i}a}^* \varphi_{\tau, \mathbf{x}} + \varphi_{\tau, \mathbf{x}}^* \varphi_{\tau, \mathbf{x} + \hat{i}a} - 2|\varphi_{\tau, \mathbf{x}}|^2 \right) + \frac{1}{4} \frac{\lambda}{a^2} a^3 |\varphi_{\tau, \mathbf{x}}|^4 \right], \quad (4.21)$$

where $u_\tau(x) = \exp(-qaA_\tau(x))$ is the real (not complex) link variable. The lattice volume is $N_x N_y N_z \times N_\tau$. We take all spatial components of gauge potentials zero, i.e., $A_i = 0$. We also impose periodic boundary conditions to all directions. The gauge potential and the associated electric field are shown in Fig. 4.1. We consider the electric field along z direction. To satisfy the periodic boundary condition, we set the vector potential as

$$A_\tau(z) = \begin{cases} -E(z - L/4) & (0 \leq z < L/2) \\ E(z - 3L/4) & (L/2 \leq z < L), \end{cases} \quad (4.22)$$

where $L = N_z a$, and we divided finite lattice into two regions. The electric field in each region is given as

$$E_z = -\partial_z A_\tau(z) = \begin{cases} +E & (0 \leq z < L/2) \\ -E & (L/2 \leq z < L). \end{cases} \quad (4.23)$$

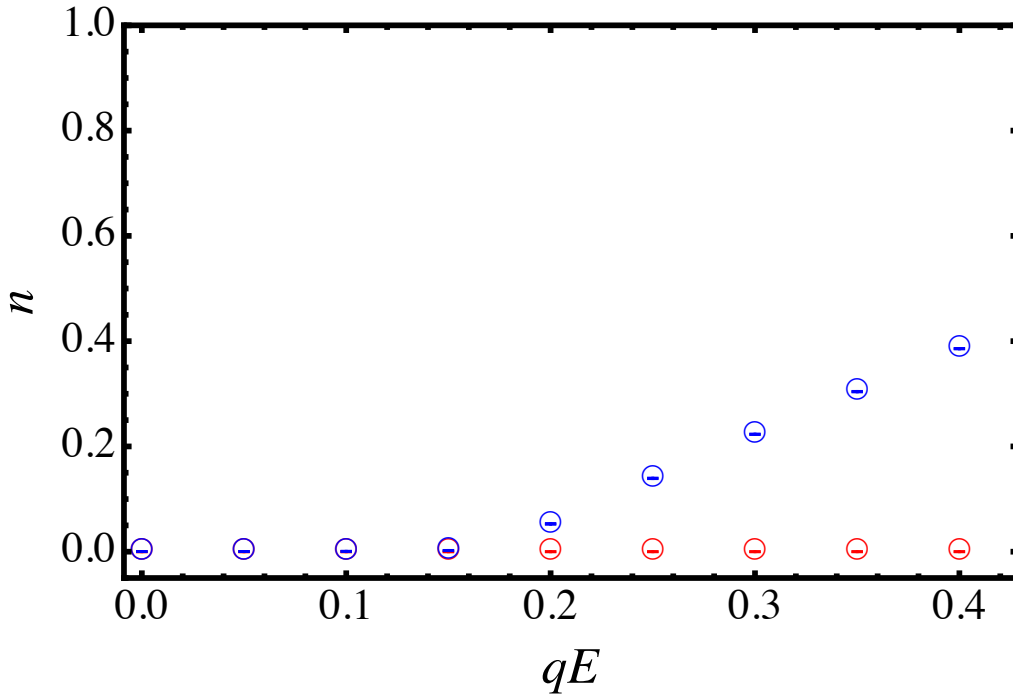


Figure 4.2: Number density n as a function of electric field $a^2 qE$. Blue and red symbols denote real and imaginary parts of number density, respectively. All the scales are measured in the unit of the lattice spacing a .

We analyze the spontaneous U(1) symmetry breaking by the electric field. We have numerically calculated Eqs. (3.26) and (3.27) with the lattice action (4.21), by adopting the higher order algorithm [107, 108] with $\varepsilon = 2.0 \times 10^{-4} a$. The total number of lattice sites is $V = N_x N_y N_z N_\tau = 10^4$. The periodic boundary condition was imposed to all directions. We set $ma = 1.0$ and $\lambda/a^2 = 1.0$. Errors were estimated by using the jackknife method. We note that imaginary parts of observables were found to be consistent with zero within error bars.

We show the charge density

$$n = \frac{1}{V} \sum_{\tau, \mathbf{x}} n_{\tau, \mathbf{x}}, \quad (4.24)$$

$$n_{\tau, \mathbf{x}} = (\delta_{ab} + i\epsilon_{ab}) \left(\varphi_{\tau, \mathbf{x}}^{aR} \varphi_{\tau-1, \mathbf{x}}^{bR} - \varphi_{\tau, \mathbf{x}}^{aI} \varphi_{\tau-1, \mathbf{x}}^{bI} + i \left(\varphi_{\tau, \mathbf{x}}^{aR} \varphi_{\tau-1, \mathbf{x}}^{bI} + \varphi_{\tau, \mathbf{x}}^{aI} \varphi_{\tau-1, \mathbf{x}}^{bR} \right) \right), \quad (4.25)$$

as a function of the electric field in Fig 4.2. Below the critical value of electric field, the charge density is completely independent of E as in the case of chemical potential. Above the critical value, the charge density shows the linear dependence, which is also consistent with that in the

case of chemical potential shown in Fig. 3.3. To see the difference between the electric field and the chemical potential, we show the charge density distribution along the parallel direction to the electric field in Fig. 4.3:

$$n(z) = \frac{1}{N_\tau N_x N_y} \sum_{\tau, x, y} n_{\tau, \mathbf{x}}. \quad (4.26)$$

Above the critical electric field, we can clearly see that the particles accumulate in the highest

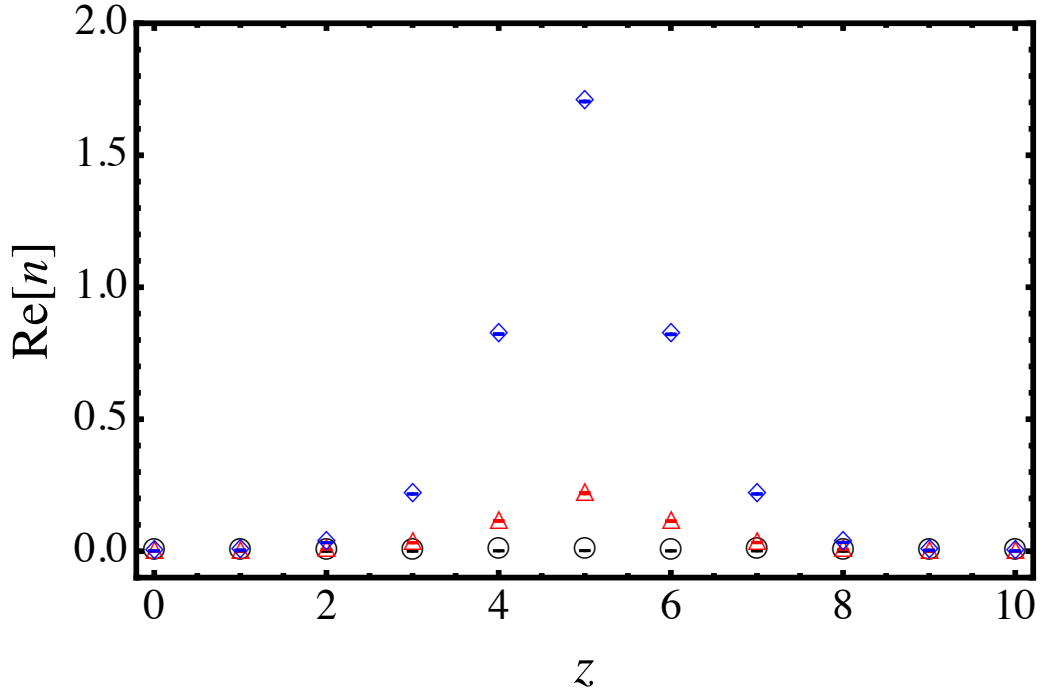


Figure 4.3: Number density n as a function of z at $a^2qE = 0.1$ (circle), 0.2 (triangle) and 0.4 (diamond). All the scales are measured in the unit of the lattice spacing a .

voltage region shown in Fig. 4.1, as expected. The charge density becomes zero in the region, where $-qA_\tau^M$ is smaller than the critical chemical potential. It shows the linear z dependence in the region, where $-qA_\tau^M$ is larger than the critical chemical potential. This behavior is completely consistent with the configuration of the vector potential shown in Fig. 4.1.

As discussed in Sec. 3, the nonvanishing number density is accompanied by the spontaneous U(1) symmetry breaking at zero (or sufficiently low) temperature. To see non-uniform U(1) symmetry breaking induced by the non-uniform charge distribution, we have performed the off-diagonal long-range order analysis. We have calculated the two-point correlation function in the plane perpendicular to the electric field:

$$G(r, z) = \frac{1}{N_\tau N_y} \sum_{\tau, y} \langle \phi^*(\tau, r, y, z) \phi(\tau, 0, y, z) \rangle. \quad (4.27)$$

In Fig. 4.4, we show the two-point correlation function in the perpendicular plane at $z = 5$ in

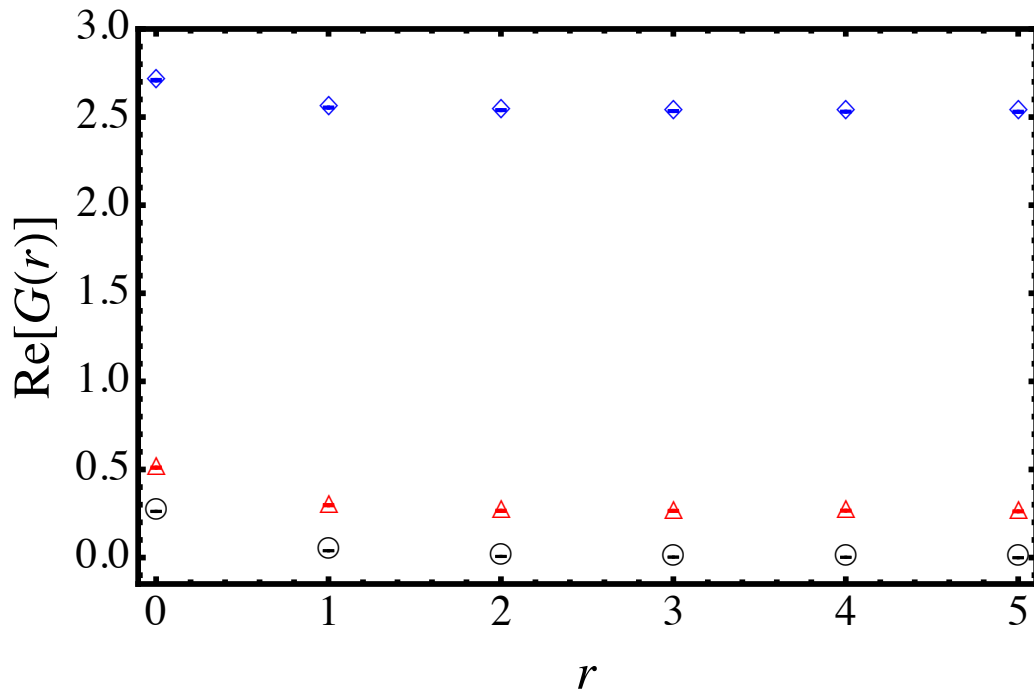


Figure 4.4: Boson propagator $G(r)$ as a function of r at $z = 5$, and $a^2qE = 0.1$ (circle), 0.2 (triangle) and 0.4 (diamond). All the scales are measured in the unit of the lattice spacing a .

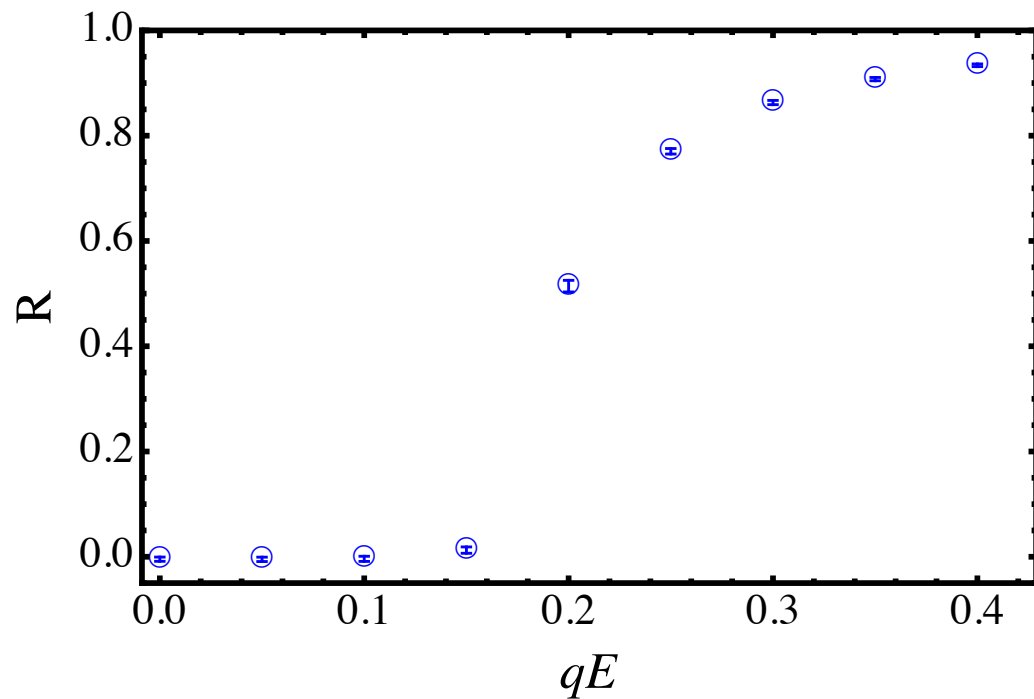


Figure 4.5: Condensate fraction R at $z = 5$ as a function of a^2qE . All the scales are measured in the unit of the lattice spacing a .

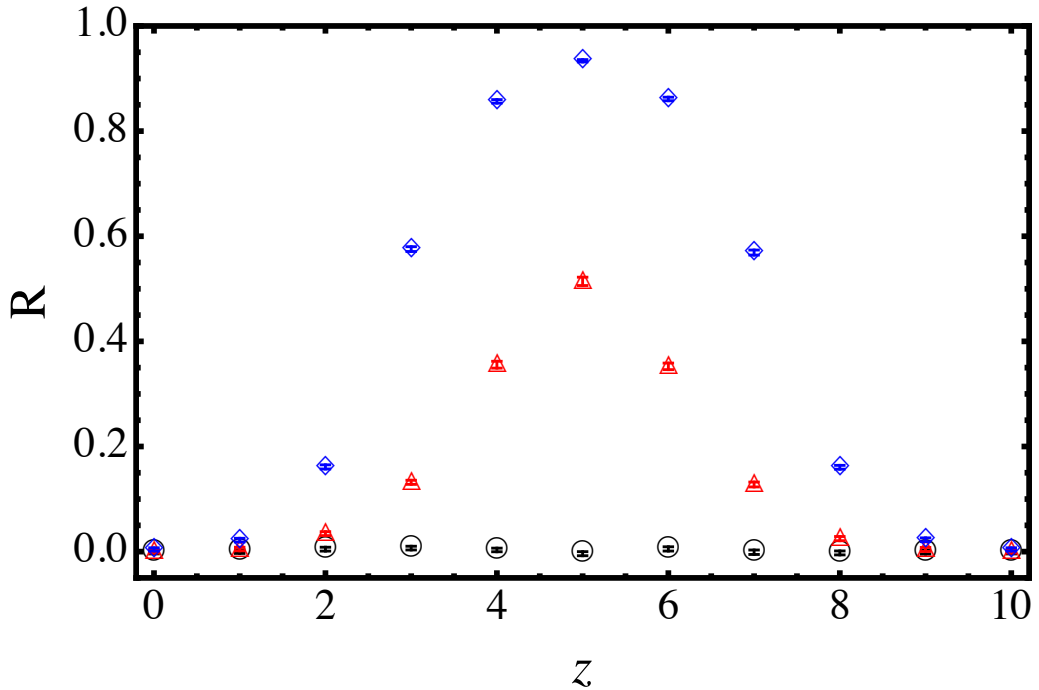


Figure 4.6: Condensate fraction R as a function of z at $a^2qE = 0.1$ (circle), 0.2 (triangle) and 0.4 (diamond). All the scales are measured in the unit of the lattice spacing a .

the case of $a^2qE = 0.1$ (circle), 0.2 (triangle) and 0.5 (diamond). The signature of long-range order is clearly observed above the critical electric field (triangle and diamond). We have also calculated the condensate fraction R :

$$R(z) = \text{Re}[G(N_x a/2, z)] / \text{Re}[G(0, z)], \quad (4.28)$$

where N_x is an extent along the x direction ($N_x = 10$ in our simulation). We show the condensate fraction as a function of the electric field at the highest voltage point ($z = 5a$) in Fig. 4.5. We can see the transition from the U(1) symmetric to the U(1) broken phase at $a^2qE \sim 0.15$. To see the inhomogeneity of symmetry breaking, we show the condensate fraction as a function of z at $a^2qE = 0.1$ (circle), 0.2 (triangle) and 0.4 (diamond) in Fig. 4.6. Reflecting the inhomogeneity of the charge density, the condensate fraction becomes also inhomogeneous.

4.3 Magnetic field

4.3.1 Landau level

We start with the free charged scalar field Φ in a uniform magnetic field A_μ . The equation of motion reads

$$\left(iD_0 - \frac{1}{2m} D_i^2 \right) \Phi(x) = 0, \quad (4.29)$$

with the background covariant derivative $D_\mu = \partial_\mu - ieA_\mu^M$. We choose the symmetric gauge $A_\mu^M = (0, By/2, -Bx/2, 0)$, and rewrite Eq. (4.29) with an ansatz $\Phi(x) = f(x_\parallel)\varphi(x_\perp)$ as

$$\left(i\partial_0 - \frac{1}{2m}\partial_z^2\right) f(x_\parallel) = -\lambda f(x_\parallel), \quad (4.30)$$

$$-\frac{1}{2m}((D_1)^2 + (D_2)^2)\varphi(x_\perp) = \lambda\varphi(x_\perp). \quad (4.31)$$

We use the convention of $x_\parallel = (x^0, x^3) = (t, z)$ and $x_\perp = (x^1, x^2) = (x, y)$. From Eq. (4.30), we have

$$f(x_\parallel) = \exp(-i\varepsilon t + ip^3 z), \quad (4.32)$$

$$\lambda = \varepsilon - \frac{(p^3)^2}{2m}. \quad (4.33)$$

Also, we can solve Eq. (4.31) by rewriting it in the Dirac bracket form,

$$\frac{eB}{2m}H|\varphi\rangle = \lambda|\varphi\rangle, \quad (4.34)$$

where $H \equiv -((D_1)^2 + (D_2)^2)/eB$. We introduce new position and momentum operators as

$$X \equiv \frac{1}{\sqrt{eB}}(i\partial_y + xeB/2), \quad (4.35)$$

$$P_X \equiv \frac{1}{\sqrt{eB}}(-i\partial_x + yeB/2), \quad (4.36)$$

$$Y \equiv \frac{1}{\sqrt{eB}}(i\partial_x + yeB/2), \quad (4.37)$$

$$P_Y \equiv \frac{1}{\sqrt{eB}}(-i\partial_y + xeB/2). \quad (4.38)$$

We can easily check that they satisfy the canonical commutation relations

$$[X, P_X] = [Y, P_Y] = i, \quad (4.39)$$

and others become zero. Then, H reads

$$H = P_X^2 + X^2. \quad (4.40)$$

The transverse motion of charged scalar field is given by a harmonic oscillator and thus quantized, which is the so-called Landau quantization. Now, the creation and annihilation operators of harmonic oscillator are

$$a \equiv \frac{1}{\sqrt{2}}(X + iP_X), \quad (4.41)$$

$$a^\dagger \equiv \frac{1}{\sqrt{2}}(X - iP_X), \quad (4.42)$$

$$b \equiv \frac{1}{\sqrt{2}}(Y + iP_Y), \quad (4.43)$$

$$b^\dagger \equiv \frac{1}{\sqrt{2}}(Y - iP_Y), \quad (4.44)$$

where

$$[a, a^\dagger] = [b, b^\dagger] = 1, \quad (4.45)$$

and other commutation relations vanish. Using these operators, the Hamiltonian is given as

$$H = 2a^\dagger a + 1. \quad (4.46)$$

Since the eigenvalues of H are $2n + 1$ with integer n , the energy eigenvalues of charged scalar field read

$$\varepsilon(n, p^3) = \frac{1}{2m}(p^3)^2 + \frac{eB}{2m}(2n + 1). \quad (4.47)$$

Therefore, in the case of spinless boson, all Landau levels including the lowest ones acquire the gap proportional to the magnetic field as given in Eq. (4.47). The energy of ground state increases as the magnetic field does, which causes the restoration of the $U(1)$ symmetry at strong magnetic fields, that is, the superfluidity of charged boson (superconductivity) is destroyed by the magnetic field. This is because the chemical potential must be larger than the gap of lowest excitation to reach the condensed phase. We will numerically show that it occurs even in the interacting theory.

We remark here that the situation is totally different in the case of finite-spin particles, where the lowest Landau levels can be gapless, and thus the order parameter is not necessarily destroyed by the magnetic field. In fact, the opposite behavior, namely, the enhancement of symmetry breaking by the magnetic field, which is referred to as the magnetic catalysis, has been proposed in literatures [113, 114] (for a review, see Ref. [115]).

In the symmetric gauge, the angular momentum L_z reads

$$L_z = b^\dagger b - a^\dagger a, \quad (4.48)$$

and it apparently commutes with H . Therefore, the eigenstates of Eq. (4.34) are labeled by the Landau level n and the angular momentum l as

$$|n, l\rangle = \frac{1}{\sqrt{n!(n+l)!}}(a^\dagger)^n(b^\dagger)^{n+l}|0, 0\rangle, \quad (4.49)$$

where $|0, 0\rangle$ is the Fock vacuum defined by a and b , and satisfies

$$a|0, 0\rangle = b|0, 0\rangle = 0. \quad (4.50)$$

We note that l has the minimum $l = -n$, but it is not bounded from above by n .

Let us now derive the wave function of $|n, l\rangle$ in the coordinate space. We define the complex coordinates

$$\xi \equiv \sqrt{\frac{eB}{2}}(x + iy), \quad (4.51)$$

$$\bar{\xi} \equiv \sqrt{\frac{eB}{2}}(x - iy). \quad (4.52)$$

The creation and annihilation operators read

$$a = \frac{\xi}{2} + \partial_{\bar{\xi}}, \quad a^\dagger = \frac{\bar{\xi}}{2} - \partial_{\xi}, \quad (4.53)$$

$$b = \frac{\bar{\xi}}{2} + \partial_{\xi}, \quad b^\dagger = \frac{\xi}{2} - \partial_{\bar{\xi}}. \quad (4.54)$$

The lowest Landau level wave function with $l = 0$ are obtained by $a|0, 0\rangle = b|0, 0\rangle = 0$, which are

$$\left(\frac{\xi}{2} + \partial_{\bar{\xi}}\right) \varphi_{0,0}(\xi, \bar{\xi}) = 0, \quad (4.55)$$

$$\left(\frac{\bar{\xi}}{2} + \partial_{\xi}\right) \varphi_{0,0}(\xi, \bar{\xi}) = 0 \quad (4.56)$$

in the coordinate space. Here $\varphi_{0,0}(\xi, \bar{\xi}) \equiv \langle \xi, \bar{\xi} | 0, 0 \rangle$. The solution is

$$\varphi_{0,0}(\xi, \bar{\xi}) = \sqrt{\frac{eB}{2\pi}} e^{-\frac{|\xi|^2}{2}}, \quad (4.57)$$

where the normalization of the wave function is chosen as

$$\int \frac{d\xi d\bar{\xi}}{eB} \varphi_{n,l}^*(\xi, \bar{\xi}) \varphi_{n,l}(\xi, \bar{\xi}) = 1. \quad (4.58)$$

The wave function of $|n, l\rangle$ in the complex coordinates reads

$$\begin{aligned} \varphi_{n,l}(\xi, \bar{\xi}) \equiv \langle \xi, \bar{\xi} | n, l \rangle &= \frac{1}{\sqrt{n!(n+l)!}} \langle \xi, \bar{\xi} | (a^\dagger)^n (b^\dagger)^{n+l} | 0, 0 \rangle \\ &= \frac{1}{\sqrt{n!(n+l)!}} \left(\frac{\bar{\xi}}{2} - \partial_{\xi}\right)^n \left(\frac{\xi}{2} - \partial_{\bar{\xi}}\right)^{n+l} \varphi_{0,0}(\xi, \bar{\xi}) \\ &= \frac{1}{\sqrt{n!(n+l)!}} e^{\frac{|\xi|^2}{2}} (-\partial_{\xi})^n (-\partial_{\bar{\xi}})^{n+l} e^{-\frac{|\xi|^2}{2}} \varphi_{0,0}(\xi, \bar{\xi}) \\ &= \frac{1}{\sqrt{n!(n+l)!}} e^{\frac{|\xi|^2}{2}} (-1)^n \frac{1}{\bar{\xi}^l} \left(\frac{\partial}{\partial |\xi|^2}\right)^n |\xi|^{2(n+l)} e^{-\frac{|\xi|^2}{2}} \varphi_{0,0}(\xi, \bar{\xi}) \\ &= \sqrt{\frac{eB}{2\pi}} \sqrt{\frac{n!}{(n+l)!}} (-1)^n \xi^l e^{-\frac{|\xi|^2}{2}} L_n^{(l)}(|\xi|^2), \end{aligned} \quad (4.59)$$

where we used the generalized Laguerre polynomials

$$L_n^{(l)}(x) = \frac{e^x x^{-l}}{n!} \frac{d^n}{dx^n} x^{n+l} e^{-x}. \quad (4.60)$$

Taking $n = 0$, we obtain the lowest Landau level wave functions

$$\varphi_l(x_\perp) = \sqrt{\frac{eB}{2\pi l!}} \left(\frac{eB}{2}\right)^{\frac{l}{2}} (x + iy)^l e^{-\frac{eB}{4}(x^2+y^2)}. \quad (4.61)$$

The longitudinal part is given by $f(x_\parallel)$ and behaves as the plane wave. The important fact is that the transverse dynamics of all the Landau levels is suppressed if $(p_\perp)^2 \equiv (p^1)^2 + (p^2)^2 \ll eB$, because the transverse momentum is scaled as $(p_\perp)^2/eB$. Thus, the theory is effectively reduced to $(1+1)$ dimensions by strong magnetic field.

4.3.2 Magnetic flux quantization

As we have shown in the free theory, the magnetic field can destroy the Bose-Einstein condensate. Therefore, the system energetically disfavors the uniform condensation in the presence of magnetic field. The condensation becomes inhomogeneous and then the topological defect may appear, which is quantized due to the single validness of macroscopic wave function of the Bose-Einstein condensate. In the case of superconductors, it can be observed through the quantization of penetrating magnetic flux. To show this, let us consider a situation where the

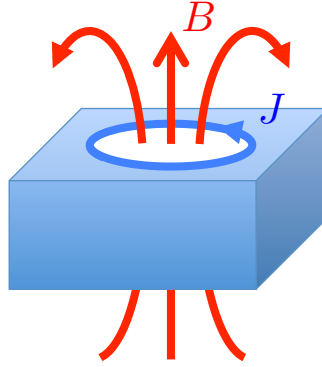


Figure 4.7: Schematic configuration of penetrating magnetic flux.

magnetic field penetrates a defect in superconductor as schematically shown in Fig. 4.7. The electric current is defined as $j^i = \partial\mathcal{L}/\partial A_i$ with the Lagrangian (4.1) or (4.6) and reads

$$\hat{j}^i = \frac{q}{2m} (i\partial^i \hat{\varphi}^\dagger \hat{\varphi} - i\hat{\varphi}^\dagger \partial^i \hat{\varphi}) - \frac{q^2}{m} A^i \hat{\varphi}^\dagger \hat{\varphi}, \quad (4.62)$$

where m and q are mass and charge of condensed boson, respectively. We use hats to indicate quantum operators. In the mean field approximation, the expectation value of observable is obtained by neglecting quantum fluctuation of φ , that is, $\hat{\varphi} = \langle \hat{\varphi} \rangle + \delta\hat{\varphi} \sim \langle \hat{\varphi} \rangle \equiv \Psi$, where Ψ is a macroscopic wave function. Then, the expectation value of electric current is given as

$$\langle \hat{j}^i \rangle = \frac{q}{m} |\Psi|^2 \partial^i \theta - \frac{q^2}{m} A^i |\Psi|^2, \quad (4.63)$$

with θ being the U(1) phase of Ψ . Sufficiently far from the defect, $|\Psi|$ would be uniform. Also, there is no electric current. Therefore, by integrating Eq. (4.63) along a large closed loop enclosing the defect, we have

$$0 = \oint d\mathbf{l} \cdot \nabla\theta - q \oint d\mathbf{l} \cdot \mathbf{A}, \quad (4.64)$$

or equivalently,

$$q\Phi \equiv q \oint d\mathbf{l} \cdot \mathbf{A} = 2\pi n. \quad (4.65)$$

with n being an integer, where we used the single validness of Ψ .

In dilute and low temperature systems, quantum and thermal fluctuations are negligible, and then the above argument holds. In such systems, the quantum vortex nucleation is described by the Gross-Pitaevskii equation [66, 67]. However, when quantum or thermal fluctuation becomes large, it is highly nontrivial how the quantum vortex behaves. For example, the flux quantization may not occur in the presence of strong quantum fluctuation. As mentioned in the introduction, around the critical values of temperature, chemical potential, or magnetic field, the fluctuation grows and then the mean-field description necessarily breaks down. In the following section, we numerically analyze the quantum vortex under in such situations, and show that the magnetic flux quantization actually breaks down when the chemical potential is getting close to its critical value.

4.3.3 Numerical simulation

To see the effect of Landau levels to the Bose-Einstein condensate and also see the quantum vortex nucleation by magnetic field, we have performed the complex Langevin simulation of charged scalar theory in the presence of magnetic field. In the Euclid simulation, although we cannot follow the real-time dynamics of vortex nucleation, which can be studied in the real-time Gross-Pitaevskii simulation [68], we can still study its nonperturbative mechanism.

The lattice action of a two-component boson field $\varphi(\tau, \mathbf{x}) = \varphi^1(\tau, \mathbf{x}) + i\varphi^2(\tau, \mathbf{x})$ in the presence of magnetic field is [71, 116]

$$S_{\text{lat}}[\varphi^1, \varphi^2] = a^3 \sum_{\mathbf{x}} \left[\varphi_{\tau, \mathbf{x}}^* (\varphi_{\tau, \mathbf{x}} - e^{\mu a} \varphi_{\tau - a, \mathbf{x}}) - \frac{1}{2ma} \sum_i \left(\varphi_{\tau, \mathbf{x} + \hat{i}a}^* u_i^\dagger \varphi_{\tau, \mathbf{x}} + \varphi_{\tau, \mathbf{x}}^* u_i \varphi_{\tau, \mathbf{x} + \hat{i}a} - 2|\varphi_{\tau, \mathbf{x}}|^2 \right) + \frac{1}{4} \frac{\lambda}{a^2} a^3 |\varphi_{\tau, \mathbf{x}}|^4 \right], \quad (4.66)$$

where the abelian phase u_i are

$$u_i = \exp(-iaqA_i), \quad (4.67)$$

with

$$A_i = \left(-\frac{1}{2}By, \frac{1}{2}Bx, 0 \right). \quad (4.68)$$

The total number of lattice sites is $V = N_x N_y \times N_z N_\tau = 11^2 \times 10^2$. x and y are ranged to $[-5a, 5a]$. To compare the quantum vortex nucleation by the magnetic field with that by the rotation, we impose the Dirichlet boundary conditions to x and y directions, instead of the conventional periodic boundary conditions, while the periodic boundary condition is imposed to τ and z directions. The chemical potential is introduced on the basis of the standard lattice formulation [90, 91, 106] as discussed in Sec. 4.1. We have applied the magnetic field to the superconducting phase just above ($\mu a = 0.30$) and far above ($\mu a = 0.50$) the critical chemical potential $\mu_c a \sim 0.25$. We have numerically solved Eqs. (3.26) and (3.27) with the lattice action (4.66) by adopting the higher order algorithm [107, 108] with the fictitious time step

$\varepsilon = 1.0 \times 10^{-4}a$. Errors were estimated by using the jackknife method. We note that the imaginary parts of observables were found to be consistent with zero within error bars.

First, we show the charge density at $\mu a = 0.30$ and 0.50 as a function of magnetic field in Fig. 4.8. As discussed in Sec. 4.3.1, the magnetic field effectively screens the chemical potential

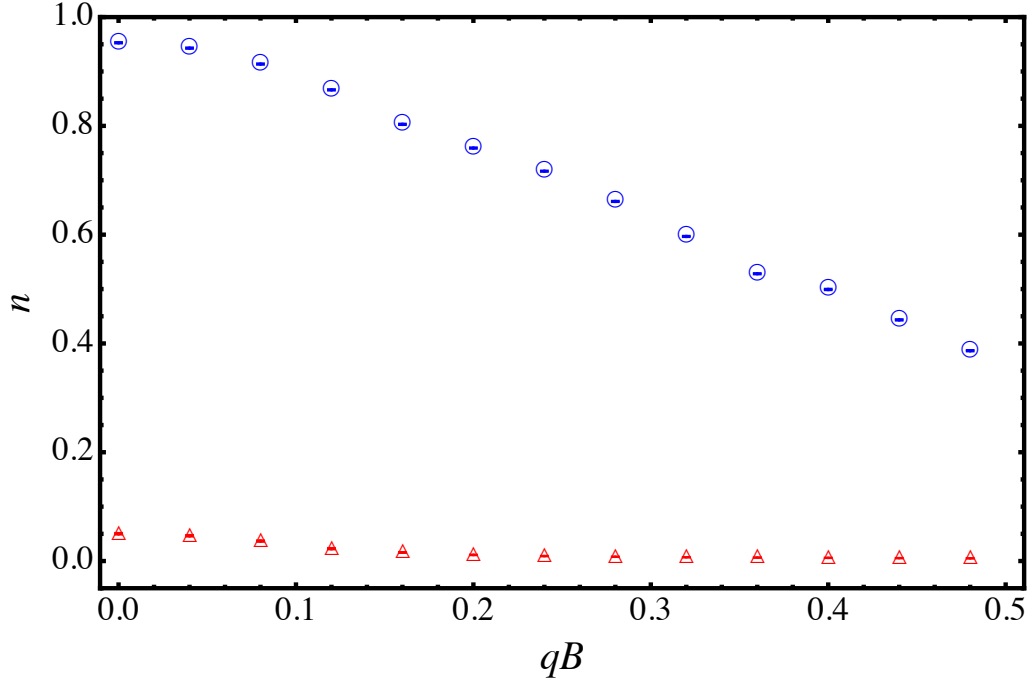


Figure 4.8: Number density n at $\mu a = 0.30$ (triangle) and 0.50 (circle) as a function of magnetic field a^2qB . All the scales are measured in the unit of the lattice spacing a .

due to the Landau levels, and thus the charge density decreases as the magnetic field increases. In Fig. 4.9, we show the condensate fraction at $(x, y) = (0, 0)$, which is defined as

$$R = \text{Re}[G(0, 0, N_z a/2)] / \text{Re}[G(0, 0, 0)], \quad (4.69)$$

with

$$G(x, y, z) = \frac{1}{N_\tau} \sum_{\tau} \langle \phi^*(\tau, x, y, z) \phi(\tau, x, y, 0) \rangle. \quad (4.70)$$

At $\mu a = 0.50$ (circle), we can see the clear plateaux, which reflect the vortex nucleation as we find from the quantized circulation shown in Fig. 4.10. On the other hand, at $\mu a = 0.30$ (triangle), the condensate fraction monotonically decreases as the magnetic field increases.

Next, we analyze the quantum vortex nucleation by magnetic field. The direct evidence of quantum vortex nucleation is the quantization of circulation. The circulation of a vortex is defined as the phase integral around it. On the hypercubic lattice, the circulation is written as the integration along the square loop. Thus, we have calculated the circulation of the O(2) angle (U(1) phase) of φ^{1R} and φ^{2R} , which is given explicitly as

$$\hat{\Gamma}(l) = \frac{1}{2\pi} \oint_{l \times l} d\mathbf{x} \left[\tan^{-1} \left(\frac{\varphi_{\tau, \mathbf{x}+\mathbf{j}}^{2R}}{\varphi_{\tau, \mathbf{x}+\mathbf{j}}^{1R}} \right) - \tan^{-1} \left(\frac{\varphi_{\tau, \mathbf{x}}^{2R}}{\varphi_{\tau, \mathbf{x}}^{1R}} \right) \right], \quad (4.71)$$

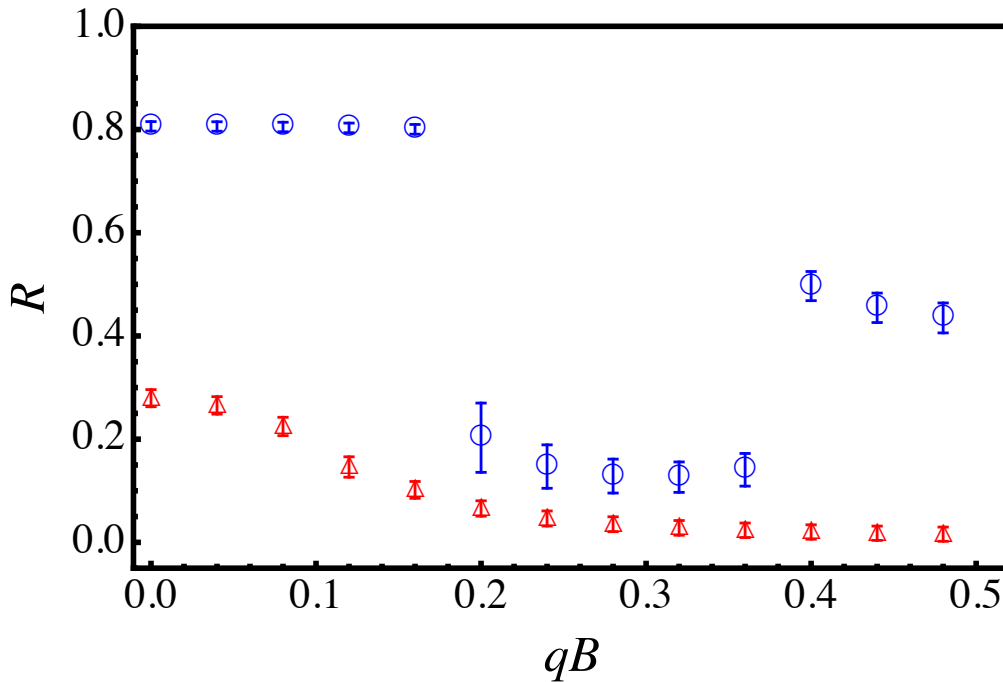


Figure 4.9: Condensate fraction R at $(x, y) = (0, 0)$, and $\mu a = 0.30$ (triangle) and 0.50 (circle) as a function of magnetic field a^2qB . All the scales are measured in the unit of the lattice spacing a .

where \mathbf{j} is unit vector along the loop. The size of the loop is $l \times l$ ($2 \leq l \leq 10$ in our simulation) and the center of the loop is placed at $(x, y) = (0, 0)$. In each configuration of the ensemble, $\hat{\Gamma}(l)$ must be integer because of the single-valuedness of wave functions, but is not necessarily the same in different configurations. Therefore, the expectation value of circulation $\Gamma(l) \equiv \langle \hat{\Gamma}(l) \rangle$ becomes in general non-integer when the number of vortices strongly fluctuates. The mean-field approximation, where the circulation takes an exact integer value, works well when the fluctuation is negligible.

In Fig. 4.10, we show the circulation as a function of magnetic field in the superconducting phase slightly above ($\mu a = 0.3$) and far above ($\mu a = 0.5$) the critical chemical potential. We can see the clear plateaux at $\mu a = 0.5$, although it does not take exact integer value. On the other hand, at $\mu a = 0.3$, it is not quantized and linearly increases, namely, it behaves like a classical vortex. The result indicates the breakdown of the mean-field approximation as the chemical potential getting close to its critical value.

The spatial positions of vortices can be estimated from the l -dependence of $\Gamma(l)$ shown in Fig. 4.11. At $a^2qB = 0.20$ (triangle), $\Gamma(l) = 1$, and it is almost independent of l in $l \geq 2$. Thus, one vortex exists inside the 2×2 loop, i.e., in $|x| \leq a$ and $|y| \leq a$. At $a\Omega = 0.20$ (diamond), $\Gamma(l)$ increases at $l = 4$. Thus, $3/2$ (or 2) vortices exist in average in $a \leq |x| \leq 2a$ and $a \leq |y| \leq 2a$ ($a \leq |x| \leq 3a$ and $a \leq |y| \leq 3a$). By calculating two-point or three-point correlation functions of loops, we can obtain more detailed information such as intervortex distance or the lattice

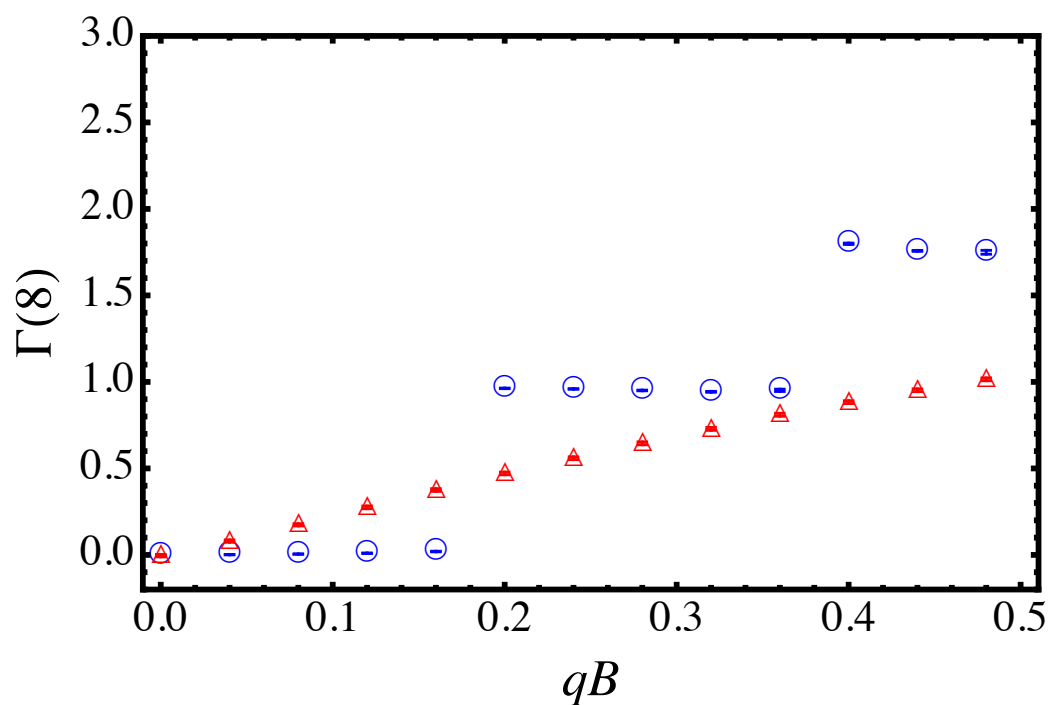


Figure 4.10: Circulation $\Gamma(8)$ as a function of magnetic field qB at $\mu a = 0.3$ (triangle) and 0.5 (circle). The magnetic field qB is measured in the unit of the lattice spacing a .

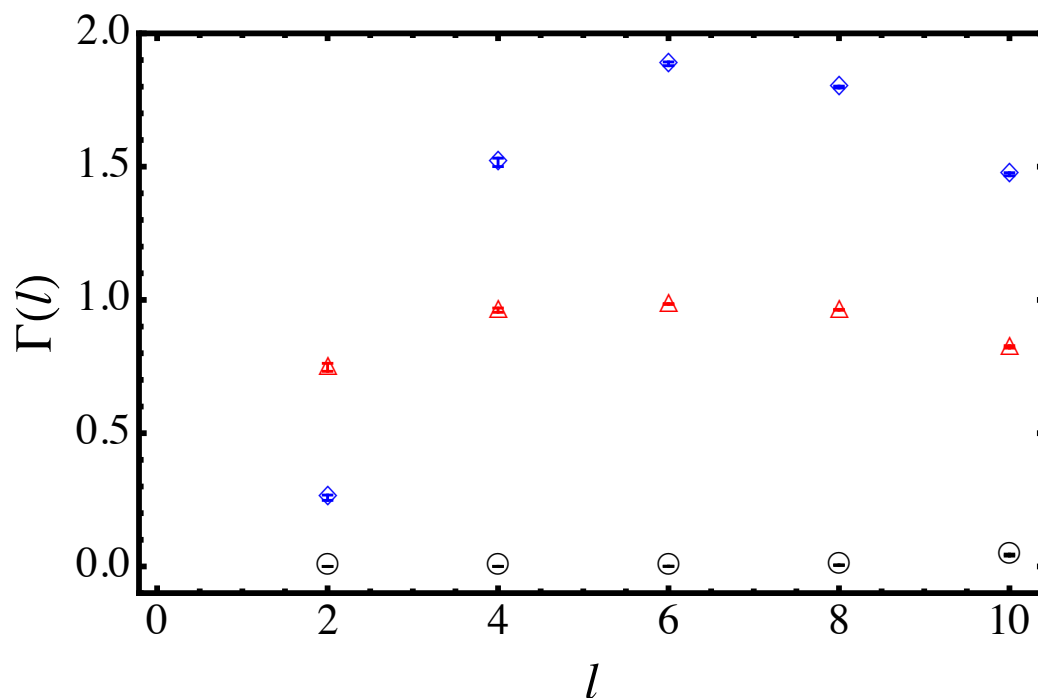


Figure 4.11: Circulation $\Gamma(l)$ as a function of loop size l at $\mu a = 0.5$, and $a^2qB = 0.08$ (circle), 0.20 (triangle) and 0.40 (diamond).

structure, although we must use finer lattice than the present one.

Here, instead of such correlation functions of loops, by using the charge density and condensate fraction, we analyze the vortex structure. As seen in Figs. 4.8 and 4.9, the quantized vortex is reflected in the magnetic field dependence of the charge density and the condensate fraction. In Fig. 4.12, we show the charge density as a function of x at $\mu a = 0.50$ by changing magnetic fields:

$$n(x) = \frac{1}{N_\tau N_z} \sum_{\tau, z} n_{\tau, x, 0, z}. \quad (4.72)$$

Also, in Fig. 4.13, we show the condensate fraction as a function of x at $\mu a = 0.50$:

$$R(x) = \text{Re}[G(x, 0, N_z a/2)] / \text{Re}[G(x, 0, 0)], \quad (4.73)$$

where the boson propagator G is given by Eq. (4.82). In both figures, the number of valleys corresponds to the number of vortices. At $a^2 q B = 0.08$ (circle), $\Gamma(l) = 0$, both charge density and condensate fractions are homogeneous. We note that we imposed the Dirichlet boundary condition to x and y directions, so that all observables drop off near the boundaries as seen in Figs. 4.12 and 4.13. At $a^2 q B = 0.20$ (triangle), $\Gamma(l) = 1$, both charge density and condensate fraction are inhomogeneous. The U(1) symmetry is almost restored at $(x, y) = (0, 0)$ and thus the vortex is localized around this point. The typical size of vortex is $2a$ in the lattice unit, which is consistent with that estimated from the size dependence of the circulation shown in Fig. 4.11. At $a^2 q B = 0.40$ (diamond), $\Gamma(l) = 3/2 - 2$, the U(1) symmetry is partially broken at $(x, y) = (0, 0)$ and there are two valleys at $|x| = a$. Two vortices are separated by the distance $2a$ in lattice unit, which is consistent with the size dependence of the circulation shown in Fig. 4.11. The valleys in Figs. 4.12 and 4.13 are not so deep and thus the vortices are not localized around the valleys. This may be the reason why the circulation shown in Fig. 4.10 is not clearly quantized.

For comparison, we show the charge density (4.72) and the condensate fraction (4.73) at $\mu a = 0.30$ in Figs. 4.14 and 4.15. We do not see clear spatial structures and the U(1) symmetry is homogeneously restored as the magnetic field increases.

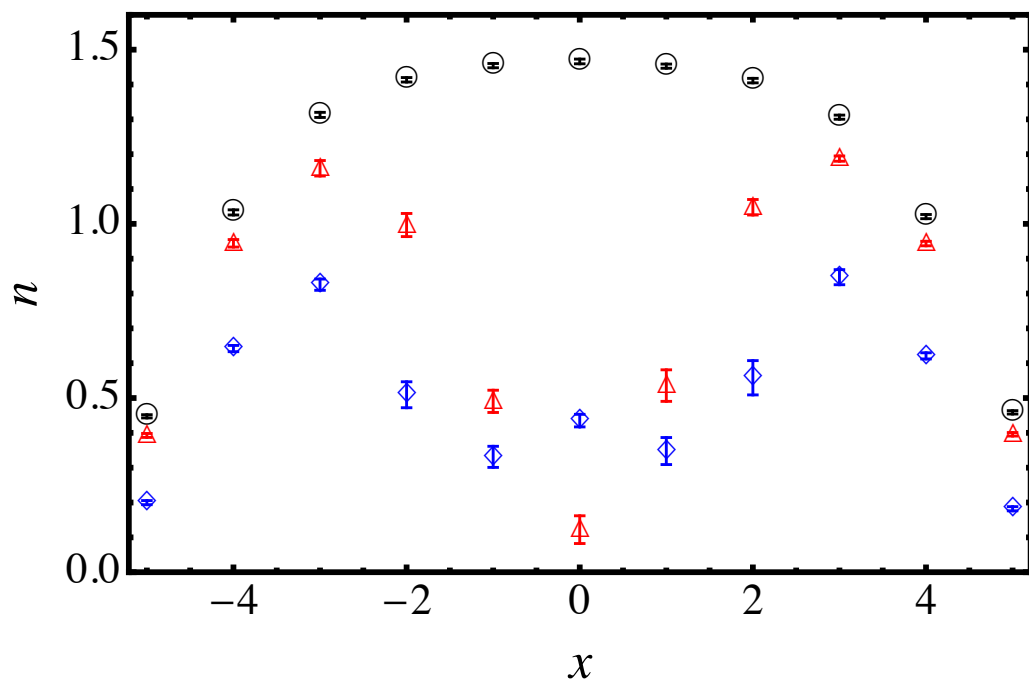


Figure 4.12: Number density n as a function of x at $a^2qB = 0.08$ (circle), 0.2 (triangle) and 0.4 (diamond). All the scales are measured in the unit of the lattice spacing a .

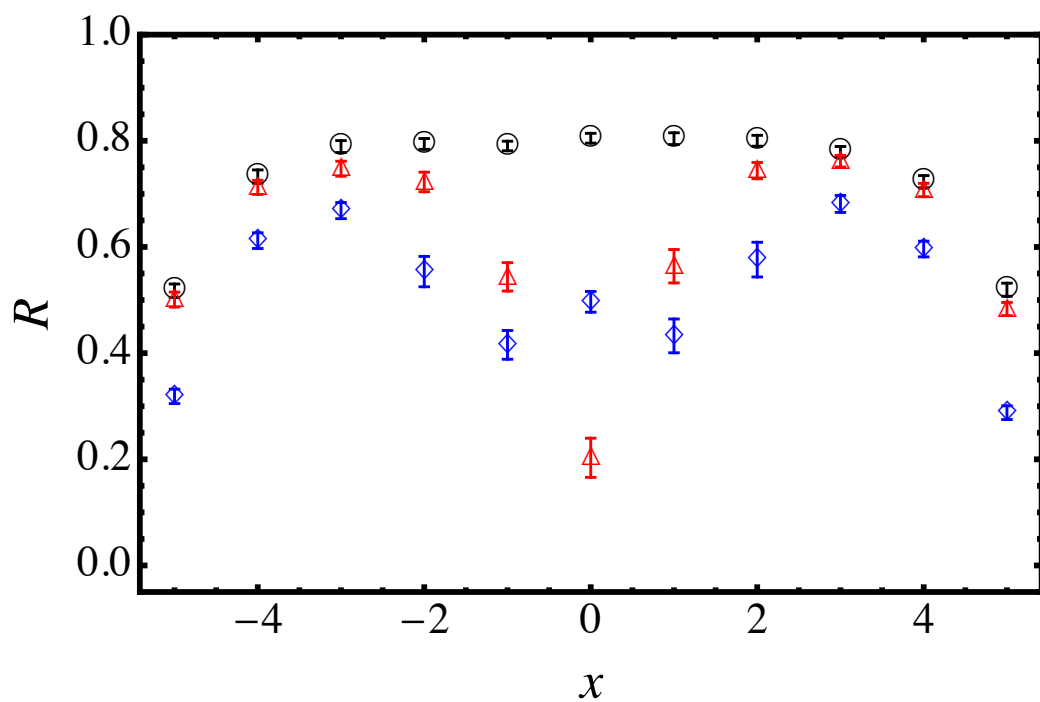


Figure 4.13: Condensate fraction R as a function of x at $a^2qB = 0.08$ (circle), 0.2 (triangle) and 0.4 (diamond). All the scales are measured in the unit of the lattice spacing a .

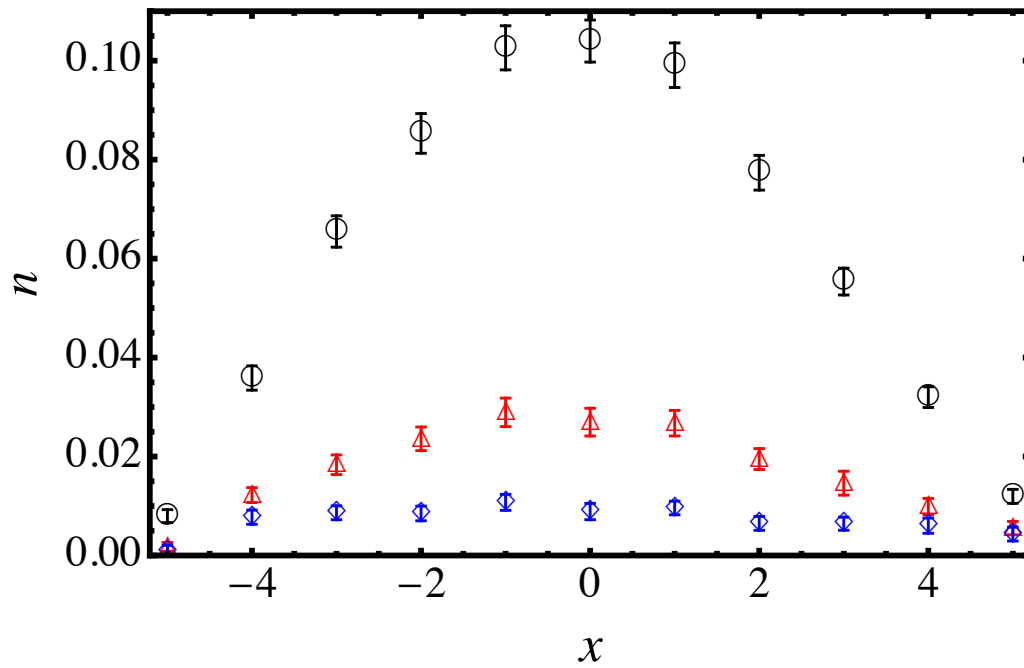


Figure 4.14: Number density n as a function of x at $a^2qB = 0.08$ (circle), 0.2 (triangle) and 0.4 (diamond). All the scales are measured in the unit of the lattice spacing a .

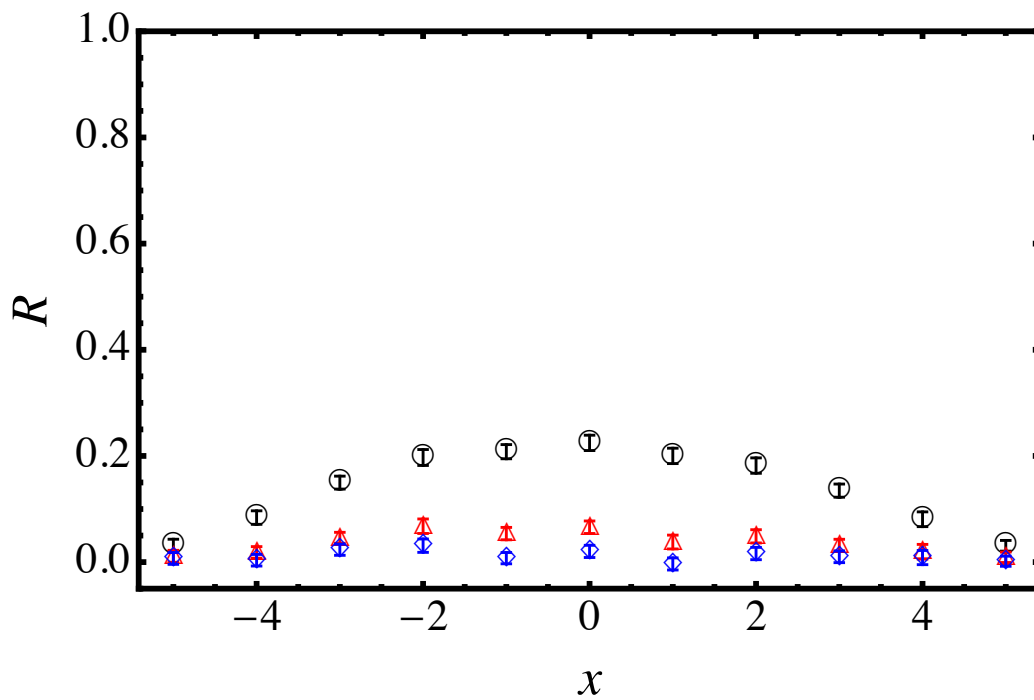


Figure 4.15: Condensate fraction R as a function of x at $a^2qB = 0.08$ (circle), 0.2 (triangle) and 0.4 (diamond). All the scales are measured in the unit of the lattice spacing a .

4.4 Rotation

4.4.1 Bose gas under rotation

Let us consider the situation where the particles are confined in some region by an external potential, and we start to rotate the potential by a constant angular velocity Ω at very low temperatures. After a sufficiently long time, the system is in equilibrium with finite angular momentum, and the rotating Bose-Einstein condensate is created. Standard method to analyze such equilibration process is to solve the real-time dynamics of the Bose-Einstein condensate by using the real-time Gross-Pitaevskii equation as discussed in e.g., Ref. [68]. Another method which can go beyond the mean-field approximation is the Euclid simulation discussed below.

We consider rotations around the z axis: Then in rotating frame, the partition function of the equilibrium state is obtained by replacing H with $H - \Omega L_z$ as

$$Z = \text{tr} e^{-\beta(\hat{H} - \mu\hat{Q} - \Omega\hat{L}_z)}, \quad (4.74)$$

where L_z is angular momentum along the z direction and given explicitly as

$$L_z = xP_y - yP_x = i \int d^3x \varphi^* (-x\partial_y + y\partial_x) \varphi, \quad (4.75)$$

where $P_{x(y)}$ is momentum along the x (y) direction. By using the path integral, the partition function reads

$$Z = \mathcal{N} \int \prod_{\tau, \mathbf{x}} d\varphi_{\tau, \mathbf{x}}^* d\varphi_{\tau, \mathbf{x}} e^{-S}. \quad (4.76)$$

The continuum action of a two-component boson field $\varphi(\tau, \mathbf{x}) = \varphi^1(\tau, \mathbf{x}) + i\varphi^2(\tau, \mathbf{x})$ in rotating frame is [116]

$$S_{\text{con}}[\varphi^1, \varphi^2] = \int d\tau d^3x \left[\varphi^* (\partial_\tau - \mu) \varphi + \frac{1}{2m} |\nabla \varphi|^2 + \frac{1}{4} \lambda |\varphi|^4 - \Omega i \varphi^* (-x\partial_y + y\partial_x) \varphi \right], \quad (4.77)$$

or equivalently,

$$S_{\text{con}}[\varphi^1, \varphi^2] = \int d\tau d^3x \left[\varphi^* (\partial_\tau - \mu) \varphi + \frac{1}{2m} |(\nabla - im\mathbf{\Omega} \times \mathbf{x}) \varphi|^2 - \frac{1}{2} m(x^2 + y^2) \Omega^2 |\varphi|^2 + \frac{1}{4} \lambda |\varphi|^4 \right], \quad (4.78)$$

where $\mathbf{\Omega} = \Omega \hat{z}$. (\hat{i} denotes a unit vector in the i direction.)

We remark here that, except for the centrifugal potential $-\frac{1}{2}m(x^2 + y^2)\Omega^2|\varphi|^2$, the action (4.78) is mathematically equivalent to the action of the spinless charged bosons under magnetic field. In rotating frame, particles effectively couple to the ‘‘magnetic field’’ $q\mathbf{B} = q\nabla \times \mathbf{A} = 2m\Omega\hat{z}$ with $\mathbf{A} = \mathbf{\Omega} \times \mathbf{x}$. Therefore, the quantization of vortices should

be and has been observed also in the rotating Bose-Einstein condensate [41, 42, 43, 44, 45] (See also Ref. [46]).

To perform lattice simulations, we discretize the continuum action (4.78) on the hypercubic lattice. The corresponding lattice action is [71]

$$\begin{aligned}
S_{\text{lat}}[\varphi^1, \varphi^2] &= a^3 \sum_x \left[\varphi_{\tau, \mathbf{x}}^* (\varphi_{\tau, \mathbf{x}} - e^{\mu a} \varphi_{\tau-a, \mathbf{x}}) \right. \\
&\quad \left. - \frac{1}{2ma} \sum_i \left(\varphi_{\tau, \mathbf{x}+ia}^* u_i^\dagger \varphi_{\tau, \mathbf{x}} + \varphi_{\tau, \mathbf{x}}^* u_i \varphi_{\tau, \mathbf{x}+ia} - 2|\varphi_{\tau, \mathbf{x}}|^2 \right) \right. \\
&\quad \left. - \frac{1}{2} ma(x^2 + y^2) \Omega^2 |\varphi_{\tau, \mathbf{x}}|^2 + \frac{1}{4} \frac{\lambda}{a^2} a^3 |\varphi_{\tau, \mathbf{x}}|^4 \right].
\end{aligned} \tag{4.79}$$

The effective gauge field of rotation is introduced by the same manner as the electromagnetic gauge field [92]

$$u_i = \exp(-iaqA_i) = \exp(-iam(\boldsymbol{\Omega} \times \mathbf{x})_i). \tag{4.80}$$

The chemical potential is introduced on the basis of the standard lattice formulation [90, 91, 106], which is discussed in Sec. 4.1.

We note that we have introduced the rotation as an effective magnetic field, not as an external field, which directly couples to the Noether charge of the rotation (angular momentum). Since we cannot maintain the rotational symmetry on the hypercubic lattice, the angular momentum is not obvious. One way to resolve this problem and directly formulate the rotating lattice is to perform lattice simulations on the cylindrical coordinates $\mathbf{x} = (r, \theta, z)$. However, on the cylindrical lattice, there is an apparent singularity at $r = 0$, and thus we have to remove the region around the rotational axis. Also, the cylindrical lattice has the problem of renormalization similar to the case of the anisotropic lattice [117, 118]. Those problems are beyond the scope of this thesis, but we remark here that it is essential when we analyze the quantum vortex nucleation by the rotation in the relativistic Bose-Einstein condensate, where we cannot introduce the rotation as the effective magnetic field.

4.4.2 Numerical simulation

We have numerically solved Eqs. (3.26) and (3.27) with the action (4.79) by adopting the higher order algorithm [107, 108] with the fictitious time step $\varepsilon = 1.0 \times 10^{-4}a$. The total number of lattice sites is $V = N_x N_y \times N_z N_\tau = 11^2 \times 10^2$. x and y are ranged to $[-5a, 5a]$, and the position of rotational axis is set to $(x, y) = (0, 0)$. We take the Dirichlet boundary condition in x and y directions, and take the periodic boundary condition in z and τ directions. We set $ma = \lambda/a^2 = 1.0$. Errors were estimated by using the jackknife method. We note that the imaginary parts of observables were found to be consistent with zero within error bars.

First, we show the charge density at superfluid phase just above ($\mu a = 0.30$) and far above ($\mu a = 0.50$) the critical chemical potential $\mu_c a = 0.25$ as a function of angular velocity Ω in Fig. 4.16. In contrast to the magnetic field, the rotation enhances the charge density. This

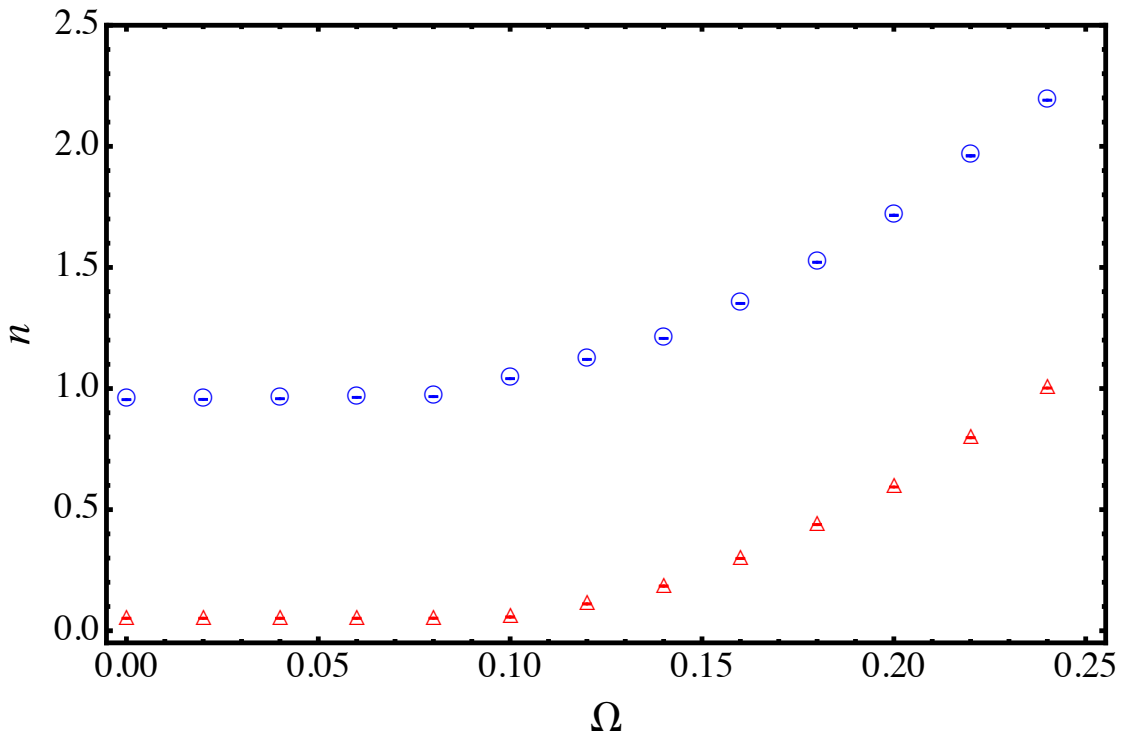


Figure 4.16: Number density n at $\mu a = 0.30$ (triangle) and 0.50 (circle) as a function of angular velocity Ω . All the scales are measured in the unit of the lattice spacing a .

is because the centrifugal potential in Eq. (4.78) or (4.79) effectively plays a role of chemical potential. In Fig. 4.17, we show the condensate fraction at $(x, y) = (0, 0)$, which is defined as

$$R = \text{Re}[G(0, 0, N_z/2)]/\text{Re}[G(0, 0, 0)], \quad (4.81)$$

with

$$G(x, y, z) = \frac{1}{N_\tau} \sum_{\tau} \langle \phi^*(\tau, x, y, z) \phi(\tau, x, y, 0) \rangle. \quad (4.82)$$

At $\mu a = 0.50$ (circle), we can see that the oscillatory behavior between the U(1) symmetry breaking and the U(1) restoration takes place as the angular velocity increases. On the other hand, at $\mu a = 0.30$ (triangle), the condensate fraction decreases as the angular velocity increases, although it shows a non-monotonic behavior around $a\Omega = 0.22$ as seen in Fig. 4.17: This is different from the case of magnetic field shown in Fig. 4.9.

Next, we analyze the quantum vortex nucleation by rotation. The direct evidence of a quantum vortex is the quantized circulation. On the hypercubic lattice, the circulation is given by integrating the phase difference along the square loop as in Eq. (4.71). The size of the loop is $l \times l$ ($2 \leq l \leq 10$ in our simulation) and the center of the loop is placed at $(x, y) = (0, 0)$. The ensemble average $\Gamma(l) \equiv \langle \hat{\Gamma}(l) \rangle$ becomes non-integer if the number of vortices strongly fluctuates, although $\hat{\Gamma}(l)$ is exact integer in each configuration, because of the single-valuedness of wave functions.

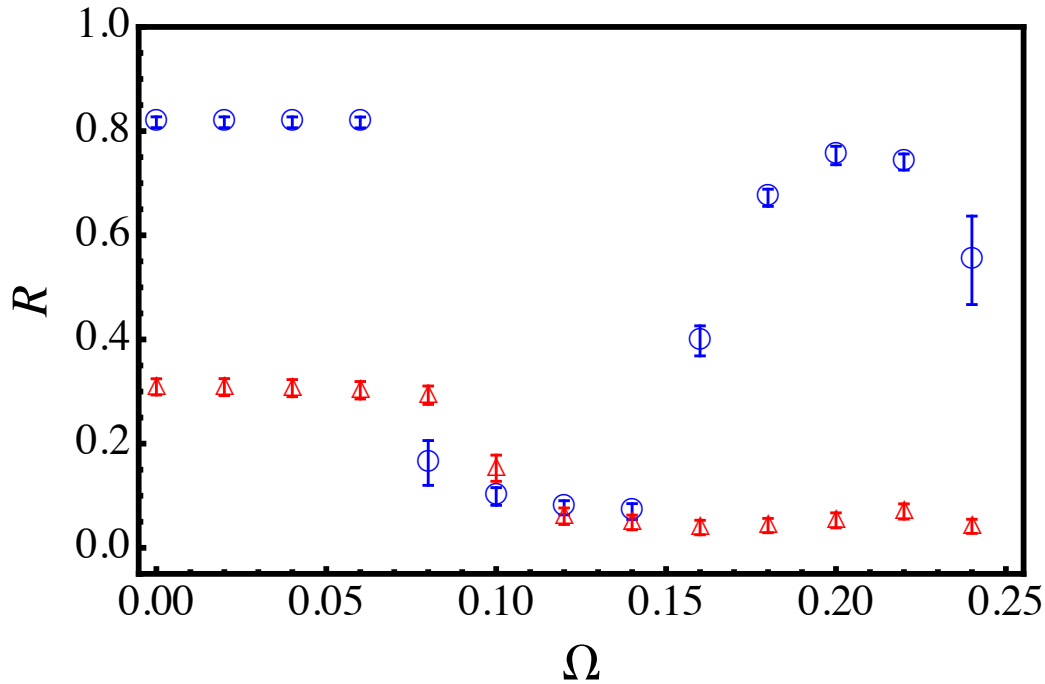


Figure 4.17: Condensate fraction R at $(x, y) = (0, 0)$, and $\mu a = 0.30$ (triangle) and 0.50 (circle) as a function of angular velocity Ω . The angular velocity Ω is measured in the unit of the lattice spacing a .

In Fig. 4.18, we show the circulation as a function of angular velocity in the superfluid phase at $\mu a = 0.3$ and $\mu a = 0.5$. The circulation is clearly quantized to exact integer at $\mu a = 0.5$, in contrast to the case of magnetic field. On the other hand, it is not quantized at $\mu a = 0.3$, which indicates the breakdown of the mean-field approximation as the chemical potential getting close to its critical value. To see the fluctuation of vortices, we show the profile of circulation $\hat{\Gamma}$ obtained from each configuration at $\mu a = 0.3$ and $\mu a = 0.5$ in Figs. 4.19 and 4.20, respectively. When the chemical potential is slightly above the critical chemical potential ($\mu a = 0.3$), at a small angular velocity, the profile shows broad Gaussian distribution. As Ω increases, the profile becomes sharper and finally becomes like a single peak. On the other hand, when the chemical potential is far from the critical chemical potential ($\mu a = 0.5$), the profile shows a very sharp Gaussian distribution.

The spatial positions of vortices can be estimated from the l -dependence of $\Gamma(l)$ shown in Fig. 4.22. At $a\Omega = 0.08$ (circle), $\Gamma(l) = 1$ and it is almost independent of l in $l \geq 2$. Thus, one vortex exists inside the 2×2 loop, i.e., in $|x| \leq a$ and $|y| \leq a$. At $a\Omega = 0.16$ (triangle), $\Gamma(l) = 2$, $\Gamma(l)$ increases at $l = 4$, and thus two vortices exist in $a \leq |x| \leq 2a$ and $a \leq |y| \leq 2a$. At $a\Omega = 0.20$ (diamond), $\Gamma(l) = 4$, two vortices exist in $a \leq |x| \leq 2a$ and $a \leq |y| \leq 2a$, and another two vortices exist inside $2a \leq |x| \leq 3a$ and $2a \leq |y| \leq 3a$. From two-point or more higher-point correlation functions of loops, we can analyze the more detailed information on the vortex structure, although we need finer lattice than the present one.

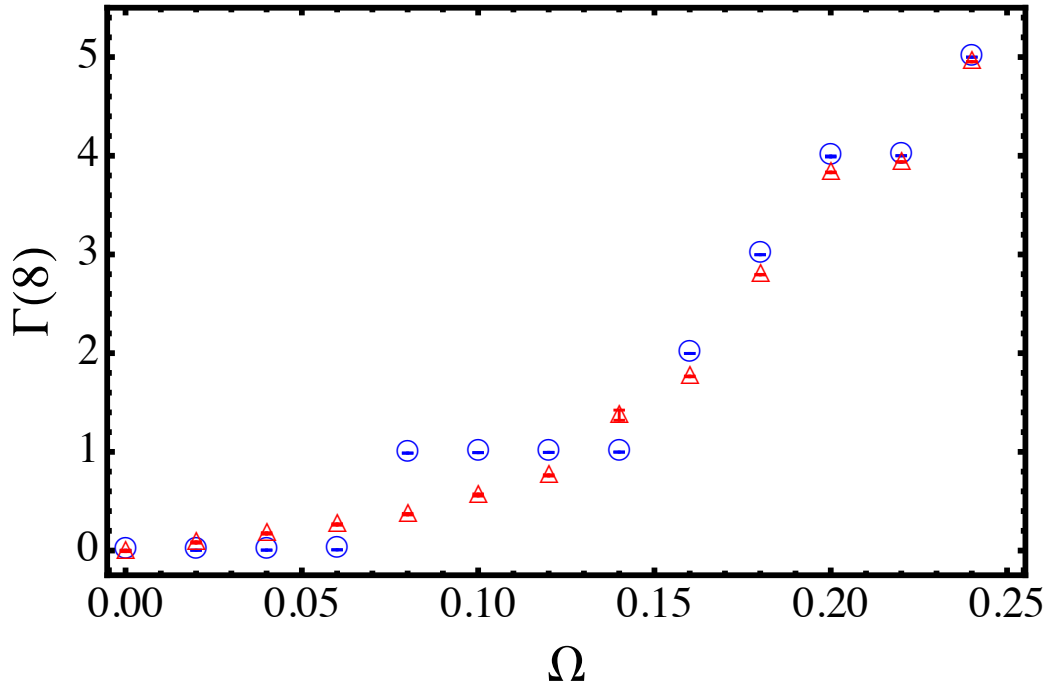
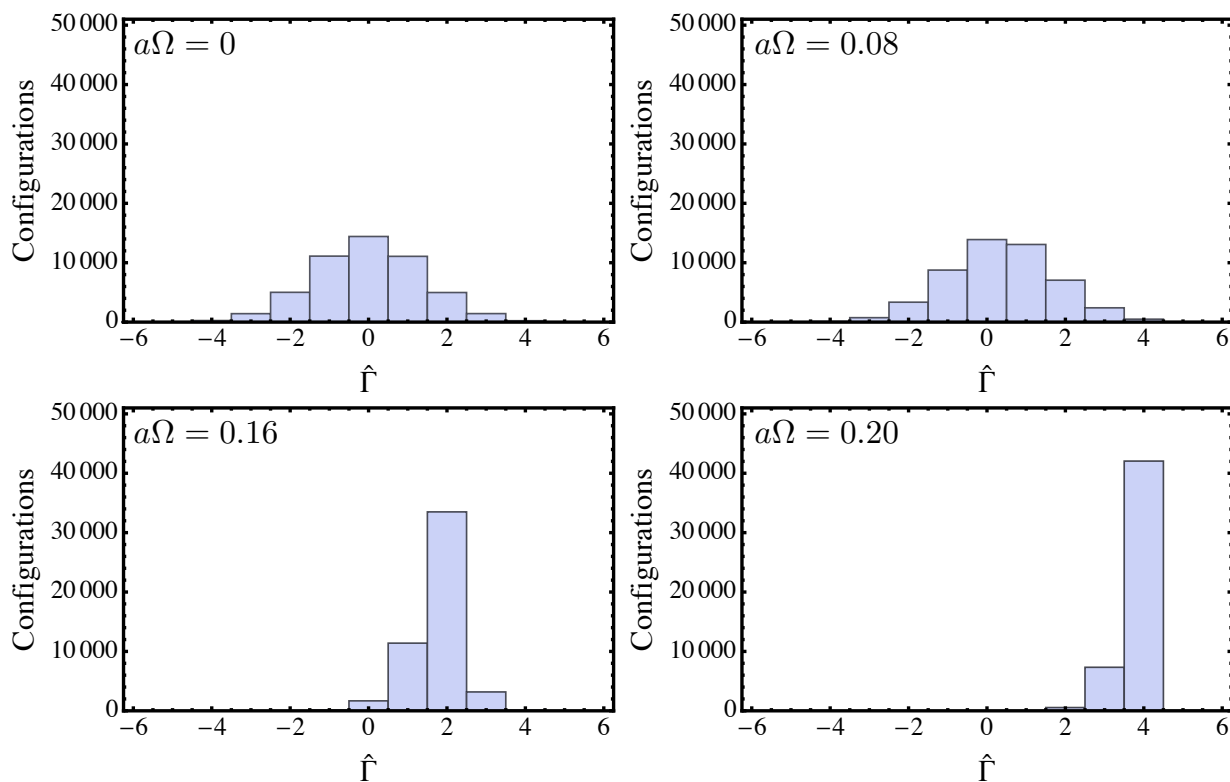
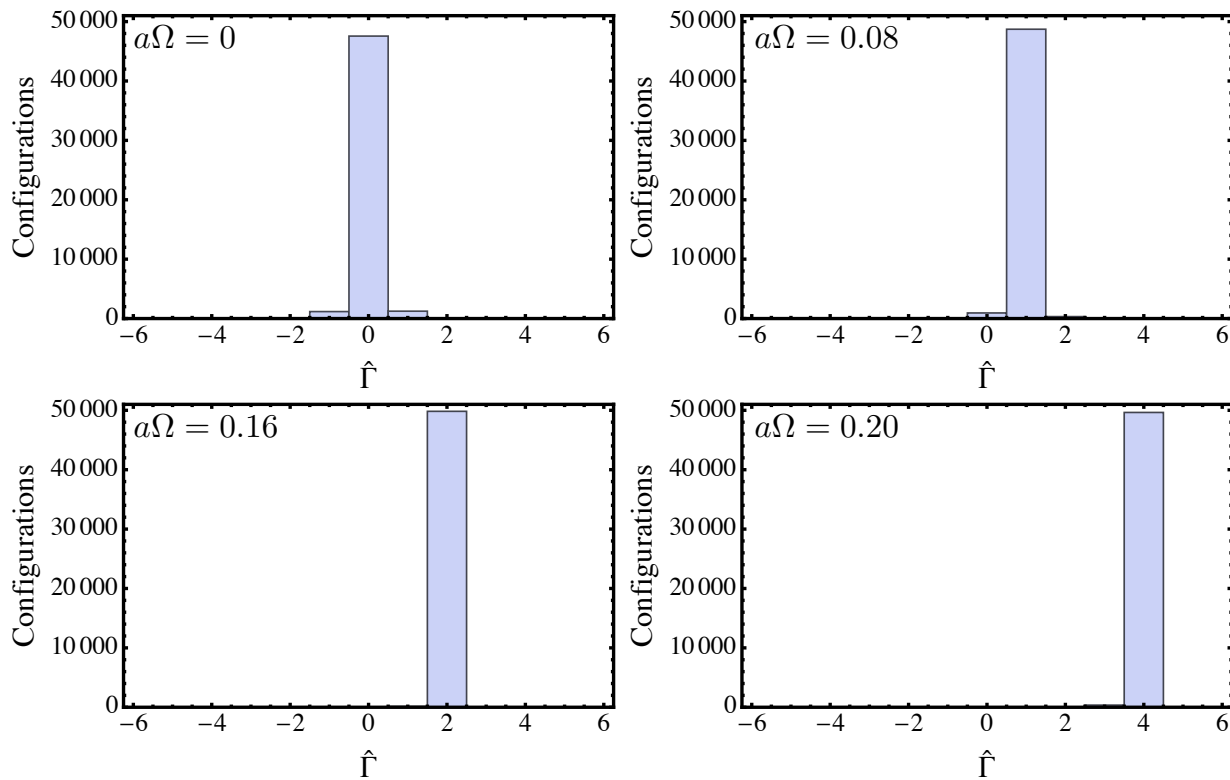


Figure 4.18: Circulation $\Gamma(8)$ as a function of angular velocity Ω at $\mu a = 0.3$ (triangle) and 0.5 (circle). The angular velocity Ω is measured in the unit of the lattice spacing a .

Now, we analyze the vortex structure in an alternative way by using the charge density and condensate fraction. In Figs. 4.22 and 4.23, we show the charge density and the condensate fraction as a function of x in the superfluid phase far from the critical chemical potential ($\mu a = 0.50$), at $a\Omega = 0$ (circle), 0.08 (triangle), 0.16 (diamond), and 0.20 (square). Although we impose the Dirichlet boundary condition in x and y directions, observables shown in Figs. 4.22 and 4.23 do not drop off at the boundaries. This is because particles concentrate on the corners at large angular velocity due to the centrifugal potential. At $a\Omega = 0$ (square), $\Gamma(l) = 0$, both charge density and condensate fraction are homogeneous. At $a\Omega = 0.08$ (circle), $\Gamma(l) = 1$, both charge density and condensate fraction are inhomogeneous. From Fig. 4.23, we find that the U(1) symmetry is restored at $(x, y) = (0, 0)$ and the vortex is localized around this point. The healing length of condensate fraction is $2a$ in lattice unit, which is consistent with the position of vortex estimated from the size dependence of the circulation shown in Fig. 4.18. At $a\Omega = 0.16$ (triangle), $\Gamma(l) = 2$, the condensate fraction is flat around $(x, y) = (0, 0)$, which indicates that two vortices are inside $|x| \leq 4a$, not localized around $(x, y) = (0, 0)$. At $a\Omega = 0.20$ (diamond), $\Gamma(l) = 4$, there are two valleys at $|x| = 2a$, which indicates that two vortices are in each valley and is consistent with Fig. 4.18.

For comparison, we show the charge density (4.72) and the condensate fraction (4.73) in the superfluid phase at $\mu a = 0.30$, and $a\Omega = 0$ (circle), 0.08 (triangle), 0.16 (diamond), and 0.20 (square) in Figs. 4.24 and 4.25. As the angular velocity increases, particles strongly concentrate on the corners, in contrast to the case of $\mu a = 0.50$, shown in Fig. 4.22. We do not see clear

Figure 4.19: Profile of the circulation $\hat{\Gamma}(8)$ at $\mu a = 0.3$.Figure 4.20: Profile of the circulation $\hat{\Gamma}(8)$ at $\mu a = 0.5$.

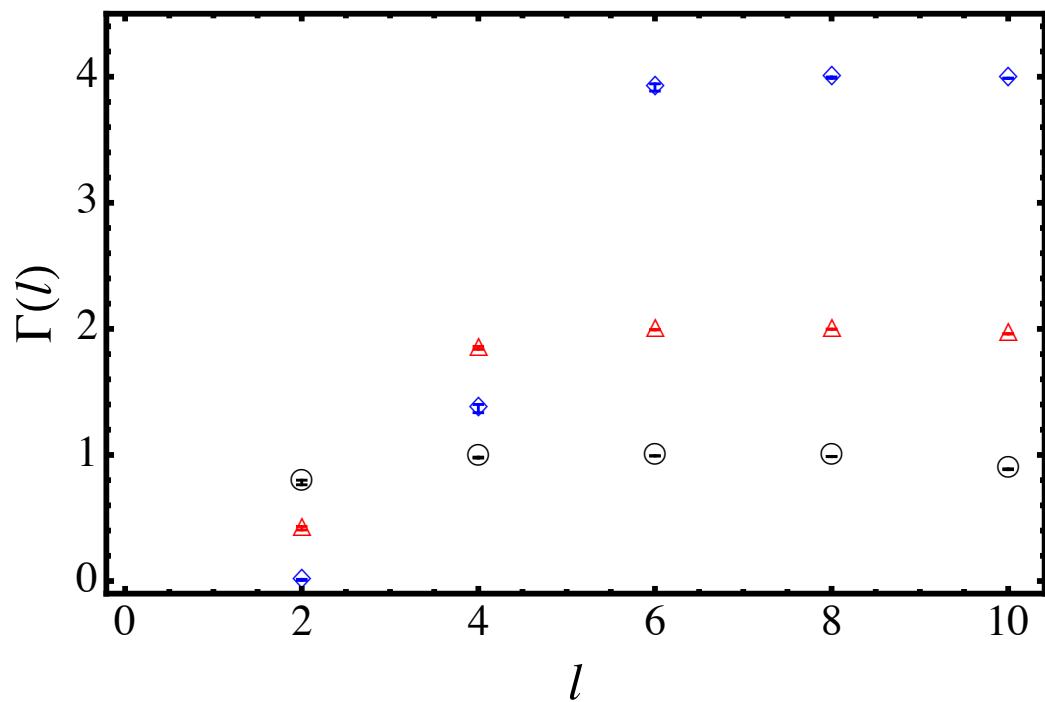


Figure 4.21: Circulation $\Gamma(l)$ as a function of loop size l at $\mu a = 0.5$, and $a\Omega = 0.08$ (circle), 0.16 (triangle) and 0.20 (diamond).

spatial structure associated with quantum vortex nucleation and the density distribution is consistent with that of classical particles under the rotation, although the system is in the superfluid phase at zero angular velocity.

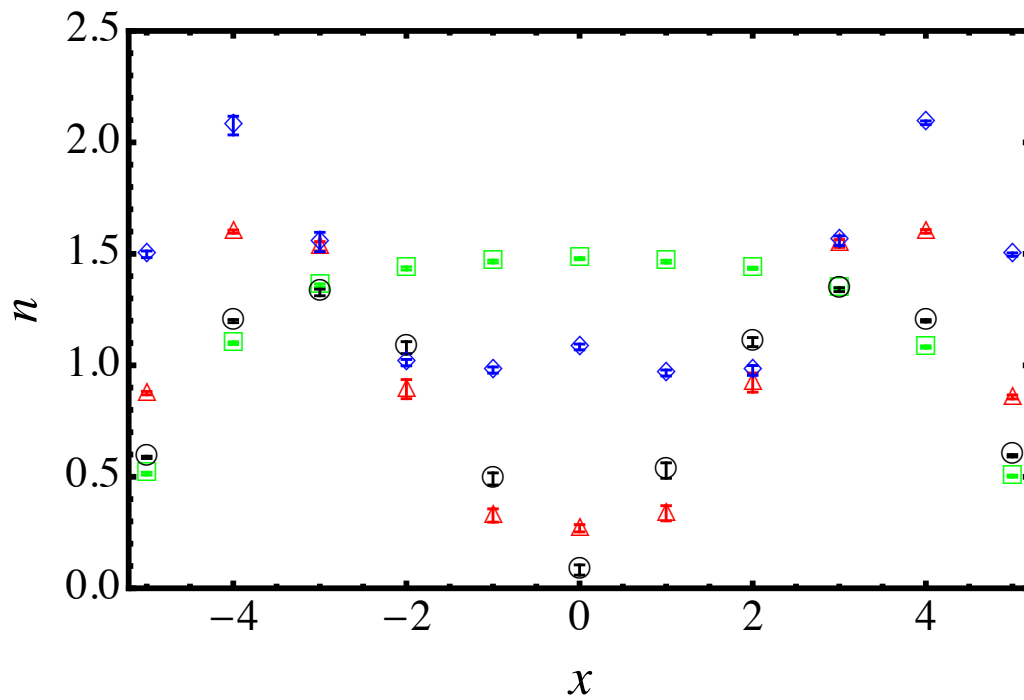


Figure 4.22: Number density n as a function of x at $a\Omega = 0$ (square), 0.08 (circle), 0.16 (triangle) and 0.2 (diamond). All the scales are measured in the unit of the lattice spacing a .

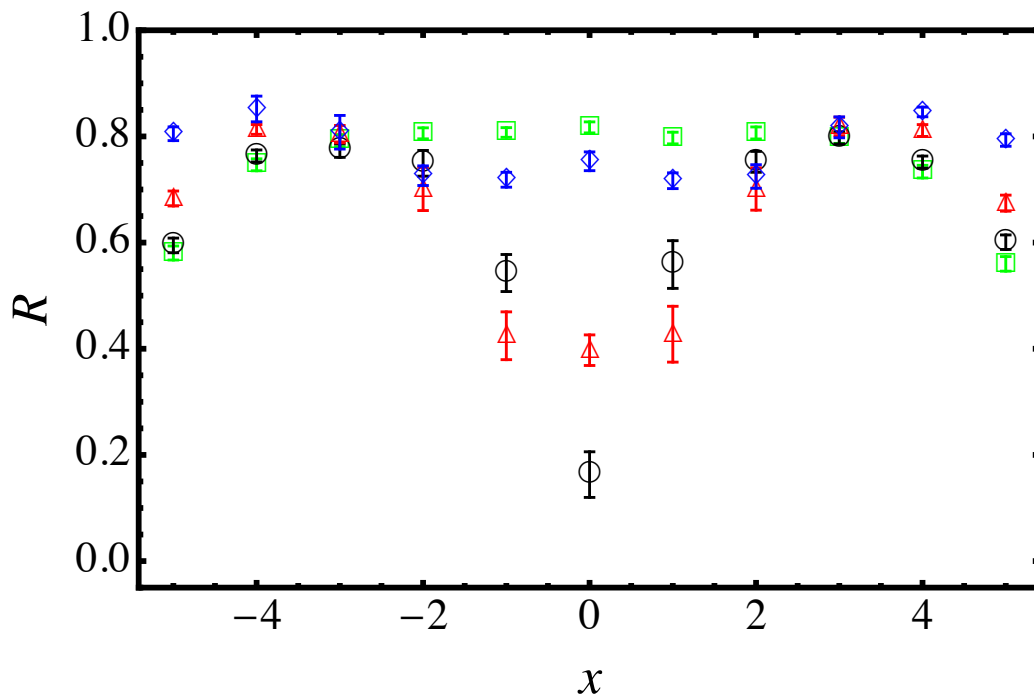


Figure 4.23: Condensate fraction R as a function of x at $a\Omega = 0$ (square), 0.08 (circle), 0.16 (triangle) and 0.2 (diamond). All the scales are measured in the unit of the lattice spacing a .

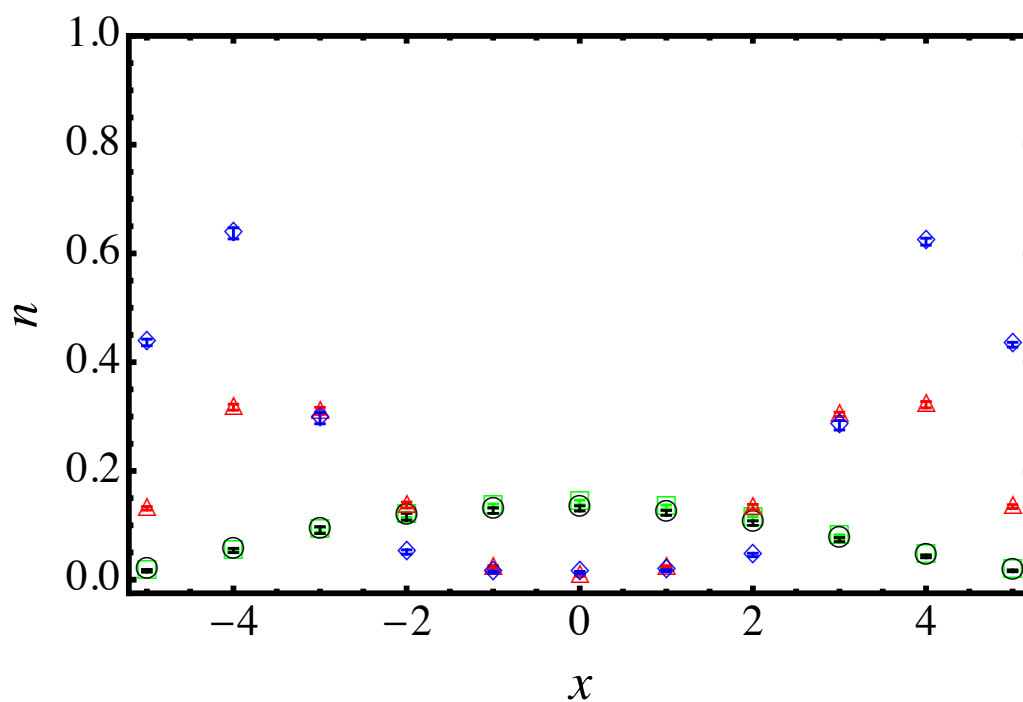


Figure 4.24: Number density n as a function of x at $a\Omega = 0$ (square), 0.08 (circle), 0.16 (triangle) and 0.2 (diamond). All the scales are measured in the unit of the lattice spacing a .

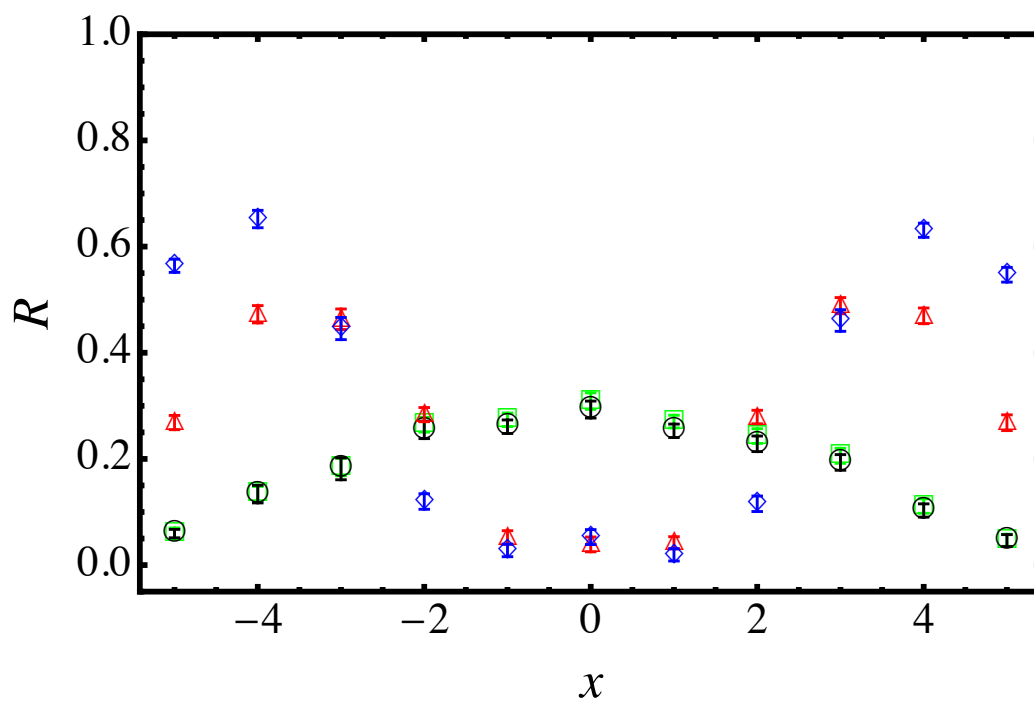


Figure 4.25: Condensate fraction R as a function of x at $a\Omega = 0$ (square), 0.08 (circle), 0.16 (triangle) and 0.2 (diamond). All the scales are measured in the unit of the lattice spacing a .

Chapter 5

Relativistic Bose-Einstein condensate

In this chapter, we perform ab-initio simulations of the relativistic Bose-Einstein condensate under strong electromagnetic fields. We adopt the complex Langevin method, instead of the conventional quantum Monte Carlo method, which suffers from the sign problem.

First, in Sec. 5.1, we reproduce the previous study given in Ref. [87]. We perform the complex Langevin simulation of relativistic scalar field theory at finite chemical potential. We show that the Silver Blaze problem [101] is resolved by using the complex Langevin method [87]. Moreover, we perform the long-range order analysis, which was not done in Ref. [87], and analyze the spontaneous $U(1)$ symmetry breaking.

Then, in Sec. 5.2, we analyze the Bose-Einstein condensate in the presence of Minkowski electric field, which is our original work. Contrary to the nonrelativistic theories, in relativistic theories, the particle production in the vacuum can occur via the Schwinger mechanism [112]. As mentioned in Sec. 4.2.1, the Minkowski electric field can be introduced as a coordinate-dependent real chemical potential. Therefore, the sign problem, in general, occurs in the presence of electric field. We perform the first ab-initio simulation of particle production in such general system by using the complex Langevin method. We show that the charge distribution is generated according to the vector potential. We also analyze the associated $U(1)$ symmetry breaking by performing the long-range order analysis.

Finally, in Sec. 5.3, we analyze the relativistic Bose-Einstein condensate in the presence of magnetic field. We numerically show, as in the case of nonrelativistic theories, that the Bose-Einstein condensate is destroyed by the magnetic field due to the formation of Landau levels. We also analyze the quantum vortex nucleation by the magnetic field. We show that the vortex is quantized far from the critical chemical potential, but it is not just above the critical chemical potential. We also analyze the fluctuation of vortices by performing the same analysis given in the previous chapter.

5.1 Chemical potential

We consider relativistic complex scalar field φ in the presence of external electromagnetic fields. The continuum Euclid action is

$$S_{\text{con}} = \int d\tau d^3x \left[|(\partial_\mu - iqA_\mu^E) \varphi|^2 + m^2 |\varphi|^2 + \lambda |\varphi|^4 \right], \quad (5.1)$$

where A_μ^E are external Euclid gauge fields. In this chapter, we use the convention of $x^\mu = (x^0, x^1, x^2, x^3) = (\tau, \mathbf{x})$ and $x_\mu = (x_0, x_1, x_2, x_3) = (\tau, \mathbf{x})$. The Einstein convention is understood for repeated indices, i.e., $A_\mu B_\mu = A_0 B_0 + A_1 B_1 + A_2 B_2 + A_3 B_3$. We note that the coupling constant λ is dimensionless in (1+3) dimensional relativistic field theory, but it is not in (1+3) dimensional nonrelativistic theory.

To perform lattice simulations, we discretize the continuum action (5.1) on the hyper cubic lattice. The corresponding lattice action is

$$S_{\text{lat}} = a^4 \sum_x \left[-\frac{1}{a^2} \sum_\mu (\varphi_{x+\hat{\mu}a}^* u_\mu^\dagger \varphi_x + \varphi_x^* u_\mu \varphi_{x+\hat{\mu}a} - 2|\varphi_x|^2) + \frac{1}{a^2} m^2 a^2 |\varphi_x|^2 + \lambda |\varphi_x|^4 \right], \quad (5.2)$$

or equivalently,

$$S_{\text{lat}} = a^4 \sum_x \left[-\frac{1}{a^2} \sum_\mu (\cos A_\mu^E \varphi_{x+\hat{\mu}a}^a \varphi_{\tau,x}^a - \sin A_\mu^E \epsilon_{ab} \varphi_{x+\hat{\mu}a}^a \varphi_x^b - 2|\varphi_{\tau,x}|^2) + \frac{1}{2a^2} m^2 a^2 |\varphi_x|^2 + \frac{1}{4} \lambda |\varphi_x|^4 \right], \quad (5.3)$$

where $\varphi = (\varphi^1 + i\varphi^2)/\sqrt{2}$, and $u_\mu(x) = \exp(-iaqA_\mu^E(x))$. Here, as discussed in Sec. 4.1, we discretized the derivative terms as

$$(\partial_\mu - iqA_\mu^E) \varphi_x \rightarrow \left(\varphi_x - e^{iqaA_\mu^E} \varphi_{x-\hat{\mu}a} + O(a^2) \right) / a. \quad (5.4)$$

Then, the kinetic terms read

$$\begin{aligned} & |(\partial_\mu - iqA_\mu^E) \varphi|^2 \\ & \rightarrow \sum_\mu (\varphi_x^* - u_\mu \varphi_{x-\hat{\mu}a}^*) (\varphi_x - u_\mu^\dagger \varphi_{x-\hat{\mu}a}) / a^2 \\ & = \sum_\mu (\varphi_x^* \varphi_x + \varphi_{x-\hat{\mu}a}^* \varphi_{x-\hat{\mu}a} - \varphi_x^* u_\mu^\dagger \varphi_{x-\hat{\mu}a} - \varphi_{x-\hat{\mu}a}^* u_\mu \varphi_x) / a^2. \end{aligned} \quad (5.5)$$

Using the periodicity of the lattice action, we have Eq. (5.2).

In this section, we analyze the superconducting transition at finite chemical potential. For this purpose, we consider quantum field theories at finite temperature and chemical potential,

i.e., in $(1 + 3)$ dimensional Euclid spacetime. The lattice action is obtained from Eq. (5.3) by replacing A_τ^E with the chemical potential μ as $iqA_\tau^E \rightarrow \mu$. It reads [87]

$$S_{\text{lat}} = a^4 \sum_x \left[-\frac{1}{a^2} \left(\cosh \mu a \varphi_{x+\hat{0}a}^a \varphi_x^a + i \sinh \mu a \epsilon_{ab} \varphi_{x+\hat{0}a}^a \varphi_x^b - 2\varphi_{\tau,\mathbf{x}}^a \varphi_{\tau,\mathbf{x}}^a \right) \right. \\ \left. - \frac{1}{a^2} \sum_i \left(\varphi_{\tau,\mathbf{x}+\hat{i}a}^a \varphi_{\tau,\mathbf{x}}^a - 2\varphi_{\tau,\mathbf{x}}^a \varphi_{\tau,\mathbf{x}}^a \right) + \frac{1}{2a^2} m^2 a^2 |\varphi_{\tau,\mathbf{x}}|^2 + \frac{1}{4} \lambda |\varphi_{\tau,\mathbf{x}}|^4 \right]. \quad (5.6)$$

At $\mu a = 0$, the temporal hopping terms are real as in the first line of Eq. (5.6). However, at finite chemical potential, they are not. The lattice action only satisfies $S_{\text{lat}}^\dagger(\mu) = S_{\text{lat}}(-\mu)$ and becomes in general complex. Therefore, the standard Monte Carlo simulation suffers from the sign problem. This lattice action has been analyzed by adopting the complex Langevin simulation in Ref. [87]. Here, for completeness of the thesis, we reproduce their result.

We have numerically solved Eqs. (3.26) and (3.27) with the lattice action (5.6) by adopting the higher order algorithm [107, 108] with $\varepsilon = 2.0 \times 10^{-4}a$. The size of lattice sites is $V = N_x N_y N_z N_\tau = 6^4, 8^4$ and 10^4 . The periodic boundary condition was imposed to all directions. We set $ma = 0.10$ and $\lambda = 0.10$. Errors were estimated by using the jackknife method. We note that imaginary parts of observables were consistent with zero within error bars.

First, we analyze the Silver Blaze problem [101]. The number density is defined as the $n = \partial \mathcal{L} / \partial \mu$ with \mathcal{L} being the lattice Lagrangian density. It is explicitly given as

$$n = \frac{1}{V} \sum_{\tau,\mathbf{x}} n_{\tau,\mathbf{x}}, \quad (5.7)$$

with

$$n_{\tau,\mathbf{x}} = -\varphi_{\tau+a,\mathbf{x}}^* e^{-\mu a} \varphi_{\tau,\mathbf{x}} + \varphi_{\tau,\mathbf{x}}^* e^{\mu a} \varphi_{\tau+a,\mathbf{x}} \\ = (\sinh \mu a \delta_{ab} + i \cosh \mu a \epsilon_{ab}) \varphi_{\tau+a,\mathbf{x}}^a \varphi_{\tau,\mathbf{x}}^b. \quad (5.8)$$

We show the real part of the charge density as a function of chemical potential for the lattice size $V = N^4$ with $N = 6, 8$ and 10 in Fig. 5.1. We can clearly see that the charge density brows up at a critical value of $\mu_c a \sim 0.25$. Figure 5.2 shows the number density near the critical chemical potential. As the lattice volume V is increasing, the transition becomes sharper and sharper and the density goes to zero below μ_c . Thus, the Silver Blaze problem [101] in the relativistic complex scalar field can be correctly handled by the complex Langevin method [87].

We note that in Ref. [87], the critical chemical potential is $\mu_c a \sim 1.15$, and thus larger than one in the lattice unit. As mentioned in Sec. 3.4, the chemical potential should be smaller than one, i.e., $\mu a < 1$ to avoid the lattice artifact, which comes from exponentiating the chemical potential. Therefore, we choose different parameters from Ref. [87], so that the transition occurs at sufficiently small chemical potential.

We have performed a further study on the complex scalar field at finite chemical potential. At zero temperature, as shown in Chap. 2 and Chap. 3, the nonvanishing number density

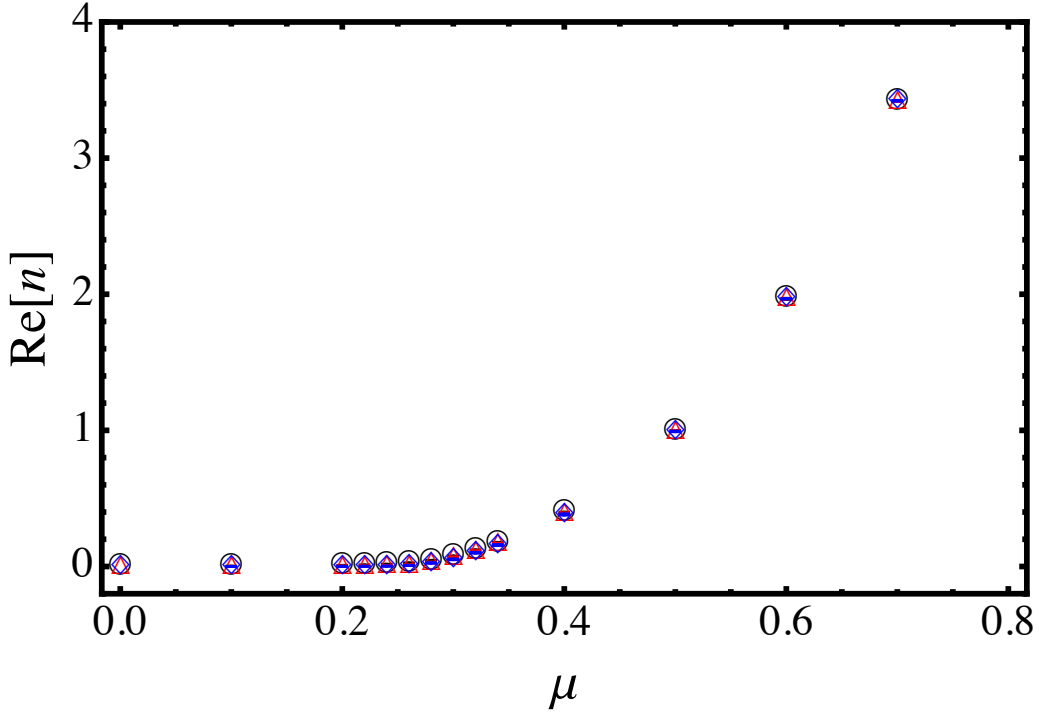


Figure 5.1: Number density n as a function of chemical potential μ at $N = 6$ (circle), 8 (triangle) and 10 (diamond). All the scales are measured in the unit of the lattice spacing a .

implies the Bose-Einstein condensate. To show this, we have performed the long range order analysis. We show the two-point correlation function:

$$G(r) = \frac{1}{N_\tau N_x N_y} \sum_{\tau, x, y} \langle \phi^*(\tau, x, y, r) \phi(\tau, x, y, 0) \rangle, \quad (5.9)$$

at $\mu a = 0.1$ (circle), 0.34 (triangle), and 0.5 (diamond) in Fig. 5.3. The lattice volume is $N^4 = 10^4$. Below μ_c (circle), the boson propagator exponentially drops to zero. On the other hand, above μ_c (triangle and diamond), it goes to a constant value and thus the signature of long range order has been clearly observed. We show the condensate fraction R as a function of μ in Fig. 5.4, which is defined as

$$R = \text{Re}[G(N_z/2)]/\text{Re}[G(0)], \quad (5.10)$$

with $N_z = 10$ in our simulation. We can see that the spontaneous U(1) symmetry breaking occurs simultaneously at μ_c , which is defined as the critical value where the charge density starts to grow up. Now, we find that, by using the complex Langevin method, we can non-perturbatively analyze the spontaneous symmetry breaking in the relativistic scalar field even when the lattice action suffers from the sign problem.

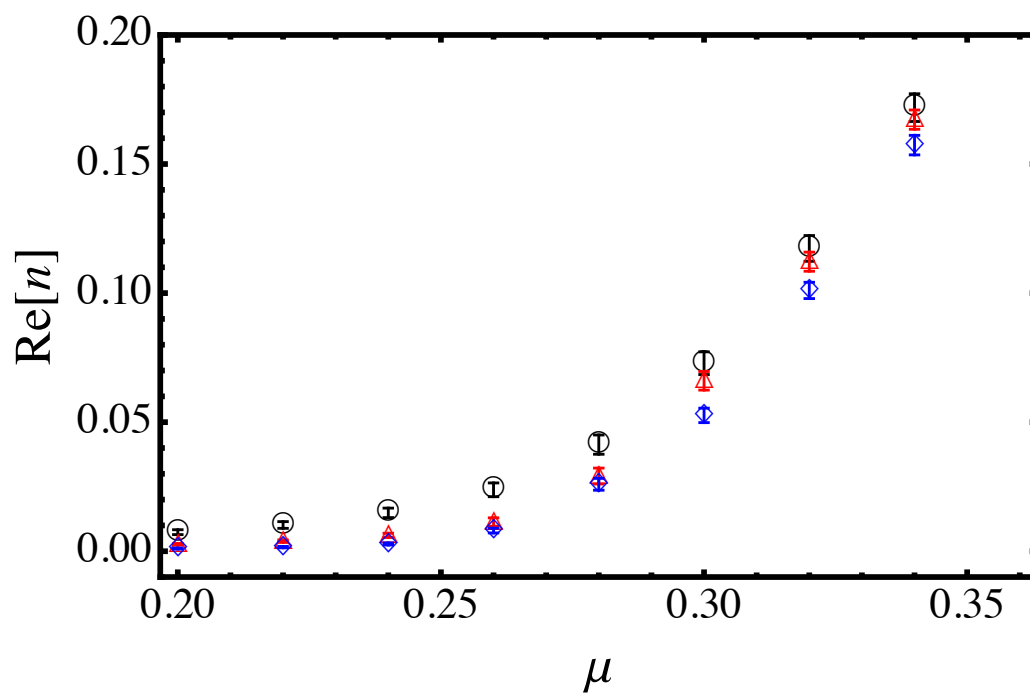


Figure 5.2: Number density n near the transition region at $N = 6$ (circle), 8 (triangle) and 10 (diamond). All the scales are measured in the unit of the lattice spacing a .

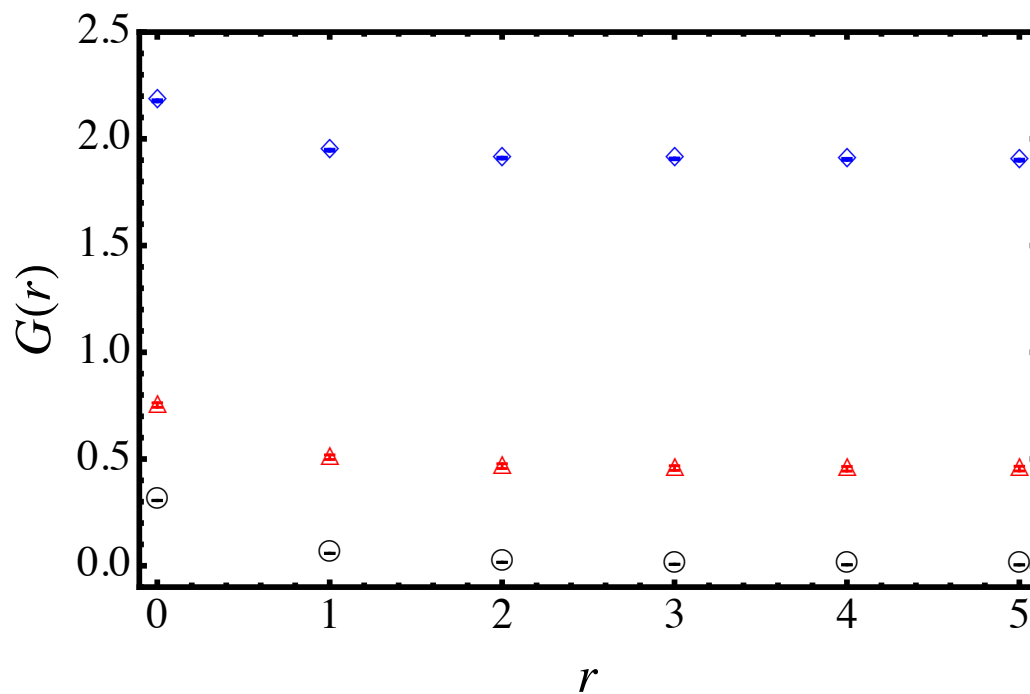


Figure 5.3: Boson propagator $G(r)$ as a function of r at $\mu a = 0.1$ (circle), 0.34 (triangle) and 0.5 (diamond). All the scales are measured in the unit of the lattice spacing a .

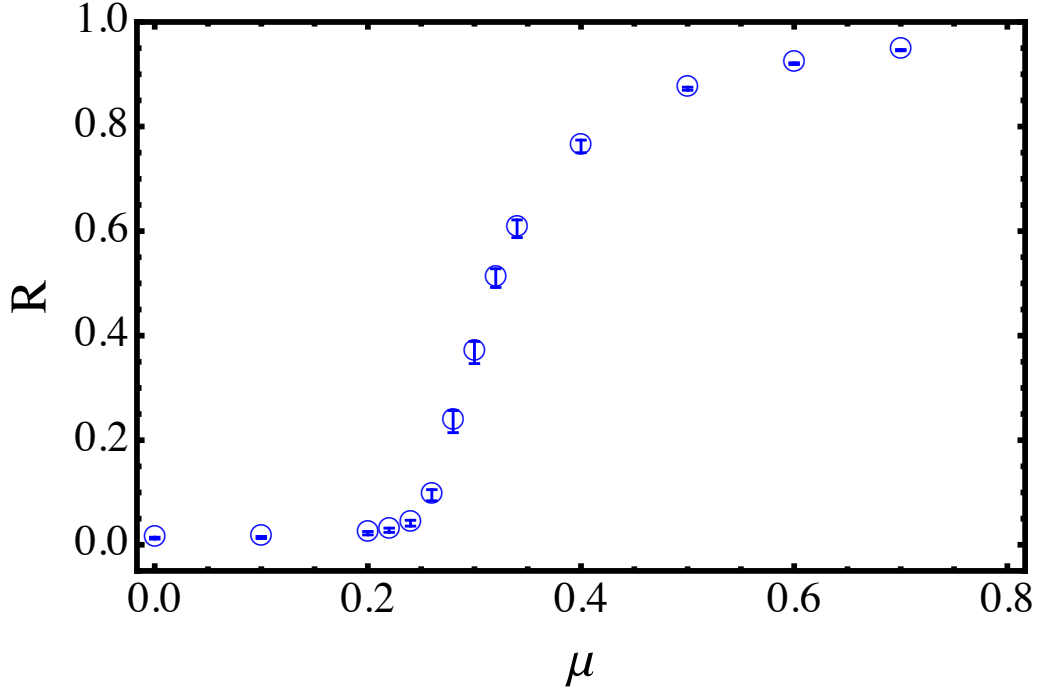


Figure 5.4: Condensate fraction R as a function of μ . All the scales are measured in the unit of the lattice spacing a .

5.2 Electric field

Next, we analyze the relativistic Bose-Einstein condensate in the presence of Minkowski electric field. As mentioned in Sec. 4.2.1, the Minkowski electric field can be introduced as a coordinate-dependent real chemical potential. Therefore, the same strategy can be applicable in the Minkowski electric field and the real chemical potential to evade the sign problem. For example, in the case where particles have the iso-spin symmetric electric charges, the sign problem does not occur and the lattice simulation has been performed by adopting the standard Monte Carlo method [109]. However, when there is no such special symmetry in the system, the sign problem necessarily occurs. We perform the ab-initio simulation of particle production in such situation by using the complex Langevin method.

In Euclid spacetime, although we cannot follow the real-time dynamics associated with the vacuum instability, we can still analyze the nonperturbative mechanism of the particle production. For this purpose, we have applied the Minkowski electric field to the relativistic charged bose gas. The lattice action is

$$\begin{aligned}
S_{\text{lat}} = a^4 \sum_x & \left[-\frac{1}{a^2} \left(\cosh(qaA_0(x)) \varphi_{x+\hat{0}a}^a \varphi_x^a + i \sinh(qaA_0(x)) \epsilon_{ab} \varphi_{x+\hat{0}a}^a \varphi_x^b - 2\varphi_{\tau,\mathbf{x}}^a \varphi_{\tau,\mathbf{x}}^a \right) \right. \\
& \left. - \frac{1}{a^2} \sum_i \left(\varphi_{\tau,\mathbf{x}+\hat{i}a}^a \varphi_{\tau,\mathbf{x}}^a - 2\varphi_{\tau,\mathbf{x}}^a \varphi_{\tau,\mathbf{x}}^a \right) + \frac{1}{2a^2} m^2 a^2 |\varphi_{\tau,\mathbf{x}}|^2 + \frac{1}{4} \lambda |\varphi_{\tau,\mathbf{x}}|^4 \right].
\end{aligned} \tag{5.11}$$

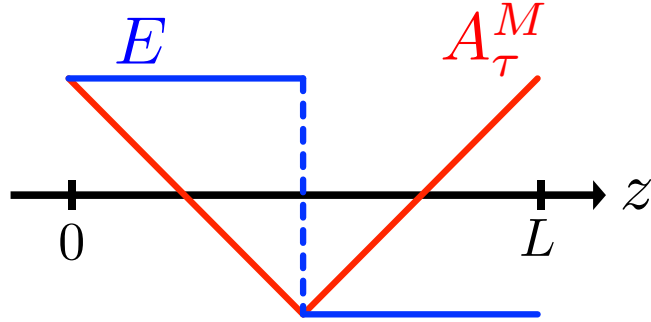


Figure 5.5: Schematic configuration of vector potential A_τ^M and electric field E^M . The periodic boundary condition is imposed.

The lattice volume is $N_x N_y N_z N_\tau$. We consider only the Minkowski electric field and omit the upper script M . We take all spatial components of gauge potentials zero, i.e., $A_i = 0$. We impose periodic boundary condition to all directions. The gauge potential and the associated electric field are shown in Fig. 5.5. We consider electric fields along z direction. The vector potential, which satisfies the periodic boundary condition, is given explicitly as

$$A_0(z) = \begin{cases} -E(z - L/4) & (0 \leq z < L/2) \\ E(z - 3L/4) & (L/2 \leq z < L). \end{cases} \quad (5.12)$$

The associated electric field reads

$$E_z = -\partial_z A_0(z) = \begin{cases} +E & (0 \leq z < L/2) \\ -E & (L/2 \leq z < L). \end{cases} \quad (5.13)$$

We have numerically calculated Eqs. (3.26) and (3.27) with the lattice action (5.11), by adopting the higher order algorithm with $\varepsilon = 2.0 \times 10^{-4}a$. The lattice volume is $V = N_x N_y N_z N_\tau = 10^4$. We set $ma = 0.1$ and $\lambda/a^2 = 0.1$. Errors were estimated by using the jackknife method. We note that imaginary parts of observables were consistent with zero within error bars.

First, we analyze the particle production by electric field. The particle production via the Schwinger mechanism is a pair production, i.e., particles and anti-particles are equally generated. Thus, the net charge of the system vanishes. We have checked that the volume-averaged charge density became zero within the error bar. We show the charge density distribution along the z direction, which is parallel to the electric field in Fig. 5.6:

$$n(z) = \frac{1}{N_\tau N_x N_y} \sum_{\tau, x, y} n_{\tau, \mathbf{x}}, \quad (5.14)$$

with

$$n_{\tau, \mathbf{x}} = (\sinh aqA_0 \delta_{ab} + i \cosh aqA_0 \epsilon_{ab}) \varphi_{\tau+a, \mathbf{x}}^a \varphi_{\tau, \mathbf{x}}^b. \quad (5.15)$$

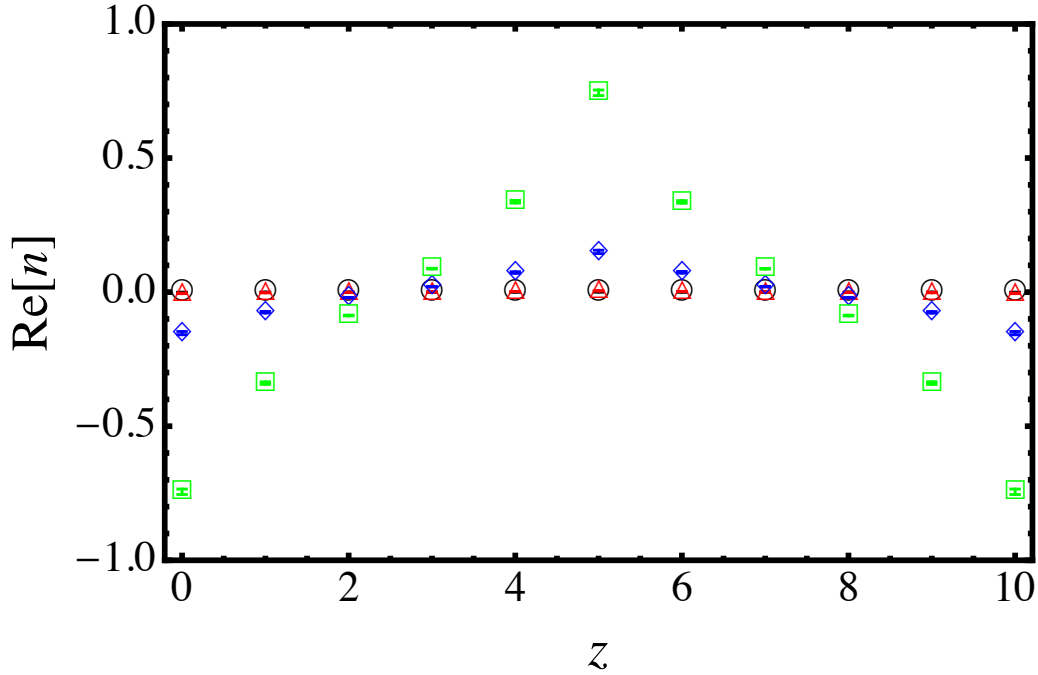


Figure 5.6: Number density n as a function of z at $a^2qE = 0.05$ (circle), 0.15 (triangle), 0.2 (diamond), and 0.25 (square). All the scales are measured in the unit of the lattice spacing a .

We find that there is a critical electric field, above which the particles and anti-particles are produced. The particles and anti-particles accumulate in the highest and lowest voltage regions, respectively. The charge density shows the linear z dependence. This behavior is consistent with the configuration of the vector potential shown in Fig. 5.5, and also with the result in the nonrelativistic theory shown in Fig. 4.3.

As discussed in Chap. 3 and Chap. 4, the nonvanishing number density is accompanied by the U(1) symmetry breaking at zero (or sufficiently low) temperature. To show such non-uniform symmetry breaking, we perform the off-diagonal long-range order analysis. We have calculated the two-point correlation function in the plane perpendicular to the electric field:

$$G(r, z) = \frac{1}{N_\tau N_y} \sum_{\tau, y} \langle \phi^*(\tau, r, y, z) \phi(\tau, 0, y, z) \rangle. \quad (5.16)$$

In Fig. 5.7, we show the two-point correlation function in the perpendicular plane at $z = 5$ in the case of $a^2qE = 0.05$ (circle), 0.15 (triangle), 0.2 (diamond) and 0.25 (square). We can clearly observe the signature of long-range order above the critical electric field (diamond and square). We have also calculated the condensate fraction R :

$$R(z) = \text{Re}[G(N_x a/2, z)] / \text{Re}[G(0, z)], \quad (5.17)$$

with $N_x = 10$ in our simulation. The condensate fraction R as a function of electric field at highest voltage point ($z = 5a$) is shown in Fig. 5.8. We can see the transition from U(1)

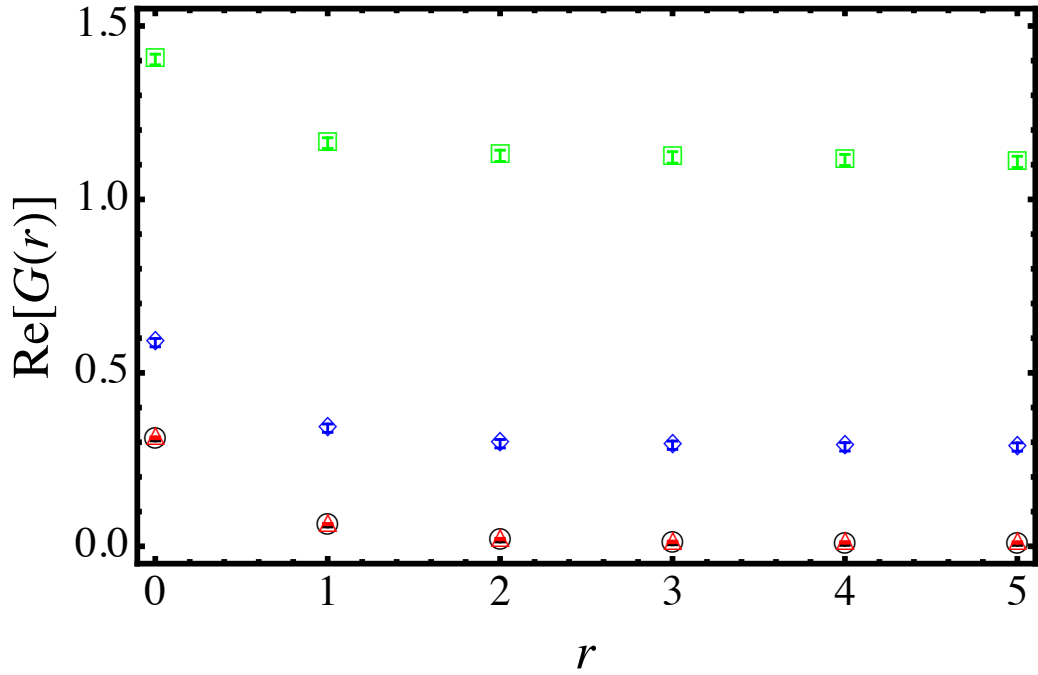


Figure 5.7: Boson propagator $G(r)$ as a function of r at $z = 5$, and $a^2qE = 0.05$ (circle), 0.15 (triangle), 0.2 (diamond) and 0.25 (square). All the scales are measured in the unit of the lattice spacing a .

symmetric to U(1) broken phase at $a^2qE \sim 0.15$. To see the inhomogeneity of symmetry breaking, we show the condensate fraction as a function of z at $a^2qE = 0.05$ (circle), 0.1 (triangle), 0.2 (diamond) and 0.25 (square) in Fig. 5.9. In contrast to the nonrelativistic theory shown in Fig. 4.6, the symmetry breaking occurs also in the lowest voltage regions ($z = 0$ or $10a$). This is because in the relativistic theory, there are two Bose-Einstein condensates of particles and anti-particles. The interplay of these two Bose-Einstein condensate exhibits the periodic behavior of the condensate fraction shown in Fig. 5.9.

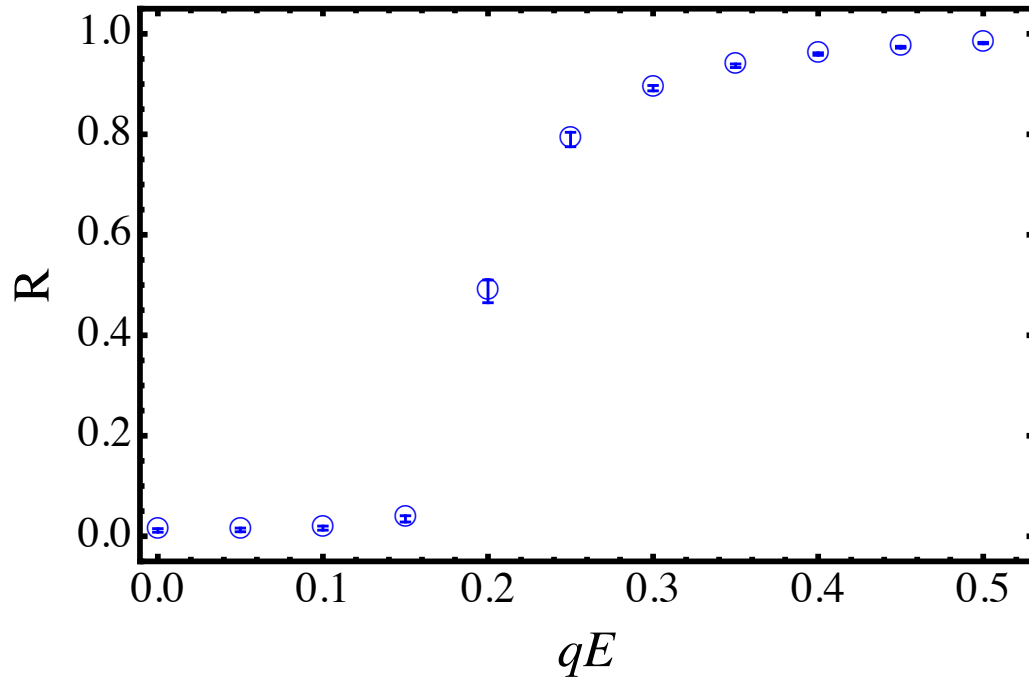


Figure 5.8: Condensate fraction R at $z = 5$ as a function of $a^2 qE$. All the scales are measured in the unit of the lattice spacing a .

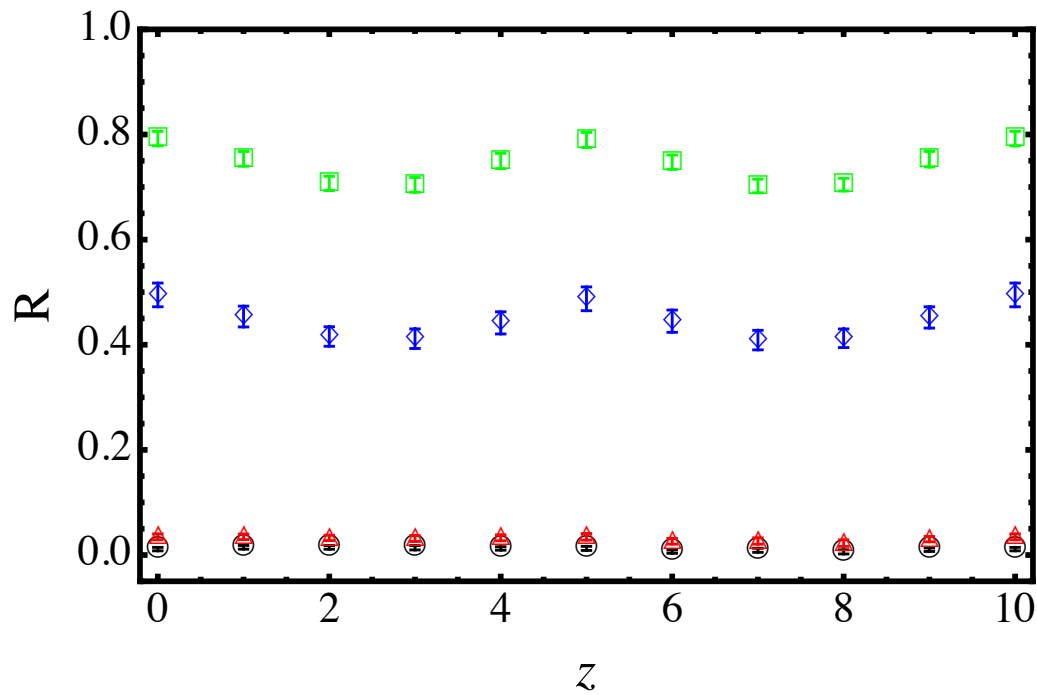


Figure 5.9: Condensate fraction R as a function of z at $a^2 qE = 0.05$ (circle), 0.1 (triangle), 0.2 (diamond) and 0.25 (square). All the scales are measured in the unit of the lattice spacing a .

5.3 Magnetic field

To see the effect of magnetic field to the relativistic Bose-Einstein condensate, we have performed the complex Langevin simulation of charged scalar theory in the presence of magnetic field. The lattice action is

$$\begin{aligned}
S_{\text{lat}} = a^4 \sum_x & \left[-\frac{1}{a^2} \left(\varphi_{x+\hat{0}a}^* e^{\mu a} \varphi_x + \varphi_x^* e^{-\mu a} \varphi_{x+\hat{0}a} - 2|\varphi_x|^2 \right) \right. \\
& - \frac{1}{a^2} \sum_i \left(\varphi_{x+\hat{i}a}^* u_i^\dagger \varphi_x + \varphi_x^* u_i \varphi_{x+\hat{i}a} - 2|\varphi_x|^2 \right) \\
& \left. + \frac{1}{a^2} m^2 a^2 |\varphi_x|^2 + \lambda |\varphi_x|^4 \right],
\end{aligned} \tag{5.18}$$

where the abelian phase u_i are

$$u_i = \exp(-iaqA_i), \tag{5.19}$$

with

$$A_i = \left(-\frac{1}{2}By, \frac{1}{2}Bx, 0 \right). \tag{5.20}$$

The lattice volume is $V = N_x N_y \times N_z N_\tau = 11^2 \times 10^2$. x and y are ranged to $[-5a, 5a]$. We imposed the Dirichlet boundary condition to x and y directions, and the periodic boundary condition to τ and z directions. The chemical potential is introduced on the basis of the standard lattice formulation [87, 90, 91] as discussed in Sec. 4.1. We have applied the magnetic field to the superconducting phase just above ($\mu a = 0.50$) and far above ($\mu a = 0.74$) the critical chemical potential $\mu_c a \sim 0.45$. We have numerically solved Eqs. (3.26) and (3.27) with the lattice action (5.18) by adopting the higher order algorithm [107, 108] with the fictitious time step $\varepsilon = 1.0 \times 10^{-4}a$. Errors were estimated by using the jackknife method. We note that the imaginary parts of observables were found to be zero within error bars.

First, we show the charge density at $\mu a = 0.50$ (triangle) and $\mu a = 0.74$ (circle) as a function of magnetic field in Fig. 5.10. As discussed in Sec. 4.3, the magnetic field effectively screens the chemical potential due to the formation of Landau levels, and thus the charge density decreases as the magnetic field increases. This behavior is clearly observed also in the relativistic theory. In Fig. 5.11, we show the condensate fraction at $(x, y) = (0, 0)$, which is defined as

$$R = \text{Re}[G(0, 0, N_z/2)]/\text{Re}[G(0, 0, 0)], \tag{5.21}$$

with

$$G(x, y, z) = \frac{1}{N_\tau} \sum_\tau \langle \phi^*(\tau, x, y, z) \phi(\tau, x, y, 0) \rangle. \tag{5.22}$$

At $\mu a = 0.74$ (circle), we can see the clear plateaux, which reflect the quantum vortex nucleation as shown in Fig. 5.12. On the other hand, at $\mu a = 0.50$ (triangle), the condensate fraction monotonically decreases, and we do not find any oscillatory behavior.

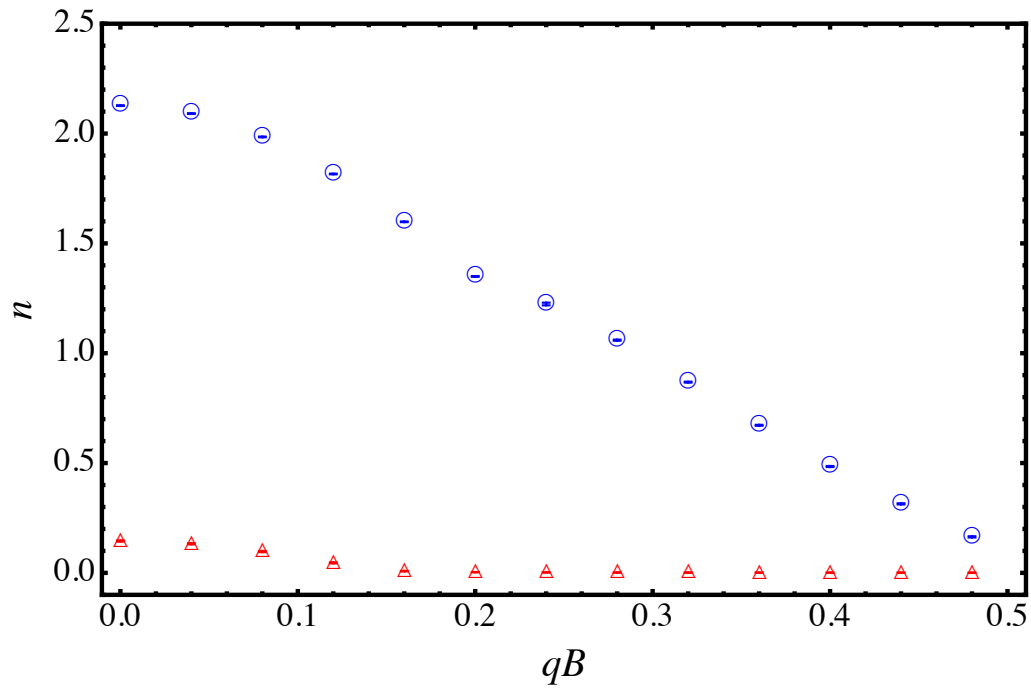


Figure 5.10: Number density n at $\mu a = 0.50$ (triangle) and 0.74 (circle) as a function of magnetic field a^2qB . All the scales are measured in the unit of the lattice spacing a .

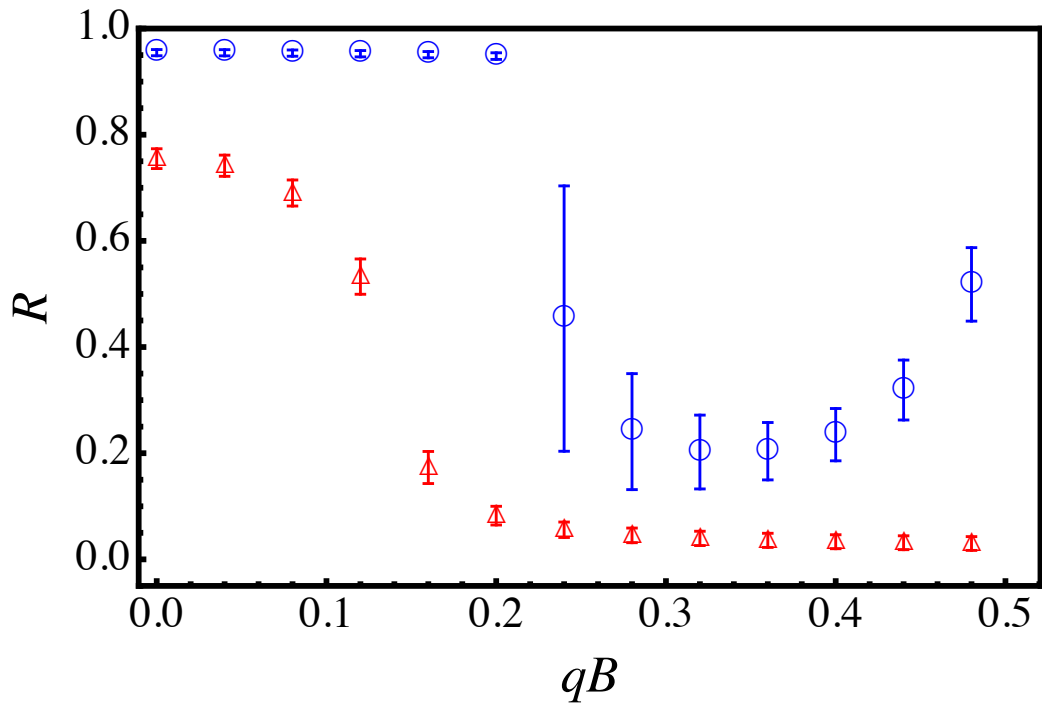


Figure 5.11: Condensate fraction R at $(x, y) = (0, 0)$, and $\mu a = 0.50$ (triangle) and 0.74 (circle) as a function of magnetic field a^2qB . All the scales are measured in the unit of the lattice spacing a .

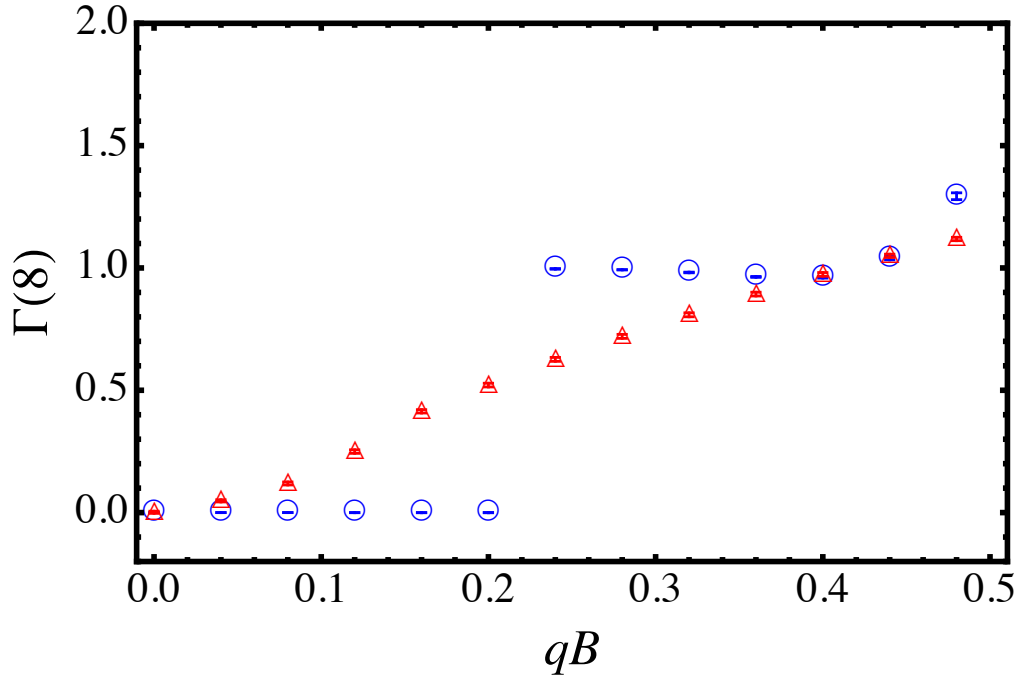
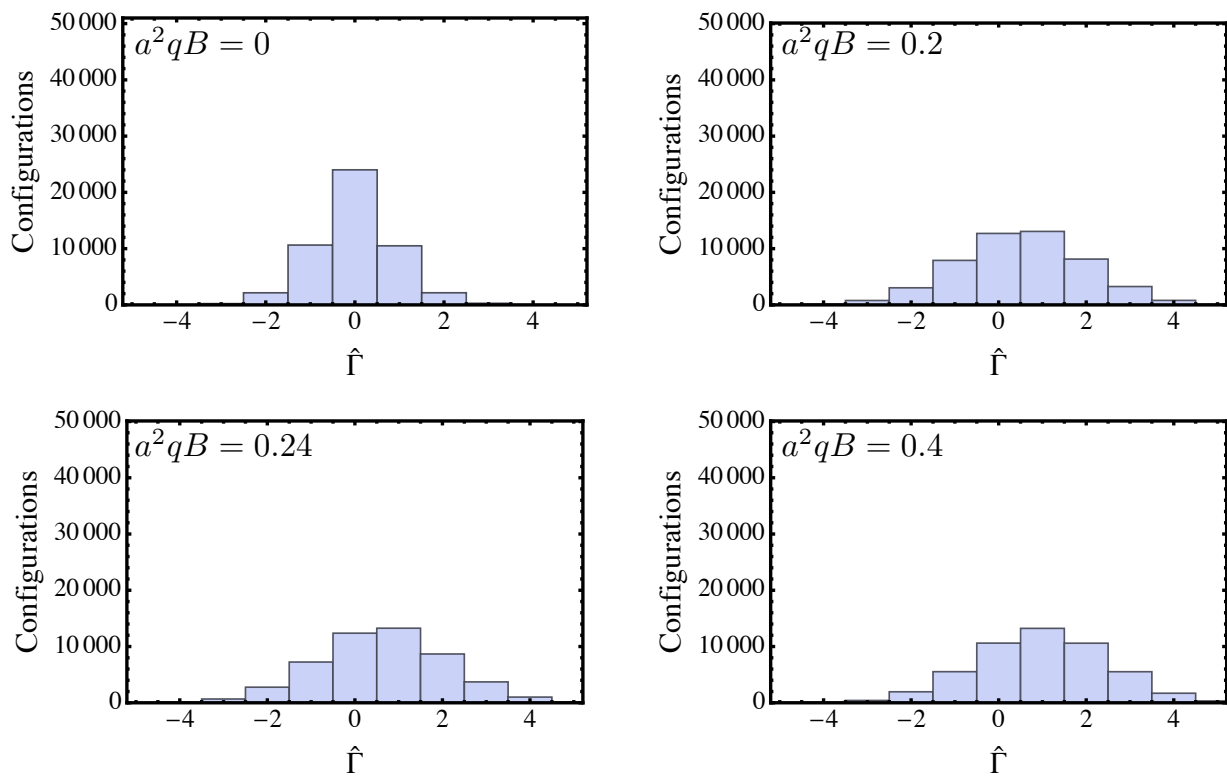
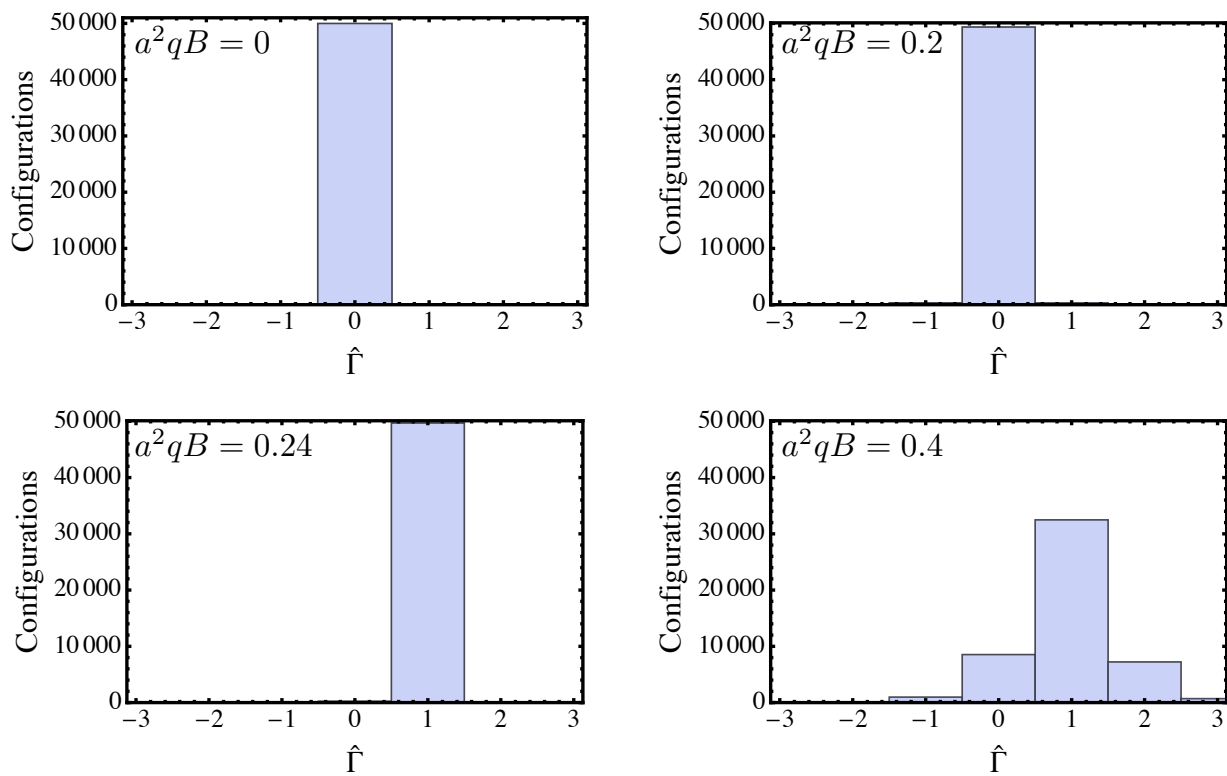


Figure 5.12: Circulation $\Gamma(8)$ as a function of magnetic field qB at $\mu a = 0.3$ (triangle) and 0.5 (circle). The magnetic field qB is measured in the unit of the lattice spacing a .

Next, we analyze the quantum vortex nucleation by magnetic field. The direct evidence of quantum vortex nucleation is the quantization of circulation, which is given in Eq. (4.71). The size of the loop is $l \times l$ ($2 \leq l \leq 10$ in our simulation), and the center of the loop is placed at $(x, y) = (0, 0)$. $\hat{\Gamma}(l)$ becomes integer in each configuration of the ensemble, but its ensemble average can be non-integer when the number of vortices strongly fluctuates.

In Fig. 5.12, we show the circulation as a function of magnetic field in the superconducting phases at $\mu a = 0.5$ (triangle) and 0.74 (circle). We can see that the circulation is clearly quantized below $a^2qB = 0.40$ at $\mu a = 0.74$. On the other hand, at $\mu a = 0.5$, it is not quantized and linearly increases like a classical vortex. The result indicates the break down of the mean-field approximation as the chemical potential getting close to its critical value. Above $a^2qB = 0.40$, both curves show the linear dependence, where the charge density almost goes to zero as shown in Fig. 5.10. It indicates that the quantum fluctuation becomes also stronger near the critical magnetic field, which is clearly seen in Fig. 5.14.

To see the fluctuation of vortices, we show the profile of circulation $\hat{\Gamma}$ obtained from each configuration at $\mu a = 0.5$ and $\mu a = 0.74$ in Figs. 5.13 and 5.14, respectively. At $\mu a = 0.5$, the profile shows a clear Gaussian distribution. Therefore, the number of vortices is strongly fluctuate near the critical chemical potential. On the other hand, when the chemical potential is far from the critical chemical potential ($\mu a = 0.74$), the profile behaves as almost a single peak. However, at $a^2qB = 0.40$, a clear Gaussian distribution appears. It indicates that the fluctuation becomes stronger as the magnetic field increases.

Figure 5.13: Profile of the circulation $\hat{\Gamma}(8)$ at $\mu a = 0.5$.Figure 5.14: Profile of the circulation $\hat{\Gamma}(8)$ at $\mu a = 0.74$.

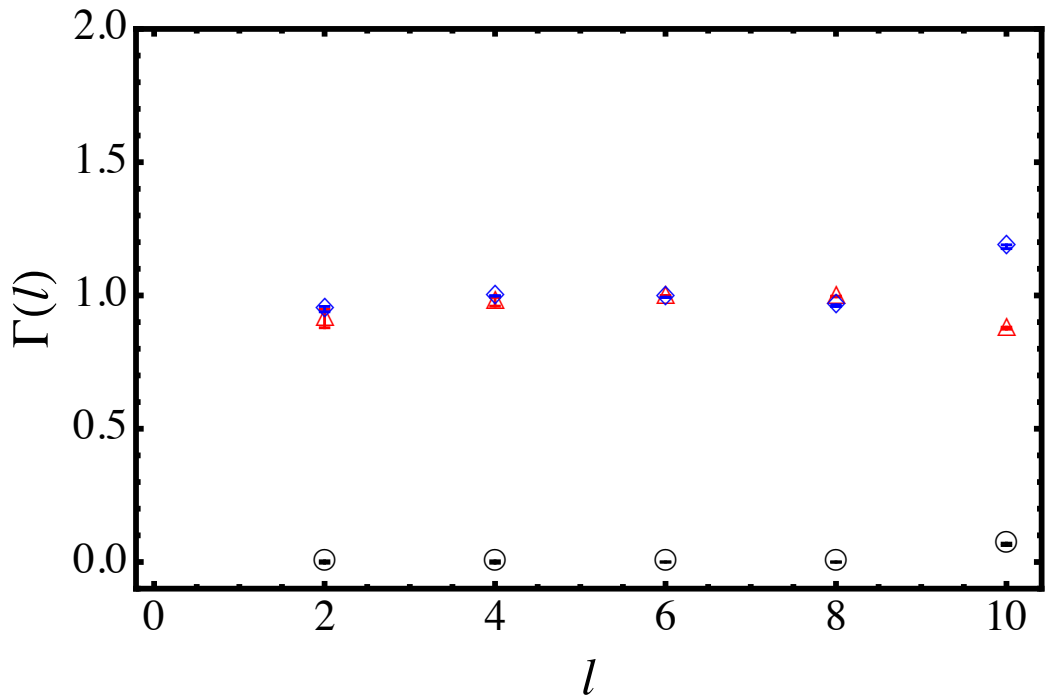


Figure 5.15: Circulation $\Gamma(l)$ as a function of loop size l at $\mu a = 0.74$, and $a^2qB = 0.08$ (circle), 0.20 (triangle) and 0.40 (diamond).

We analyze the spatial positions of vortices from the l -dependence of $\Gamma(l)$ shown in Fig. 5.15. At $a^2qB = 0.20$ (triangle) and 0.40 (diamond), $\Gamma(l) = 1$, and it is almost independent of l in $l \geq 2$. Thus, one vortex exists inside the 2×2 loop, i.e., in $|x| \leq a$ and $|y| \leq a$. The quantum vortex is strongly localized at $(x, y) = (0, 0)$ with depending little on the magnetic field.

To deepen our understanding on the vortex structure in the relativistic Bose-Einstein condensate, we analyze it by using the charge density and condensate fraction. In Fig. 5.16, we show the charge density as a function of x in the superconducting phase at $\mu a = 0.74$ with changing the magnetic fields. Also, in Fig. 5.17, we show the condensate fraction as a function of x . We note that we imposed the dirichlet boundary conditions in the x and y directions, so that these quantities drop off at the boundaries as seen in Figs. 5.16 and 5.17. The charge density and the condensate fraction decrease as a function of magnetic field, which represents the U(1) symmetry is restored as the magnetic field increases. The healing length of the condensate fraction is $1a$ in the lattice unit, which less depends on the magnetic field. We find that the one vortex is strongly localized at $x = 0$, which is consistent with Fig. 5.15.

For comparison, we show the charge density and the condensate fraction in the superconducting phase at $\mu a = 0.50$ in Figs. 5.16 and 5.17, respectively. We do not see any spatial structures and the U(1) symmetry is homogeneously restored as the magnetic field increases.

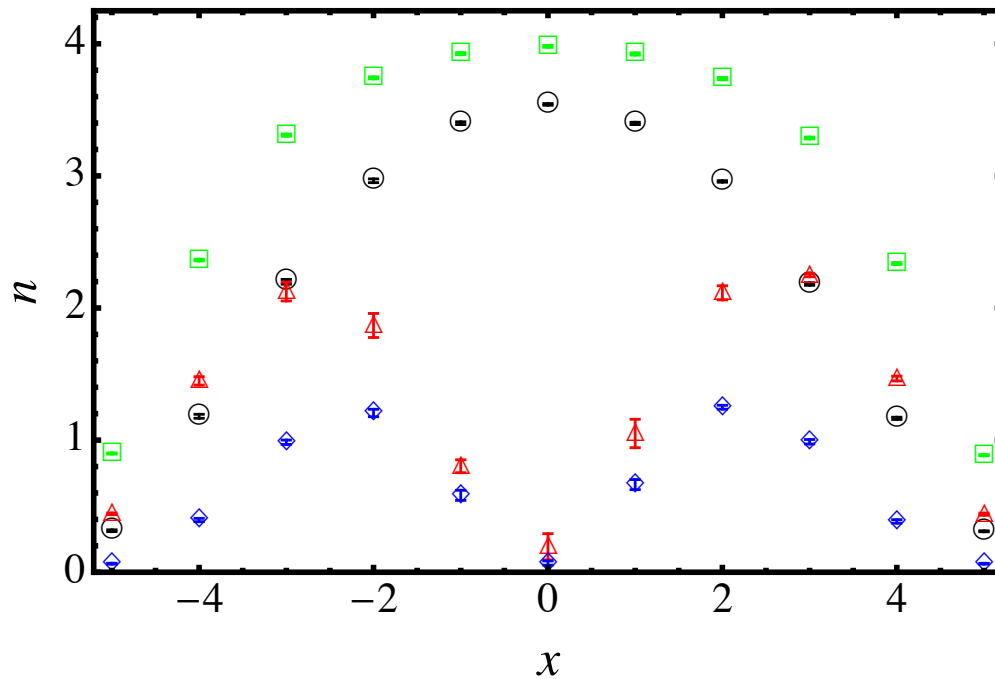


Figure 5.16: Number density n as a function of x at $a^2qB = 0$ (square), 0.08 (circle), 0.2 (triangle) and 0.4 (diamond). All the scales are measured in the unit of the lattice spacing a .

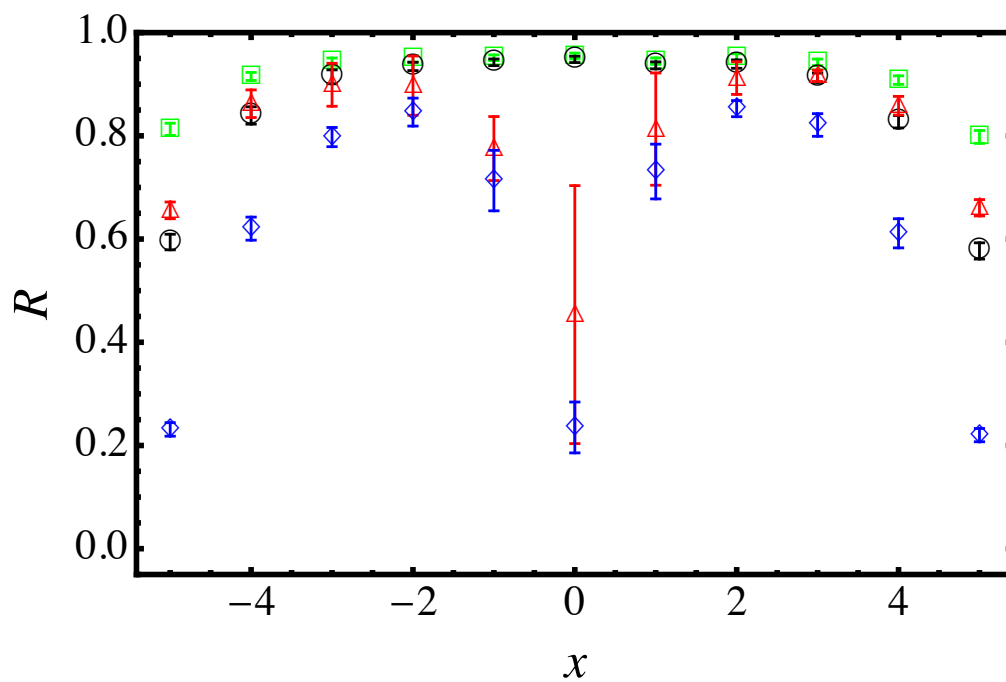


Figure 5.17: Condensate fraction R as a function of x at $a^2qB = 0$ (square), 0.08 (circle), 0.2 (triangle) and 0.4 (diamond). All the scales are measured in the unit of the lattice spacing a .

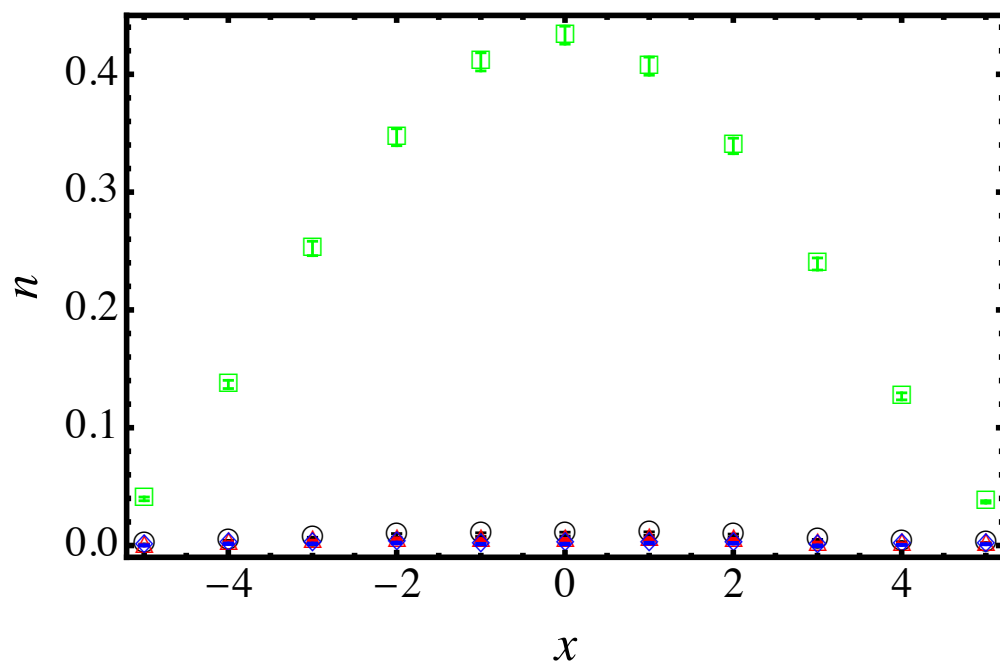


Figure 5.18: Number density n as a function of x at $a^2qB = 0$ (square), 0.08 (circle), 0.2 (triangle) and 0.4 (diamond). All the scales are measured in the unit of the lattice spacing a .

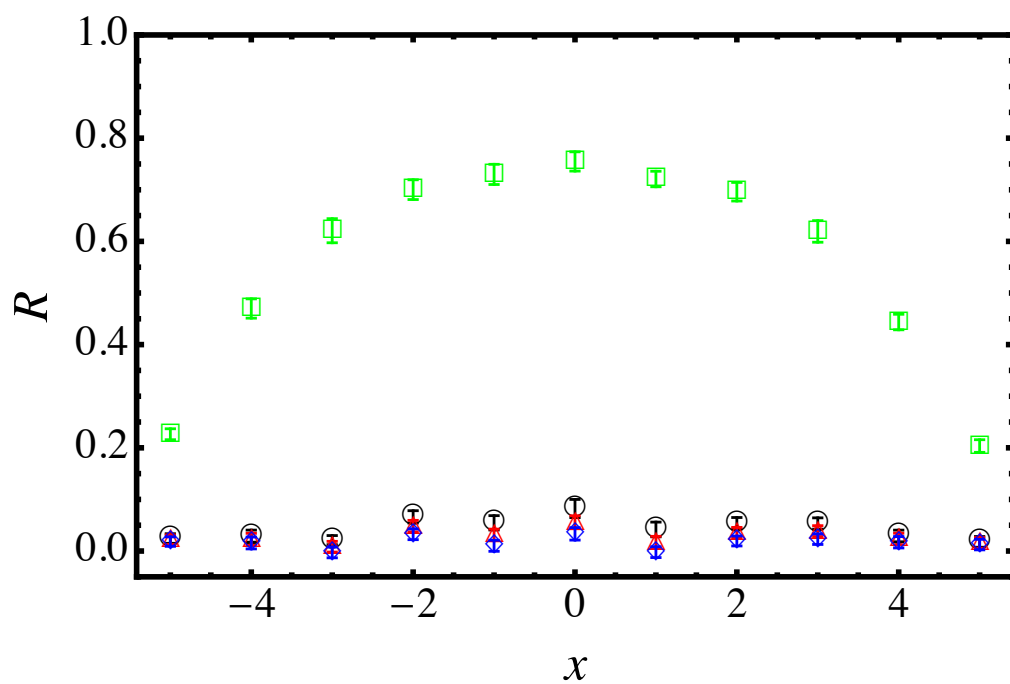


Figure 5.19: Condensate fraction R as a function of x at $a^2qB = 0$ (square), 0.08 (circle), 0.2 (triangle) and 0.4 (diamond). All the scales are measured in the unit of the lattice spacing a .

Chapter 6

Summary and Concluding Remarks

In this thesis, we have performed ab-initio lattice simulations of the nonrelativistic and relativistic Bose-Einstein condensates under strong external fields such as the electric field, the magnetic field, and the rotation. All the lattice actions discussed in this thesis are complex, so that the conventional Monte Carlo method suffers from the notorious sign problem. To overcome this difficulty, we have adopted the complex Langevin method, which can take into account quantum fluctuations exactly even for such complex actions. The complex Langevin method has been previously developed in relativistic field theories to attack complex action problems such as nonequilibrium systems and the phase diagram at finite quark number density.

In particular, we have performed the ab-initio simulation of the quantum vortex nucleation in the rotating Bose-Einstein condensate. In dilute and low temperature systems, the Bose-Einstein condensate is remarkably well described by the mean field theory and the Gross-Pitaevskii equation, where the vortex is quantized due to the single-valuedness of the macroscopic wave function of the Bose-Einstein condensate. When quantum or thermal fluctuation becomes large, it is highly nontrivial how such quantized vortex behaves. For example, the flux quantization does not occur in the presence of strong quantum fluctuation. Around the critical values of temperature, chemical potential, magnetic field, or angular velocity, the fluctuation grows and then the mean-field description necessarily breaks down. This is the reason why the ab-initio simulations are necessary as discussed in this thesis. In fact, we have shown that the flux quantization breaks down when the chemical potential is getting close to its critical value.

In Chap. 2, we have reviewed the formulation of quantum field theories on the lattice. The partition function in the grand canonical ensemble can be represented by the path integral over field variables on the lattice. We have also reviewed how to discuss the spontaneous symmetry breaking in practical simulations. The order parameter always vanishes in finite systems unless the symmetry is explicitly broken. Thus, we have introduced an alternate way to analyze the spontaneous symmetry breaking, that is, observing the off-diagonal long-range order. We have also shown that the Bose-Einstein condensate implies the spontaneous $U(1)$ symmetry breaking.

In Chap. 3, we have reviewed the stochastic quantization formalism, which was originally proposed by Parisi and Wu in 1981. We have also shown the general relation between the

stochastic and path integral formalisms from which we understand that the Langevin method can exactly reproduce the standard Monte Carlo simulation. Then, we have summarized the basis to perform the complex Langevin simulation in which the quantization procedure in the stochastic quantization formalism is numerically performed on the lattice. As an example, we have presented our original work in which we have applied the complex Langevin method to the nonrelativistic Bose system interacting by a repulsive contact interaction. The Silver Blaze problem was correctly managed in our numerical simulation. Also, we have analyzed the spontaneous $U(1)$ symmetry breaking by performing the long-range order analysis.

In Chap. 4, we have performed ab-initio simulations of the nonrelativistic Bose-Einstein condensate under strong external field such as the electric field, the magnetic field, and the rotation. First, we have discussed how to apply such external fields on the lattice. To maintain the local $U(1)$ symmetry on the lattice, we have improved the lattice action by adding higher order terms in terms of the lattice spacing.

Then, we have analyzed the Bose-Einstein condensate in the presence of the Minkowski electric field. We have shown that the non-uniform charge distribution is generated according to the vector potential. We have also analyzed the associated $U(1)$ symmetry breaking by performing the long-range order analysis.

Next, we have analyzed the Bose-Einstein condensate in the presence of the magnetic field. We have shown that the Bose-Einstein condensate for interacting theory is destroyed by the magnetic field due to the formation of Landau levels. Furthermore, we have analyzed the quantum vortex nucleation by the magnetic field. The direct evidence of quantum vortex nucleation is the quantization of circulation: We have shown that the circulation is quantized far from the critical chemical potential, but it is not just above the critical chemical potential. We have clarified that the flux quantization in the Bose-Einstein condensate is blurred by the quantum fluctuation as the chemical potential is getting close to its critical value.

Finally, we have analyzed the Bose-Einstein condensate under the rotation. We have formulated the rotating lattice by using the effective magnetic field induced by the rotation. We have successfully simulated the quantum vortex nucleation in the rotating Bose-Einstein condensate. In our simulations, the quantum fluctuation of vortex numbers is observed, while the averaged circulation is clearly quantized. We have revealed that the fluctuation of vortex numbers behaves as Gaussian and, as a result of cancellation, the average circulation becomes exact integer.

In Chap. 5, we have applied our analysis to the relativistic Bose-Einstein condensate under strong electromagnetic fields. The Silver Blaze problem is resolved by the complex Langevin method also in the relativistic case. We have analyzed the spontaneous $U(1)$ symmetry breaking by performing the long-range order analysis, which was not discussed in previous literature.

Then, we have analyzed the Bose-Einstein condensate in the presence of the electric field. In contrast to the nonrelativistic theories, the pair creation of a particle and an anti-particle can occur in the vacuum via the Schwinger mechanism in relativistic theories. We have performed,

by using the complex Langevin method, the first ab-initio simulation of the particle production in the system, where the sign problem occurs. We have shown that the non-uniform charge distribution is generated according to the vector potential. We have also analyzed the associated U(1) symmetry breaking by performing the long-range order analysis.

Finally, we have analyzed the relativistic Bose-Einstein condensate in the presence of the magnetic field. We have numerically shown, as in the case of the nonrelativistic theory, that the Bose-Einstein condensate is destroyed by the magnetic field due to the formation of Landau levels. We have also analyzed the relativistic quantum vortex nucleation by the magnetic field. We have shown that the circulation is clearly quantized in the superconducting phase far from the critical chemical potential, but it is blurred by quantum fluctuation as the chemical potential or the magnetic field is getting close to its critical value. We have clarified that near the critical values of chemical potential or magnetic field, the fluctuation of vortex numbers shows a broad Gaussian distribution, while it becomes almost a single peak far from the critical value.

There are several future applications of the complex Langevin method to condensed matter systems. First, nonperturbative simulations at finite temperatures are interesting. We can estimate the critical temperature of Bose-Einstein condensation with including all orders of density corrections [119, 120, 121, 122]. We can also study the effect of thermal fluctuations to the Bose-Einstein condensate and the breakdown of the Gross-Pitaevskii equation. Furthermore, our approach is applicable to the Bose-Hubbard model, which describes Bose system on an optical lattice [123] and is known to suffer from the sign problem [106]. The application of the complex Langevin method to the nonrelativistic fermion system is an important future problem.

The complex Langevin method will also be useful in relativistic Bose systems under rotation, where the rotation causes the sign problem as well the chemical potential does [124]. Nonperturbative study of the quantum vortex nucleation in relativistic systems is helpful to understand the physics of e.g., cosmic string in the early universe [56]. However, as remarked in Sec. 4.4.1, the formulation of rotating lattice in the relativistic field theories has some difficulties e.g., the problem of renormalization. We defer these challenging issues to future works.

Acknowledgments

First, I would like to express the greatest appreciation to my supervisor Prof. Tetsuo Hatsuda for stimulating discussions, valuable comments, and careful reading of the whole manuscript. I am also grateful to Dr. Arata Yamamoto for useful discussions and collaborations on subjects covered in this thesis. I acknowledge Prof. Kenji Fukushima, Dr. Takumi Doi, Dr. Yoshimasa Hidaka and Prof. Yuji Tachikawa for helpful discussions and comments. I also acknowledge all members of the quantum hadron physics laboratory in the RIKEN Nishina center for accelerator based science.

Appendix A

Higher order algorithm

Here, we review the higher order algorithm [107, 108]. We show, by using a toy model, that it removes the linear order step size dependence, which appears in the lowest order algorithm. In the higher order algorithm, instead of directly solving the lowest order Eqs. (3.26) and (3.27), we numerically solve following equations:

$$\varphi_{\tau,\mathbf{x}}^{(1)aR}(n) = \varphi_{\tau,\mathbf{x}}^{aR}(n) - \frac{1}{2}\varepsilon\text{Re} \left[\frac{\partial S_{\text{lat}}}{\partial \varphi_{\tau,\mathbf{x}}^a} \right] (\varphi_{\tau,\mathbf{x}}), \quad (\text{A.1})$$

$$\varphi_{\tau,\mathbf{x}}^{(1)aI}(n) = \varphi_{\tau,\mathbf{x}}^{aI}(n) - \frac{1}{2}\varepsilon\text{Im} \left[\frac{\partial S_{\text{lat}}}{\partial \varphi_{\tau,\mathbf{x}}^a} \right] (\varphi_{\tau,\mathbf{x}}), \quad (\text{A.2})$$

$$\varphi_{\tau,\mathbf{x}}^{(2)aR}(n) = \varphi_{\tau,\mathbf{x}}^{aR}(n) - \frac{1}{2}\varepsilon\text{Re} \left[\frac{\partial S_{\text{lat}}}{\partial \varphi_{\tau,\mathbf{x}}^a} \right] (\varphi_{\tau,\mathbf{x}}) + \frac{3}{2}\sqrt{\varepsilon}\tilde{\eta}_{\tau,\mathbf{x}}^a(n), \quad (\text{A.3})$$

$$\varphi_{\tau,\mathbf{x}}^{(2)aI}(n) = \varphi_{\tau,\mathbf{x}}^{aI}(n) - \frac{1}{2}\varepsilon\text{Im} \left[\frac{\partial S_{\text{lat}}}{\partial \varphi_{\tau,\mathbf{x}}^a} \right] (\varphi_{\tau,\mathbf{x}}), \quad (\text{A.4})$$

$$\begin{aligned} \varphi_{\tau,\mathbf{x}}^{aR}(n+1) &= \varphi_{\tau,\mathbf{x}}^{aR}(n) - \frac{1}{3}\varepsilon\text{Re} \left[\frac{\partial S_{\text{lat}}}{\partial \varphi_{\tau,\mathbf{x}}^a} \right] (\varphi_{\tau,\mathbf{x}}^{(0)}) \\ &\quad - \frac{2}{3}\varepsilon\text{Re} \left[\frac{\partial S_{\text{lat}}}{\partial \varphi_{\tau,\mathbf{x}}^a} \right] (\varphi_{\tau,\mathbf{x}}^{(1)}) + \sqrt{\varepsilon}\eta_{\tau,\mathbf{x}}^a(n), \end{aligned} \quad (\text{A.5})$$

$$\begin{aligned} \varphi_{\tau,\mathbf{x}}^{aI}(n+1) &= \varphi_{\tau,\mathbf{x}}^{aI}(n) - \frac{1}{3}\varepsilon\text{Im} \left[\frac{\partial S_{\text{lat}}}{\partial \varphi_{\tau,\mathbf{x}}^a} \right] (\varphi_{\tau,\mathbf{x}}^{(0)}) \\ &\quad - \frac{2}{3}\varepsilon\text{Im} \left[\frac{\partial S_{\text{lat}}}{\partial \varphi_{\tau,\mathbf{x}}^a} \right] (\varphi_{\tau,\mathbf{x}}^{(1)}), \end{aligned} \quad (\text{A.6})$$

where $\tilde{\eta}^a$ is defined as $\tilde{\eta}^a = \eta^a/2 + \sqrt{3}\bar{\eta}^a/6$. We introduce auxiliary complex fields $\varphi^{(1)a} = \varphi^{(1)aR} + i\varphi^{(1)aI}$ and $\varphi^{(2)a} = \varphi^{(2)aR} + i\varphi^{(2)aI}$. We also introduce independent Gaussian noises η^a and $\bar{\eta}^a$, which satisfy

$$\langle \eta_x^a(n) \rangle = \langle \bar{\eta}_x^a(n) \rangle = 0, \quad (\text{A.7})$$

$$\langle \eta_x^a(n)\eta_y^b(n') \rangle = \langle \bar{\eta}_x^a(n)\bar{\eta}_y^b(n') \rangle = 2\delta_{ab}\delta_{xy}\delta_{nn'}, \quad (\text{A.8})$$

$$\langle \eta_x^a(n) \bar{\eta}_y^b(n') \rangle = 0. \quad (\text{A.9})$$

$\text{Re} [\partial S_{\text{lat}} / \partial \varphi_{\tau, \mathbf{x}}^a] (\psi_{\tau, \mathbf{x}})$ or $\text{Im} [\partial S_{\text{lat}} / \partial \varphi_{\tau, \mathbf{x}}^a] (\psi_{\tau, \mathbf{x}})$ means that the functional derivative in those equations are evaluated by using the complex field $\psi = \varphi, \varphi^{(1)},$ or $\varphi^{(2)}$.

To see that this algorithm improves the step size dependence, let us consider a two site model, which imitates the temporal hopping term in the nonrelativistic lattice action. The action is

$$\begin{aligned} S &= \varphi_1^2 + \varphi_2^2 + 2i\varphi_1\varphi_2 \\ &= \begin{pmatrix} \varphi_1 & \varphi_2 \end{pmatrix} M \begin{pmatrix} \varphi_1 \\ \varphi_2 \end{pmatrix}, \end{aligned} \quad (\text{A.10})$$

$$M = \begin{pmatrix} 1 & i \\ i & 1 \end{pmatrix}, \quad (\text{A.11})$$

where $\varphi_{i=1,2}$ are real scalar field. Since the matrix M is not hermitian, the action is complex and thus causes the sign problem, namely, the Langevin equations are needed to be complexified. However, since the action is quadratic, we can analytically solve the Langevin equations by diagonalizing the action:

$$S = \begin{pmatrix} \varphi_+ & \varphi_- \end{pmatrix} \begin{pmatrix} \lambda_+ & 0 \\ 0 & \lambda_- \end{pmatrix} \begin{pmatrix} \varphi_+ \\ \varphi_- \end{pmatrix}, \quad (\text{A.12})$$

where $\varphi_{\pm} = \varphi_1 \pm \varphi_2$, and $\lambda_{\pm} = 1 \pm i$. The correlation functions of $\varphi_{1,2}$ are obtained from those of φ_{\pm} by unitary transformation and thus we only calculate the correlation functions of φ_{\pm} . The discretized Langevin equations read

$$\varphi_i(n+1) = \varphi_i(n) - 2\lambda_i\varepsilon\varphi_i(n) + \sqrt{\varepsilon}\eta_i(n), \quad (\text{A.13})$$

where $\varphi_{i=\pm}$ are complex fields and $\eta_{i=\pm}$ are independent real Gaussian noises. We have

$$\varphi_i(n) = \sqrt{\varepsilon} \sum_{m=0}^{n-1} (1 - 2\lambda_i\varepsilon)^{n-1-m} \eta_i(m), \quad (\text{A.14})$$

where we choose $\varphi_i(0) = 0$ as initial conditions. The two point function reads

$$\lim_{n \rightarrow \infty} \langle \varphi_i(n) \varphi_i^*(n) \rangle_{\eta} = \frac{2\varepsilon}{1 - (1 - \lambda_i\varepsilon)^2}. \quad (\text{A.15})$$

Therefore, the correlation function shows the linear step size dependence in the limit of $\varepsilon \rightarrow 0$:

$$\lim_{n \rightarrow \infty} \langle \varphi_i(n) \varphi_i^*(n) \rangle_{\eta} = \frac{1}{\lambda_i} \left(1 + \frac{1}{2} \lambda_i \varepsilon + \mathcal{O}(\varepsilon^2) \right). \quad (\text{A.16})$$

On the other hand, Eqs. (A.1)- (A.6) read

$$\varphi_i^{(1)}(n) = \varphi_i(n) - \frac{1}{2} \varepsilon \lambda_i \varphi_i(n), \quad (\text{A.17})$$

$$\varphi_i^{(2)}(n) = \varphi_i(n) - \frac{1}{2}\varepsilon\lambda_i\varphi_i(n) + \frac{3}{2}\sqrt{\varepsilon}\tilde{\eta}_i(n), \quad (\text{A.18})$$

$$\varphi_i(n+1) = \varphi_i(n) - \frac{1}{3}\varepsilon\lambda_i\left(\varphi_i^{(1)}(n) + 2\varphi_i^{(2)}(n)\right) + \sqrt{\varepsilon}\eta_i(n). \quad (\text{A.19})$$

Then, we have

$$\varphi_i(n+1) = \varphi_i(n) - \varepsilon\tilde{\lambda}_i\varphi_i(n) + \sqrt{\varepsilon}\eta'_i(n), \quad (\text{A.20})$$

where

$$\tilde{\lambda}_i = \lambda_i\left(1 - \frac{1}{2}\varepsilon\lambda_i\right), \quad (\text{A.21})$$

$$\eta'_i(n) = \eta_i(n) - \varepsilon\lambda_i\tilde{\eta}_i(n). \quad (\text{A.22})$$

Since Gaussian noises are additive, $\eta'_i(n)$ are also Gaussian noises, which are no longer real and satisfy

$$\langle\eta'_i(n)\rangle = 0, \quad (\text{A.23})$$

$$\langle\eta'_i(n)\eta'_j(n')\rangle = 2\left(1 - \varepsilon\lambda_i + \frac{1}{3}\varepsilon^2\lambda_i^2\right)\delta_{ij}\delta_{nn'}. \quad (\text{A.24})$$

From Eqs. (A.13) and (A.13), the two point function in the higher order algorithm read

$$\lim_{n\rightarrow\infty}\langle\varphi_i(n)\varphi_i^*(n)\rangle_\eta = \frac{2\varepsilon}{1 - (1 - \tilde{\lambda}_i\varepsilon)^2}\left(1 - \varepsilon\lambda_i + \frac{1}{3}\varepsilon^2\lambda_i^2\right). \quad (\text{A.25})$$

Therefore, the leading step size dependence of the correlation function in the limit of $\varepsilon \rightarrow 0$ is improved as

$$\lim_{n\rightarrow\infty}\langle\varphi_i(n)\varphi_i^*(n)\rangle_\eta = \frac{1}{\lambda_i}\left(1 - \frac{1}{6}\lambda_i^2\varepsilon^2 + \mathcal{O}(\varepsilon^3)\right). \quad (\text{A.26})$$

Appendix B

Jackknife method

Here we summarize the Jackknife method to estimate the statistical errors of ensemble averages [125].

B.1 Standard deviation

Let us consider a set of finite data x_i , $X = \{x_i : x_1, x_2, \dots, x_N\}$, which have the same probability distribution. We are interested in estimating the “error” of their mean value:

$$\bar{x} = \frac{1}{N} \sum_{i=1}^N x_i. \quad (\text{B.1})$$

If x_i are uncorrelated, by assuming the central limit theorem, the standard error of the mean value δx is obtained from the corrected standard deviation of the data s as

$$\begin{aligned} s^2 &= \frac{1}{N-1} \sum_{i=1}^N (x_i - \bar{x})^2 \\ &= \frac{N}{N-1} \left(\frac{1}{N} \sum_{i=1}^N x_i^2 - \bar{x}^2 \right), \end{aligned} \quad (\text{B.2})$$

$$\begin{aligned} \delta x &= \frac{s}{\sqrt{N}} \\ &= \sqrt{\frac{1}{N-1} \left(\frac{1}{N} \sum_{i=1}^N x_i^2 - \bar{x}^2 \right)}. \end{aligned} \quad (\text{B.3})$$

B.2 Jackknife estimation

In the jackknife method, the statistical errors are estimated by dividing $\{x_i\}$ into small subsets. We decompose $\{x_i\}$ into $N_m = N/m$ bins and thus each bin has m data. Let us define $X^{k=1, \dots, N_m}$ as

$$X^k = \{x_i^k : x_1, \dots, x_{(k-1)m}, x_{(k+1)m}, \dots, x_N\}. \quad (\text{B.4})$$

The subsets X^k are obtained from X by removing the data decomposed into the k th bin. The mean value in X^k is

$$\bar{x}^k = \frac{1}{N-m} \sum_{i \in X^k} x_i. \quad (\text{B.5})$$

Now, we have a data set $\tilde{X} = \{\bar{x}^i : \bar{x}^1, \dots, \bar{x}^{N_M}\}$. We use $\langle \cdot \rangle$ as the average over \tilde{X} . Then, we can calculate the mean value of the whole data as

$$\langle \bar{x} \rangle = \frac{1}{N_m} \sum_k \bar{x}^k, \quad (\text{B.6})$$

which recovers Eq. (B.1) as follows

$$\begin{aligned} \langle \bar{x} \rangle &= \frac{1}{N_m} \sum_k \bar{x}^k \\ &= \frac{1}{N_m} \sum_k \frac{1}{N-m} \sum_{i \in X^k} x_i \\ &= \frac{1}{N_m} \frac{1}{N-m} \sum_{i \in X} (N_m - 1) x_i \\ &= \frac{1}{N} \sum_{i=1}^N x_i. \end{aligned} \quad (\text{B.7})$$

The statistical error in the m -th bin jackknife method, δx_m , is estimated from the uncorrected standard deviation of \tilde{X} , s_m , as

$$\begin{aligned} s_m^2 &= \langle (\bar{x} - \langle \bar{x} \rangle)^2 \rangle \\ &= \frac{1}{N_m} \sum_{k=1}^{N_m} (\bar{x}^k - \bar{x})^2 \\ &= \frac{1}{N_m} \sum_{k=1}^{N_m} (\bar{x}^k)^2 - \bar{x}^2, \end{aligned} \quad (\text{B.8})$$

$$\delta x_m = \sqrt{(N_m - 1) s_m}. \quad (\text{B.9})$$

When we choose $m = 1$, Eq. (B.9) recovers the statistical error obtained from the corrected standard deviation (B.3) as follows. Eq. (B.8) reads

$$\begin{aligned} s_1^2 &= \frac{1}{N} \sum_{k=1}^N (\bar{x}^k - \bar{x})^2 \\ &= \frac{1}{N} \sum_{k=1}^N \left(\frac{1}{N-1} \sum_{i \neq k} x_i - \bar{x} \right)^2 \\ &= \frac{1}{N} \sum_{k=1}^N \left(\frac{N}{N-1} \left(\bar{x} - \frac{x_k}{N} \right) - \bar{x} \right)^2 \\ &= \frac{1}{N(N-1)} s^2. \end{aligned} \quad (\text{B.10})$$

Therefore, δx_1 apparently satisfies

$$\begin{aligned}\delta x_1 &= \sqrt{N-1} s_1 \\ &= \delta x.\end{aligned}\tag{B.11}$$

By changing the bin size m , we can estimate the autocorrelation between data taken from Langevin trajectories. If the data are uncorrelated, the estimated error s_m are independent of m , and thus by observing the bin size dependence of errors, we can determine how many times we should iterate the Langevin process before we take next field configurations. In all simulations performed in this thesis, we have taken sufficiently large Langevin time step to generate the ensemble, so that the statistical errors of expectation values do not depend on the bin size m .

References

- [1] P. L. Kapitza, “Viscosity of Liquid Helium below the λ -Point,” *Nature*, vol. 141, pp. 74–75, 1938.
- [2] J. F. Allen and A. D. Misener, “Flow Phenomena in Liquid Helium II,” *Nature*, vol. 142, pp. 643–644, 1938.
- [3] D. D. Osheroff, R. C. Richardson, and D. M. Lee, “Evidence for a New Phase of Solid He^3 ,” *Phys. Rev. Lett.*, vol. 28, pp. 885–888, 1972.
- [4] S. Balibar, H. Alles, and A. Y. Parshin, “The surface of helium crystals,” *Rev. Mod. Phys.*, vol. 77, pp. 317–370, 2005.
- [5] M. H. Anderson, J. R. Ensher, M. R. Matthews, C. E. Wieman, and E. A. Cornell, “Observation of Bose-Einstein Condensation in a Dilute Atomic Vapor,” *Science*, vol. 269, pp. 198–201, 1995.
- [6] C. C. Bradley, C. A. Sackett, J. J. Tollett, and R. G. Hulet, “Evidence of Bose-Einstein Condensation in an Atomic Gas with Attractive Interactions,” *Phys. Rev. Lett.*, vol. 75, pp. 1687–1690, 1995.
- [7] K. B. Davis, M.-O. Mewes, M. R. Andrews, N. J. van Druten, D. S. Durfee, D. M. Kurn, and W. Ketterle, “Bose-Einstein Condensation in a Gas of Sodium Atoms,” *Phys. Rev. Lett.*, vol. 75, pp. 3969–3973, 1995.
- [8] I. Bloch, J. Dalibard, and W. Zwerger, “Many-body physics with ultracold gases,” *Rev. Mod. Phys.*, vol. 80, pp. 885–964, 2008.
- [9] C. Varma, “High-temperature superconductivity: Mind the pseudogap,” *Nature*, vol. 468, pp. 184–185, 2010.
- [10] K. Fukushima and T. Hatsuda, “The phase diagram of dense QCD,” *Rept. Prog. Phys.*, vol. 74, p. 014001, 2011.
- [11] J. Bardeen, L. N. Cooper, and J. R. Schrieffer, “Theory of superconductivity,” *Phys. Rev.*, vol. 108, pp. 1175–1204, 1957.

- [12] J. G. Bednorz and K. A. Müller, “Possible High T_c Superconductivity in the Ba-La-Cu-O System,” *Zeitschrift für Physik B Condensed Matter*, vol. 64, no. 2, pp. 189–193, 1986.
- [13] D. Jérôme, A. Mazaud, M. Ribault, and K. Bechgaard, “Superconductivity in a synthetic organic conductor (TMTSF)₂PF₆,” *J. Physique Lett.*, vol. 41, no. 4, pp. 95–98, 1980.
- [14] Y. Kamihara, H. Hiramatsu, M. Hirano, R. Kawamura, H. Yanagi, T. Kamiya, and H. Hosono, “Iron-Based Layered Superconductor: LaOFeP,” *J. Am. Chem. Soc.*, vol. 128, no. 31, pp. 10012–10013, 2006.
- [15] J. Blatt, K. Böer, and W. Brandt, “Bose-Einstein Condensation of Excitons,” *Phys. Rev.*, vol. 126, pp. 1691–1692, 1962.
- [16] J. Kasprzak, M. Richard, S. Kundermann, A. Baas, P. Jeambrun, J. M. J. Keeling, F. M. Marchetti, M. H. Szymanska, R. Andre, J. L. Staehli, V. Savona, P. B. Littlewood, B. Deveaud, and L. S. Dang, “Bose-Einstein condensation of exciton polaritons,” *Nature*, vol. 443, pp. 409–414, 2006.
- [17] H. Deng, H. Haug, and Y. Yamamoto, “Exciton-polariton Bose-Einstein condensation,” *Rev. Mod. Phys.*, vol. 82, pp. 1489–1537, 2010.
- [18] T. Nikuni, M. Oshikawa, A. Oosawa, and H. Tanaka, “Bose-Einstein Condensation of Dilute Magnons in TlCuCl₃,” *Phys. Rev. Lett.*, vol. 84, pp. 5868–5871, 2000.
- [19] S. O. Demokritov, V. E. Demidov, O. Dzyapko, G. A. Melkov, A. A. Serga, B. Hillebrands, and A. N. Slavin, “Bose-Einstein condensation of quasi-equilibrium magnons at room temperature under pumping,” *Nature*, vol. 443, pp. 430–433, 2006.
- [20] A. B. Migdal, “Pion Fields in Nuclear Matter,” *Rev. Mod. Phys.*, vol. 50, pp. 107–172, 1978.
- [21] M. G. Alford, A. Schmitt, K. Rajagopal, and T. Schäfer, “Color superconductivity in dense quark matter,” *Rev. Mod. Phys.*, vol. 80, pp. 1455–1515, 2008.
- [22] M. Eto, Y. Hirono, M. Nitta, and S. Yasui, “Vortices and Other Topological Solitons in Dense Quark Matter,” *PTEP*, vol. 2014, no. 1, p. 012D01, 2014.
- [23] G. Baym, C. Pethick, and D. Pines, “Superfluidity in Neutron Stars,” *Nature*, vol. 224, pp. 673–674, 1969.
- [24] M. Hoffberg, A. Glassgold, R. Richardson, and M. Ruderman, “Anisotropic Superfluidity in Neutron Star Matter,” *Phys. Rev. Lett.*, vol. 24, pp. 775–777, 1970.

- [25] T. Takatsuka and R. Tamagaki, “Superfluidity in neutron star matter and symmetric nuclear matter,” *Prog. Theor. Phys. Suppl.*, vol. 112, pp. 27–66, 1993.
- [26] M. G. Alford, K. Rajagopal, and F. Wilczek, “QCD at finite baryon density: Nucleon droplets and color superconductivity,” *Phys. Lett. B*, vol. 422, pp. 247–256, 1998.
- [27] J. Berges and K. Rajagopal, “Color superconductivity and chiral symmetry restoration at nonzero baryon density and temperature,” *Nucl. Phys. B*, vol. 538, pp. 215–232, 1999.
- [28] D. Son, “Superconductivity by long range color magnetic interaction in high density quark matter,” *Phys. Rev. D*, vol. 59, p. 094019, 1999.
- [29] M. G. Alford, J. Berges, and K. Rajagopal, “Unlocking color and flavor in superconducting strange quark matter,” *Nucl. Phys. B*, vol. 558, pp. 219–242, 1999.
- [30] M. G. Alford, J. A. Bowers, and K. Rajagopal, “Crystalline color superconductivity,” *Phys. Rev. D*, vol. 63, p. 074016, 2001.
- [31] M. Alford and K. Rajagopal, “Absence of two flavor color superconductivity in compact stars,” *JHEP*, vol. 0206, p. 031, 2002.
- [32] F. Englert and R. Brout, “Broken Symmetry and the Mass of Gauge Vector Mesons,” *Phys. Rev. Lett.*, vol. 13, pp. 321–323, 1964.
- [33] P. W. Higgs, “Broken Symmetries and the Masses of Gauge Bosons,” *Phys. Rev. Lett.*, vol. 13, pp. 508–509, 1964.
- [34] G. S. Guralnik, C. R. Hagen, and T. W. B. Kibble, “Global Conservation Laws and Massless Particles,” *Phys. Rev. Lett.*, vol. 13, pp. 585–587, 1964.
- [35] G. Aad *et al.*, “Observation of a new particle in the search for the Standard Model Higgs boson with the ATLAS detector at the LHC,” *Phys. Lett. B*, vol. 716, pp. 1–29, 2012.
- [36] S. Chatrchyan *et al.*, “Observation of a new boson at a mass of 125 GeV with the CMS experiment at the LHC,” *Phys. Lett. B*, vol. 716, pp. 30–61, 2012.
- [37] A. Abrikosov, “On the Magnetic properties of superconductors of the second group,” *Sov. Phys. JETP*, vol. 5, pp. 1174–1182, 1957.
- [38] W. H. Kleiner, L. M. Roth, and S. H. Autler, “Bulk Solution of Ginzburg-Landau Equations for Type II Superconductors: Upper Critical Field Region,” *Phys. Rev.*, vol. 133, pp. 1226–1227, 1964.
- [39] U. Essmann and H. Träuble, “The direct observation of individual flux lines in type II superconductors,” *Phys. Lett. A*, vol. 24, no. 10, pp. 526 – 527, 1967.

- [40] H. F. Hess, R. B. Robinson, R. C. Dynes, J. M. Valles, and J. V. Waszczak, “Scanning-Tunneling-Microscope Observation of the Abrikosov Flux Lattice and the Density of States near and inside a Fluxoid,” *Phys. Rev. Lett.*, vol. 62, pp. 214–216, 1989.
- [41] M. R. Matthews, B. P. Anderson, P. C. Haljan, D. S. Hall, C. E. Wieman, and E. A. Cornell, “Vortices in a Bose-Einstein Condensate,” *Phys. Rev. Lett.*, vol. 83, pp. 2498–2501, 1999.
- [42] K. W. Madison, F. Chevy, W. Wohlleben, and J. Dalibard, “Vortex Formation in a Stirred Bose-Einstein Condensate,” *Phys. Rev. Lett.*, vol. 84, pp. 806–809, 2000.
- [43] J. R. Abo-Shaeer, C. Raman, J. M. Vogels, and W. Ketterle, “Observation of Vortex Lattices in Bose-Einstein Condensates,” *Science*, vol. 292, no. 5516, pp. 476–479, 2001.
- [44] K. W. Madison, F. Chevy, V. Bretin, and J. Dalibard, “Stationary States of a Rotating Bose-Einstein Condensate: Routes to Vortex Nucleation,” *Phys. Rev. Lett.*, vol. 86, pp. 4443–4446, 2001.
- [45] S. Donadello, S. Serafini, M. Tylutki, L. P. Pitaevskii, F. Dalfovo, G. Lamporesi, and G. Ferrari, “Observation of Solitonic Vortices in Bose-Einstein Condensates,” *Phys. Rev. Lett.*, vol. 113, p. 065302, 2014.
- [46] A. L. Fetter, “Rotating trapped Bose-Einstein condensates,” *Rev. Mod. Phys.*, vol. 81, pp. 647–691, 2009.
- [47] E. Hubble, “A Relation between Distance and Radial Velocity among Extra-Galactic Nebulae,” *Proc. Natl. Acad. Sci.*, vol. 15, pp. 168–173, 1929.
- [48] R. A. Alpher, H. Bethe, and G. Gamow, “The Origin of Chemical Elements,” *Phys. Rev.*, vol. 73, pp. 803–804, 1948.
- [49] G. Gamow, “Expanding Universe and the Origin of Elements,” *Phys. Rev.*, vol. 70, pp. 572–573, 1946.
- [50] K. Sato, “First-order phase transition of a vacuum and the expansion of the Universe,” *Mon. Not. Roy. Astron. Soc.*, vol. 195, no. 3, pp. 467–479, 1981.
- [51] A. H. Guth, “The Inflationary Universe: A Possible Solution to the Horizon and Flatness Problems,” *Phys. Rev. D*, vol. 23, pp. 347–356, 1981.
- [52] A. D. Linde, “A New Inflationary Universe Scenario: A Possible Solution of the Horizon, Flatness, Homogeneity, Isotropy and Primordial Monopole Problems,” *Phys. Lett. B*, vol. 108, pp. 389–393, 1982.

- [53] A. Albrecht and P. J. Steinhardt, “Cosmology for Grand Unified Theories with Radiatively Induced Symmetry Breaking,” *Phys. Rev. Lett.*, vol. 48, pp. 1220–1223, 1982.
- [54] B. Ratra and P. J. E. Peebles, “Cosmological Consequences of a Rolling Homogeneous Scalar Field,” *Phys. Rev. D*, vol. 37, p. 3406, 1988.
- [55] P. J. E. Peebles and B. Ratra, “The Cosmological constant and dark energy,” *Rev. Mod. Phys.*, vol. 75, pp. 559–606, 2003.
- [56] T. W. B. Kibble, “Topology of Cosmic Domains and Strings,” *J. Phys. A*, vol. 9, pp. 1387–1398, 1976.
- [57] G. 't Hooft, “Magnetic Monopoles in Unified Gauge Theories,” *Nucl. Phys. B*, vol. 79, pp. 276–284, 1974.
- [58] A. Vilenkin, “Cosmic Strings and Domain Walls,” *Phys. Rept.*, vol. 121, pp. 263–315, 1985.
- [59] M. B. Hindmarsh and T. W. B. Kibble, “Cosmic strings,” *Rept. Prog. Phys.*, vol. 58, pp. 477–562, 1995.
- [60] A. A. Penzias and R. W. Wilson, “A Measurement of excess antenna temperature at 4080-Mc/s,” *Astrophys. J.*, vol. 142, pp. 419–421, 1965.
- [61] G. F. Smoot *et al.*, “Structure in the COBE differential microwave radiometer first-year maps,” *Astrophys. J.*, vol. 396, pp. L1–L5, 1992.
- [62] S. Hanany, P. Ade, A. Balbi, J. Bock, J. Borrill, *et al.*, “MAXIMA-1: A Measurement of the cosmic microwave background anisotropy on angular scales of $10' - 5^\circ$,” *Astrophys. J.*, vol. 545, p. L5, 2000.
- [63] D. N. Spergel *et al.*, “First year Wilkinson Microwave Anisotropy Probe (WMAP) observations: Determination of cosmological parameters,” *Astrophys. J. Suppl.*, vol. 148, pp. 175–194, 2003.
- [64] C. L. Bennett *et al.*, “First year Wilkinson Microwave Anisotropy Probe (WMAP) observations: Preliminary maps and basic results,” *Astrophys. J. Suppl.*, vol. 148, pp. 1–27, 2003.
- [65] P. A. R. Ade *et al.*, “Planck 2013 results. XVI. Cosmological parameters,” *Astron. Astrophys.*, vol. 571, p. A16, 2014.
- [66] E. P. Gross, “Structure of a quantized vortex in boson systems,” *Il Nuovo Cimento Series 10*, vol. 20, no. 3, pp. 454–477, 1961.

- [67] L. P. Pitaevskii, “VORTEX LINES IN AN IMPERFECT BOSE GAS,” *Sov. Phys. JETP-USSR*, vol. 13, no. 2, 1961.
- [68] M. Tsubota, K. Kasamatsu, and M. Ueda, “Vortex lattice formation in a rotating Bose-Einstein condensate,” *Phys. Rev. A*, vol. 65, p. 023603, 2002.
- [69] N. R. Cooper, N. K. Wilkin, and J. M. F. Gunn, “Quantum Phases of Vortices in Rotating Bose-Einstein Condensates,” *Phys. Rev. Lett.*, vol. 87, p. 120405, 2001.
- [70] J. Sinova, C. B. Hanna, and A. H. MacDonald, “Quantum Melting and Absence of Bose-Einstein Condensation in Two-Dimensional Vortex Matter,” *Phys. Rev. Lett.*, vol. 89, p. 030403, 2002.
- [71] T. Hayata and A. Yamamoto, “Complex Langevin simulation of quantum vortex nucleation in the Bose-Einstein condensate,” *in preparation*, 2014.
- [72] J. B. Kogut, “An Introduction to Lattice Gauge Theory and Spin Systems,” *Rev. Mod. Phys.*, vol. 51, p. 659, 1979.
- [73] G. S. Bali, “QCD forces and heavy quark bound states,” *Phys. Rept.*, vol. 343, pp. 1–136, 2001.
- [74] A. Bazavov, D. Toussaint, C. Bernard, J. Laiho, C. DeTar, *et al.*, “Nonperturbative QCD simulations with 2+1 flavors of improved staggered quarks,” *Rev. Mod. Phys.*, vol. 82, pp. 1349–1417, 2010.
- [75] v. d. L. Wolfgang, “A quantum Monte Carlo approach to many-body physics,” *Phys. Rep.*, vol. 220, no. 23, pp. 53 – 162, 1992.
- [76] N. Kawashima and K. Harada, “Recent Developments of World-Line Monte Carlo Methods,” *J. Phys. Soc. Jpn*, vol. 73, p. 1379, 2004.
- [77] L. Pollet, “Recent developments in quantum Monte Carlo simulations with applications for cold gases,” *Rep. Prog. Phys.*, vol. 75, no. 9, p. 094501, 2012.
- [78] N. Metropolis, A. W. Rosenbluth, M. N. Rosenbluth, A. H. Teller, and E. Teller, “Equation of State Calculations by Fast Computing Machines,” *J. Chem. Phys.*, vol. 21, no. 6, pp. 1087–1092, 1953.
- [79] G. G. Batrouni, G. R. Katz, A. S. Kronfeld, G. P. Lepage, B. Svetitsky, and K. G. Wilson, “Langevin simulations of lattice field theories,” *Phys. Rev. D*, vol. 32, pp. 2736–2747, 1985.
- [80] S. Duane, A. D. Kennedy, B. J. Pendleton, and D. Roweth, “Hybrid Monte Carlo,” *Phys. Lett. B*, vol. 195, pp. 216–222, 1987.

- [81] J. Berges and I.-O. Stamatescu, “Simulating nonequilibrium quantum fields with stochastic quantization techniques,” *Phys. Rev. Lett.*, vol. 95, p. 202003, 2005.
- [82] J. Berges, S. Borsanyi, D. Sexty, and I.-O. Stamatescu, “Lattice simulations of real-time quantum fields,” *Phys. Rev. D*, vol. 75, p. 045007, 2007.
- [83] K. Fukushima and T. Hayata, “Schwinger Mechanism with Stochastic Quantization,” *Phys. Lett. B*, vol. 735, pp. 371–375, 2014.
- [84] F. Karsch and H. W. Wyld, “Complex Langevin Simulation of the SU(3) Spin Model With Nonzero Chemical Potential,” *Phys. Rev. Lett.*, vol. 55, p. 2242, 1985.
- [85] J. Ambjorn, M. Flensburg, and C. Peterson, “The Complex Langevin Equation and Monte Carlo Simulations of Actions With Static Charges,” *Nucl. Phys. B*, vol. 275, p. 375, 1986.
- [86] G. Aarts and I.-O. Stamatescu, “Stochastic quantization at finite chemical potential,” *JHEP*, vol. 0809, p. 018, 2008.
- [87] G. Aarts, “Can stochastic quantization evade the sign problem? The relativistic Bose gas at finite chemical potential,” *Phys. Rev. Lett.*, vol. 102, p. 131601, 2009.
- [88] D. Sexty, “Simulating full QCD at nonzero density using the complex Langevin equation,” *Phys. Lett. B*, vol. 729, pp. 108–111, 2014.
- [89] G. Aarts, “Complex Langevin dynamics and other approaches at finite chemical potential,” *PoS LATTICE2012*, p. 017, 2012.
- [90] P. Hasenfratz and F. Karsch, “Chemical Potential on the Lattice,” *Phys. Lett. B*, vol. 125, p. 308, 1983.
- [91] J.-W. Chen and D. B. Kaplan, “A Lattice theory for low-energy fermions at finite chemical potential,” *Phys. Rev. Lett.*, vol. 92, p. 257002, 2004.
- [92] M. D’Elia, “Lattice QCD Simulations in External Background Fields,” *Lect. Notes Phys.*, vol. 871, pp. 181–208, 2013.
- [93] T. Koma and H. Tasaki, “Symmetry breaking and finite-size effects in quantum many-body systems,” *J. Stat. Phys.*, vol. 76, pp. 745–803, 1994.
- [94] C. N. Yang, “Concept of Off-Diagonal Long-Range Order and the Quantum Phases of Liquid He and of Superconductors,” *Rev. Mod. Phys.*, vol. 34, pp. 694–704, 1962.
- [95] E. H. Wichmann and J. H. Crichton, “Cluster Decomposition Properties of the S Matrix,” *Phys. Rev.*, vol. 132, pp. 2788–2799, 1963.

- [96] S. Weinberg, “What is quantum field theory, and what did we think it is?,” 1996.
- [97] G. Parisi and Y.-s. Wu, “Perturbation Theory Without Gauge Fixing,” *Sci. Sin.*, vol. 24, p. 483, 1981.
- [98] G. Parisi, “On Complex Probabilities,” *Phys. Lett. B*, vol. 131, pp. 393–395, 1983.
- [99] P. H. Damgaard and H. Huffel, “Stochastic Quantization,” *Phys. Rept.*, vol. 152, p. 227, 1987.
- [100] M. Namiki, “Basic ideas of stochastic quantization,” *Prog. Theor. Phys. Suppl.*, vol. 111, pp. 1–41, 1993.
- [101] T. D. Cohen, “Functional integrals for QCD at nonzero chemical potential and zero density,” *Phys. Rev. Lett.*, vol. 91, p. 222001, 2003.
- [102] J. Ambjørn and S.-K. Yang, “Numerical problems in applying the Langevin equation to complex effective actions,” *Phys. Lett. B*, vol. 165, no. 13, pp. 140 – 146, 1985.
- [103] J. R. Klauder and W. P. Petersen, “Spectrum of certain non-self-adjoint operators and solutions of Langevin equations with complex drift,” *J. Stat. Phys.*, vol. 39, no. 1-2, pp. 53–72, 1985.
- [104] G. Aarts, E. Seiler, and I.-O. Stamatescu, “The Complex Langevin method: When can it be trusted?,” *Phys. Rev. D*, vol. 81, p. 054508, 2010.
- [105] G. Aarts, F. A. James, E. Seiler, and I.-O. Stamatescu, “Complex Langevin: Etiology and Diagnostics of its Main Problem,” *Eur. Phys. J.*, vol. C71, p. 1756, 2011.
- [106] A. Yamamoto and T. Hatsuda, “Quantum Monte Carlo simulation of three-dimensional Bose-Fermi mixtures,” *Phys. Rev. A*, vol. 86, p. 043627, 2012.
- [107] G. Aarts and F. A. James, “Complex Langevin dynamics in the SU(3) spin model at nonzero chemical potential revisited,” *JHEP*, vol. 1201, p. 118, 2012.
- [108] C. C. Chang, “Numerical solution of stochastic differential equations with constant diffusion coefficients,” *Math. Comp.*, vol. 49, pp. 523–542, 1987.
- [109] A. Yamamoto, “Lattice QCD with strong external electric fields,” *Phys. Rev. Lett.*, vol. 110, no. 11, p. 112001, 2013.
- [110] L. Landau and E. Lifshitz, *Quantum Mechanics Non-Relativistic, Theory*. Butterworth Heinemann, Oxford, UK, 3rd ed., 1987.
- [111] T. Hayata, Y. Hidaka, and A. Yamamoto, “Temporal Chiral Spiral in Strong Magnetic Fields,” *Phys. Rev. D*, vol. 89, p. 085011, 2014.

- [112] J. S. Schwinger, “On gauge invariance and vacuum polarization,” *Phys. Rev.*, vol. 82, pp. 664–679, 1951.
- [113] V. P. Gusynin, V. A. Miransky, and I. A. Shovkovy, “Dimensional reduction and catalysis of dynamical symmetry breaking by a magnetic field,” *Nucl. Phys. B*, vol. 462, pp. 249–290, 1996.
- [114] I. A. Shushpanov and A. V. Smilga, “Quark condensate in a magnetic field,” *Phys. Lett. B*, vol. 402, pp. 351–358, 1997.
- [115] I. A. Shovkovy, “Magnetic Catalysis: A Review,” *Lect. Notes Phys.*, vol. 871, pp. 13–49, 2013.
- [116] J. O. Andersen, “Theory of the weakly interacting Bose gas,” *Rev. Mod. Phys.*, vol. 76, p. 599, 2004.
- [117] A. Hasenfratz and P. Hasenfratz, “The Scales of Euclidean and Hamiltonian Lattice QCD,” *Nucl. Phys. B*, vol. 193, p. 210, 1981.
- [118] F. Karsch, “SU(N) Gauge Theory Couplings on Asymmetric Lattices,” *Nucl. Phys. B*, vol. 205, pp. 285–300, 1982.
- [119] T. D. Lee and C. N. Yang, “Low-Temperature Behavior of a Dilute Bose System of Hard Spheres. 1. Equilibrium Properties,” *Phys. Rev.*, vol. 112, pp. 1419–1429, 1958.
- [120] P. Grüter, D. Ceperley, and F. Laloë, “Critical Temperature of Bose-Einstein Condensation of Hard-Sphere Gases,” *Phys. Rev. Lett.*, vol. 79, pp. 3549–3552, 1997.
- [121] V. Kashurnikov, N. Prokof’ev, and B. Svistunov, “Critical Temperature Shift in Weakly Interacting Bose Gas,” *Phys. Rev. Lett.*, vol. 87, p. 120402, 2001.
- [122] P. B. Arnold and G. D. Moore, “Transition temperature of a dilute homogeneous imperfect Bose gas,” *Phys. Rev. Lett.*, vol. 87, p. 120401, 2001.
- [123] O. Morsch and M. Oberthaler, “Dynamics of Bose-Einstein condensates in optical lattices,” *Rev. Mod. Phys.*, vol. 78, pp. 179–215, 2006.
- [124] A. Yamamoto and Y. Hirono, “Lattice QCD in rotating frames,” *Phys. Rev. Lett.*, vol. 111, p. 081601, 2013.
- [125] I. Montvay and G. Münster, *Quantum fields on a lattice*. Cambridge monographs on mathematical physics, Cambridge: Cambridge Univ. Press, 1994.